

---

# Magnetohydrodynamical Modelling of the Io Footprint and Tail Morphology

---

## Inaugural-Dissertation

zur Erlangung des Doktorgrades  
der Mathematisch-Naturwissenschaftlichen Fakultät  
der Universität zu Köln

vorgelegt von

**Stephan Schlegel**

aus Illertissen

Köln, 2022

1. Gutachter: Prof. Dr. J. Saur
2. Gutachter: Prof. Dr. B. Tezkan

Tag der mündlichen Prüfung: 03.06.2022

Jupiter's aurora contains emission features that are associated with the Galilean moons, Io, Europa, and Ganymede. These footprints and their associated tail are generated by Alfvén waves that are produced by the relative movement of the moons and Jupiter's corotating plasma. The waves propagate along the magnetic field lines towards both hemispheres of Jupiter and trigger wave-particle interactions. The accelerated particles precipitate down towards Jupiter, generating auroral emissions in the process. The shape and location of these footprints give insight about the interaction and we can draw conclusions about the Jovian magnetic field, density in the magnetosphere, and even the moons atmosphere. Therefore, studying the interaction and observations of the footprints can help to deepen our understanding of the Jovian system. New observations with the Juno spacecraft have provided high resolution images of the footprints. These images revealed structures in the Io footprint tail that were not detectable by previous measurements. In these structures, the symmetry between the poleward and equatorward part of the footprint tail is broken and the tail spots are alternatingly displaced. This "Alternating Alfvén Spot Street" (AASS) is can not be explained by the current models. In this work we use the Alfvén wing model to compare the observed positions of the Io footprint and tail spots with expectations. We show that the locations of the main emissions of the footprint can be used to constrain the density model along the magnetic field lines connected Io's orbit and the Jovian magnetosphere. The inversion provides results comparable to values in the general literature. We further show that the location of the footprint and tail spots are consistent with Alfvén wave that get reflected as they propagate through the inner Jovian magnetosphere.

In the second part of this work, we use magnetohydrodynamic simulations to investigate mechanisms that can break the symmetry and produce structures similar to the observed AASS. To investigate, how the emission pattern in Jupiter's ionosphere would look like, we used the Poynting flux of the Alfvén waves near Jupiter's surface as a proxy. We studied three different mechanisms in our simulation that could break the symmetry. First, we conducted a study where we activated the Hall conductance in Io's atmosphere. We show that the Hall effect can significantly alter the morphology of the Poynting flux. Additionally, combined with non-linear reflections that occur at the Jovian ionosphere, the Hall effect can produce alternating patterns in the footprint tail. We conclude that the Hall effect is a promising candidate for the reason behind the AASS. As a second mecha-

nism, we investigated the influence of the different travel times of Alfvén waves originating from the Jupiter facing and opposite side of Io. The Poynting flux corresponding to the immediate vicinity of the main footprint emissions is only marginally altered. However, the symmetry breaking effect of the travel time difference accumulates down the tail and can therefore be a contributing factor towards generating the AASS. The third mechanism includes the asymmetry of Io's atmosphere. The inhomogeneities in the atmosphere are mapped along the magnetic field line and break the symmetry in the Poynting flux. However, the effects are minor for this mechanism and we rule out the asymmetries as the reason for the AASS.

This work shows that the locations of the Io footprint and associated tail spots are consistent with reflected Alfvén waves in the magnetosphere and can be used to constrain a density model. Our study additionally provides an explanatory model for the generation of the observed AASS. In this model the Hall effect combined with non-linear reflection can explain the observed pattern, while travel time differences of Alfvén waves can play a contributing role. Further observation of the Galilean footprints could confirm this hypothesis.

---

## Kurzzusammenfassung

---

Ein Teil von Jupiter's Aurora ist auf die Galileischen Monde Io, Europa und Ganymede zurückzuführen. Diese charakteristischen Lichter befinden sich an den Enden der Magnetfeldlinien, die die orbitalen Positionen der Galileischen Monden mit Jupiters Atmosphäre verbinden und werden daher Fußpunkte genannt. Die Fußpunkte und deren zugehörigen Schweife werden durch Alfvénwellen generiert, welche wiederum durch die Relativbewegung der Monde und das umgebende Plasma erzeugt werden. Die Alfvénwellen breiten sich entlang der magnetischen Feldlinien aus und lösen Wellen-Teilchen-Wechselwirkungen über Jupiters Atmosphäre aus. Dadurch werden Teilchen zu Jupiter hin beschleunigt und können bei Kontakt mit atmosphärischen Partikeln Polarlichter erzeugen. Die Form und der Ort dieser Fußpunkte werden bestimmt durch die Generierung und Ausbreitung der Alfvénwellen. Daher können wir durch Beobachtungen Einblick in das Magnetfeld und die Dichteverteilung in der Magnetosphäre gewinnen und sogar Rückschlüsse über die Atmosphären der Monde schließen.

Die Juno Weltraumsonde ist seit dem Jahr 2016 im Orbit um Jupiter und konnte einige hochauflösende Beobachtungen der Fußpunkte und deren Schweife liefern. Im Besonderen zeigten Beobachtungen des Schweifs des Io Fußpunkts neue Merkmale, die mit vorherigen Beobachtungen nicht aufgedeckt werden konnten. Diese Bilder offenbarten asymmetrische Strukturen, die einer Wirbelstraße ähneln. Punktuelle Helligkeitsmaxima im Schweif waren von der erwarteten Spur des Schweifs versetzt, abwechselnd in Richtung Pol und Äquator. Diese "Alternating Alfvén Spot Street" (AASS) kann nicht zufriedenstellend von den momentanen Modellen zur Erzeugung der Fußpunkte und deren Schweif erklärt werden.

In dieser Arbeit benutzen wir das Alfvénflügelmodell um die beobachteten Positionen der Fußpunkte mit den erwarteten Werten abzugleichen. Wir können zeigen, dass die Beobachtungen genutzt werden können um ein Dichtemodell des Plasmas entlang der magnetischen Feldlinien zu rekonstruieren. Das invertierte Modell ergibt Dichtewerte die mit der einschlägigen Literatur vergleichbar sind. Desweiteren zeigen wir, dass die Position der Fußpunkte und der Helligkeitsmaxima im Schweif mit dem Reflektionsverhalten von Alfvénwellen an den Dichtegradienten in der Magnetosphäre übereinstimmen.

Im zweiten Teil der Arbeit konzentrieren wir uns auf die Frage, wie die AASS erzeugt werden kann. Dazu benutzen wir magnetohydrodynamische Simulationen um verschiedene Mechanismen zu testen, die die Symmetrie im Schweif brechen kann. Um die Struktur des

Schweifs aus den Simulation abzuleiten, benutzen wir stellvertretend den Poyntingfluss durch eine Analyseebene nahe Jupiters Oberfläche. Wir untersuchen drei verschiedene Mechanismen, die in Frage kommen alternierende Strukturen zu erzeugen. Als erstes studieren wir die Halleitfähigkeit in Ios Atmosphäre. Wir können zeigen, dass der Halleffekt einen großen Einfluss auf die Struktur des Poyntingflusses hat. Zusammen mit den nichtlinearen Reflektionen der Alfvénwellen an Jupiters Ionosphäre erzeugt der Halleffekt lateral versetzte Poyntingflussmaxima im Schweif des Fußpunkts. Dies führt zu dem Schluss, dass der Halleffekt ein vielversprechender Kandidat zur Erzeugung der AASS ist. Als zweites untersuchen wir den Einfluss der unterschiedlichen Laufzeiten der Alfvénwellen die von unterschiedlichen Punkten in Ios Atmosphäre starten. Die längere Laufzeiten der Wellen der von Jupiter abgewandten Zeiten führt zu einer Versetzung der polwärts zeigenden Seite des Fußpunktschweifs, die besonders mit großem Abstand zum Fußpunkt merklich wird. Nahe am Fußpunkt ist der Laufzeitunterschied jedoch nicht bedeutsam. Daher schließen wir, dass die Laufzeitunterschiede zwar ein steuernder Faktor, jedoch nicht der alleinige Grund für die AASS sein kann. Als letztes untersuchen wir den Einfluss der asymmetrischen Atmosphäre von Io. Ios ungleich verteilte Atmosphäre führt zu Asymmetrien im Poyntingfluss. Diese sind jedoch kaum merklich und zu unbedeutend um die beobachteten Strukturen zu erzeugen.

Diese Arbeit zeigt, dass die Position der beobachteten Fußpunkte von Io mit reflektierten Alfvénwellen vereinbar sind. Zudem konnten die Fußpunkte benutzt werden, um Rückschlüsse auf die Plasmadichte in der inneren Magnetosphäre zu ziehen. Die Studie liefert weiterhin ein Erklärungsmodell für die AASS. Dieses Modell beinhaltet den Halleffekt in Ios Atmosphäre kombiniert mit nichtlinearen Reflektionen der Alfvénwellen an Jupiters Ionosphäre. Laufzeitunterschiede könnten den Effekt verstärken. Mithilfe weiterer Beobachtungen der Fußpunkte der Galileischen Monde könnte diese Hypothese bestätigt werden.

---

# Contents

---

<b>List of Figures</b>	<b>vii</b>
<b>List of Tables</b>	<b>ix</b>
<b>1. Introduction</b>	<b>1</b>
<b>2. Io and the Jovian Inner Magnetosphere</b>	<b>5</b>
2.1. Jupiter's Magnetosphere . . . . .	5
2.2. The Innermost Galilean Moon: Io . . . . .	7
2.2.1. Io's Atmosphere . . . . .	7
2.2.2. The Io Torus . . . . .	8
2.3. The Io Footprint . . . . .	10
2.4. Previous Modelling . . . . .	16
<b>3. Magnetohydrodynamic Framework</b>	<b>19</b>
3.1. Ideal Magnetohydrodynamics . . . . .	20
3.1.1. Ideal MHD Waves . . . . .	21
3.2. Alfvén Waves in an Inhomogeneous Medium . . . . .	23
3.2.1. Reflection and Transmission at Discontinuities . . . . .	23
3.2.2. The WKB Approximation . . . . .	24
3.2.3. Reflection in Slowly Changing Media . . . . .	26
3.3. The Hall Effect . . . . .	28
3.4. Collision and Production in MHD . . . . .	29
3.5. Pedersen and Hall Conductance . . . . .	31
<b>4. The Alfvén Wing Model</b>	<b>37</b>
4.1. General Idea of the Alfvén Wing Model and Geometry . . . . .	37
4.2. Current System Inside the Alfvén Wing . . . . .	38
4.3. Field Equations Inside the Alfvén Wing . . . . .	39
4.3.1. Energy Transport . . . . .	42
4.4. Semi-Analytical Model . . . . .	43
4.5. Non-linear Reflections . . . . .	47

<b>5. Application of the Io Alfvén Wing Model</b>	<b>55</b>
5.1. JRM09 Magnetic Field Model . . . . .	55
5.2. Torus Density Model . . . . .	56
5.3. Inversion of Footprint Position . . . . .	58
5.4. Position of the Secondary Tail Spots . . . . .	61
<b>6. MHD Simulation Setup</b>	<b>63</b>
6.1. The PLUTO Code . . . . .	63
6.2. Model, Grid and Parameters . . . . .	64
6.3. Io as Neutral Gas Cloud . . . . .	66
6.4. Validation of the Simulation . . . . .	67
6.4.1. Reflection of Alfvén Waves . . . . .	68
6.4.2. Force Balance and Conductivities . . . . .	72
6.5. The Reference Simulation . . . . .	77
6.5.1. Reference Poynting Flux . . . . .	78
<b>7. Influence of the Hall Effect</b>	<b>81</b>
7.1. Implementation of the Hall Effect . . . . .	81
7.2. Non-linear Reflection with High Hall Conductance . . . . .	83
7.3. Poynting Flux with Hall Conductance . . . . .	87
<b>8. Further Mechanisms</b>	<b>91</b>
8.1. Travel Time Difference . . . . .	91
8.1.1. Implementation and Simulation . . . . .	92
8.2. Asymmetric Atmosphere . . . . .	96
8.2.1. Simulation with an Asymmetric Atmosphere . . . . .	97
<b>9. Conclusions</b>	<b>99</b>
<b>Bibliography</b>	<b>101</b>
<b>Appendix</b>	<b>109</b>
A. Vlasov Equation . . . . .	109
A.1. Collision Term . . . . .	109
A.2. Production and Loss Term . . . . .	110
B. Analytical Derivations in the Alfvén Wing . . . . .	113
B.1. Perpendicular Magnetic Field . . . . .	113
B.2. Numerical Alfvén Wing Model . . . . .	114
B.3. Validation of the Code in the Case of Constant Conductances . . . . .	119
B.4. Poynting Flux . . . . .	119

---

## List of Figures

---

2.1.	JRM 33 Lowes Spectrum and Magnetic Surface Field Strength . . . . .	6
2.2.	Io Torus Density Distribution . . . . .	9
2.3.	Alfvén Wing Model with Reflections . . . . .	11
2.4.	First Observations of the Io Footprint . . . . .	12
2.5.	Leading Spot . . . . .	14
2.6.	JIRAM Observations of the Io Footprint and Tail . . . . .	15
2.7.	Previous MHD Simulation Model . . . . .	17
2.8.	Previous MHD Simulation Results . . . . .	17
3.1.	Friedrichs diagram . . . . .	23
3.2.	Effective reflection coefficient . . . . .	28
3.3.	Collision Currents . . . . .	32
4.1.	Alfvén wing . . . . .	38
4.2.	Hall interaction strength . . . . .	42
4.3.	Alfvén wing velocity field . . . . .	45
4.4.	Alfvén wing Poynting flux . . . . .	45
4.5.	Alfvén wing current . . . . .	46
4.6.	Alfvén wing profile with Hall conductance . . . . .	46
4.7.	Alfvén wing current profile with Hall conductance . . . . .	47
4.8.	Alfvén characteristics . . . . .	48
4.9.	Linear vs. non-linear reflection . . . . .	49
4.10.	Poynting flux at linear reflections . . . . .	50
4.11.	Poynting flux at non-linear reflections . . . . .	51
4.12.	Pre-reflection Alfvén wing field . . . . .	52
4.13.	Post reflection Alfvén wing field . . . . .	52
5.1.	JRM09 Magnetic Field on the Surface . . . . .	56
5.2.	Density Model along Magnetic Field Line . . . . .	57
5.3.	Velocity Gradient along the Io Flux Tube . . . . .	57
5.4.	Leading Angle . . . . .	58
5.5.	Best Model Fit . . . . .	60
5.6.	Density Gradient in the Io Flux Tube . . . . .	61

5.7. Reflection Pattern of Secondary Spots in the Northern Jovian Ionosphere . . . . .	62
5.8. Reflection Pattern of Secondary Spots in the Southern Jovian Ionosphere . . . . .	62
6.1. Background Model . . . . .	65
6.2. Streamlines of the simulated Alfvén wing . . . . .	68
6.3. Reflection Test for Velocity . . . . .	69
6.4. Reflection Test for Magnetic Field Strength . . . . .	70
6.5. Reflection at different density gradients with a smaller gas cloud . . . . .	71
6.6. Reflection at different density gradients with a normal sized gas cloud . . . . .	71
6.7. Reflection Spectrum . . . . .	72
6.8. Morphology of Poynting Flux after Reflection . . . . .	73
6.9. Sum of all forces in x-direction . . . . .	74
6.10. Force Balance in X Direction . . . . .	75
6.11. Advection Currents . . . . .	75
6.12. Advection Currents at $z = 20$ . . . . .	76
6.13. Force Balance as profile along x . . . . .	76
6.14. Comparison of Conductivities from simulation and collision frequency . . . . .	77
6.15. Reference Simulation velocity field . . . . .	78
6.16. Reference Simulation Poynting Flux . . . . .	79
7.1. The Effect of Particle Mass on the Conductances and Interaction Strength . . . . .	82
7.2. Influence of the Hall effect for the $V_X$ component . . . . .	84
7.3. Influence of the Hall effect for the $V_Y$ component . . . . .	84
7.4. Influence of the Hall effect for the $B_Y$ component . . . . .	85
7.5. Influence of the Hall effect for the $B_X$ component . . . . .	86
7.6. Influence of the Hall effect for the $j_z$ component . . . . .	86
7.7. Poynting flux with the Hall effect . . . . .	88
7.8. Poynting Flux Maxima with Hall Effect . . . . .	89
8.1. Travel Time Difference Sketch . . . . .	93
8.2. Calculated Travel Time Differences . . . . .	94
8.3. Poynting Flux of Simulation with Travel Time Difference . . . . .	95
8.4. Poynting Flux of Travel Time Difference and Hall Effect . . . . .	96
8.5. Pedersen Conductance of Asymmetric Atmosphere Model . . . . .	97
8.6. Poynting flux of the Asymmetric Atmosphere Simulation . . . . .	98

---

## List of Tables

---

2.1. Best fit parameters of the Io torus model (Phipps et al., 2019) . . . . .	9
4.1. Parameters for the numerical calculations of the Alfvén wing . . . . .	44
6.1. Properties of the reference simulation . . . . .	66
6.2. Analytical and Numerical Reflection and Transmission Coefficients . . . . .	70
7.1. Lateral and Longitudinal Separation of Maxima . . . . .	89



# CHAPTER 1

---

## Introduction

---

The electromagnetic interaction between the Galilean moon Io and Jupiter is a prime example for moon-planet or star-planet interactions. A very striking feature of this interaction is the Io footprint and its tail, an auroral emission in Jupiter's ionosphere associated with the motion of Io around Jupiter. The main emission of the footprint is located at the base of the field lines that map onto Io's orbital position in Jupiter's inner magnetosphere. The coupling between Io and Jupiter's ionosphere is established by Alfvén wings (Neubauer, 1980), a flux tube of Alfvénic perturbations that originate at Io and propagate along the magnetic field lines towards Jupiter. These Alfvén waves can trigger wave particle interactions in the vicinity of Jupiter's ionosphere, accelerating particles towards Jupiter's surface in the process. The location and shape of the footprint emissions provide insights about the interaction and can help to constrain the magnetic field (Connerney et al., 1998) or density distribution in the magnetosphere. Additionally, it can be used as a diagnostic to infer characteristics of the moon itself, since the conductivity distribution of the obstacle determines the fields inside the Alfvén wing (e.g. Neubauer (1998, 1999); Saur et al. (1999)).

The first hint of a moon-planet interaction between Io and Jupiter were radio bursts in intervals of Io's orbital period (Bigg, 1964). Voyager I in-situ measurements gave evidence to a standing Alfvén wave current system (Acuna et al., 1981). The first images of the Io footprint were in the infrared by Connerney et al. (1993), followed by ultraviolet observations by the Hubble Space Telescope (Clarke et al., 1996) and in this visible (Vasavada et al., 1999). Since then, more observations have provided additional insights about the position and structure of the footprint emissions. Connerney and Satoh (2000) detected multiple footprint spots with an angular separation of  $5^\circ$  that can be explained with reflection of the Alfvén waves at density gradients. Observations of additional features like the elongated tail emissions (Clarke et al., 2002) and the leading spot (Bonfond et al., 2008) broadened the understanding of the interaction. The Juno spacecraft, which is in orbit around Jupiter since July 2016, provided high resolution images of the footprint of Io and the other Galilean moons, Europa and Ganymede in the infrared with the JIRAM (JovianInfraRedAuroralMapper) infrared camera (Mura et al., 2018; Moirano et al., 2021). The observations showed new structures not resolvable with earth based telescopes.

The spots in the tail of the Io footprint were alternatingly displaced towards the poles and the equator generating a tail structure resembling a vortex street, here referred to as Alternating Alfvén Spot Street (AASS). The broken symmetry between poleward and equatorward side of the tail emission is a puzzling feature that can not be explained with current models. Furthermore, the authors argued that the inter-spot separation in the tail emissions is too small to be explained by reflections inside the torus alone as proposed by Gérard et al. (2006). In this work, we will analyze whether the location of the main footprint emission and the separation distance of the secondary spots are consistent with reflected Alfvén waves. Additionally, the location of the main emissions of the Io footprints will be used for an inversion to constrain the density profile along the magnetic field lines connecting the Jovian ionosphere to Io's orbit.

In the second part of this work, magnetohydrodynamic (MHD) simulations of the interaction with the single fluid MHD code PLUTO will be conducted. The aim is to investigate mechanisms that can break the symmetry in the Io footprint tail. For that purpose a reference simulation with a simplified geometry is set up, where no symmetry breaking effects are included. As a proxy for the available power to accelerate particles near Jupiter's ionosphere, the Poynting flux through an analysis plane representing the acceleration region is used. In the next step, three different mechanisms are added separately in order to investigate their influence on the Poynting flux. (1) The influence of the Hall effect in Io's atmosphere combined with non-linear reflections at the torus boundary and Jupiter's ionosphere is investigated. A parameter study with different ratio's of Hall to Pedersen conductance is conducted. The Hall effect changes the fields and breaks the symmetry inside the Alfvén wing. (2) The effect of different travel times between the Jupiter facing side of Io and opposite side is studied. The longer travel path of the Alfvén wave packages originating from the anti-jovian side is expected to break the symmetry. (3) The atmosphere of Io which defines the distribution of Io's conductance is not symmetric. A more realistic model of Io's conductances is included in the model. Each of these mechanisms will be discussed regarding their likelihood to cause the observed AASS and whether we can expect similar structures at the footprints of the other Galilean moons.

In Chapter 2, the Jovian inner magnetosphere is introduced and Io's atmosphere and surrounding plasma environment is described. A brief overview of the Io footprint observations is provided followed by a short description of the previous MHD modelling regarding the Io Alfvén wings by Jacobsen et al. (2007). In Chapter 3, the theory of the MHD framework is presented, starting with the ideal MHD and the Alfvén wave with emphasis on the reflection behaviour. In the second part of the chapter, the non-ideal MHD concepts important for this work are discussed, in particular the Hall effect and collision terms that are associated with Pedersen and Hall conductivity. In Chapter 4, the concept and theoretical basics of the Alfvén wing model are explained. A semi-analytical modelling of the Alfvén wing provides insight about the importance of the Hall effect and non-linear reflections. Chapter 5 shows modelling studies regarding the expected position of the Io footprint main emission and tail spots. The model incorporates the JRM09 magnetic field model (Connerney et al., 2018) and uses the positions of the Io footprints for an inversion constraining the density distribution along the magnetic field lines. In the last part of the chapter the model is used to study, whether the inter-spot distance observed by Mura et al. (2018) coincides with reflected Alfvén waves. The MHD simulation setup and reference simulation is shown in Chapter 6. The simulation is validated on the basis of theoretical expectations. Chapter 7 investigates the influence of the Hall effect in the

simulation and shows how the Poynting flux changes due to the Hall conductance in Io's ionosphere. It is discussed how the observed structures could form due to the Hall effect. The effects on the simulation results of the travel time difference and the asymmetries in Io's atmosphere are discussed in Chapter 8. The thesis closes with a conclusion in Chapter 9.



---

## Io and the Jovian Inner Magnetosphere

---

Io is embedded in Jupiter's strong magnetosphere. To understand the moon-magnetosphere interaction that generates the Io footprint, it is important to get insight about the system the interaction is embedded in. The magnetic field strength and morphology and the density distribution in the Jovian inner magnetosphere determine the location, shape and multiplicity of the Io footprint emissions. Furthermore, Io's atmosphere as a neutral obstacle governs the intensity of the interaction. In this chapter, first, the system will be described. Afterwards, the current model explaining the generation of the Io footprint will be discussed with the help of footprint observations. This chapter is closed by an examination of previous modelling studies using MHD simulations by Jacobsen et al. (2007, 2010).

### 2.1. Jupiter's Magnetosphere

First evidence of Jupiter's internal magnetic field were radio signals originating from the direction of Jupiter (Burke and Franklin, 1955), which were later correlated to Jupiter's rotational period (Franklin and Burke, 1958). The position of the dipole was inferred from synchrotron radiation by Morris and Berge (1962) with a dipole tilt of  $\approx 9^\circ$  in direction of  $\lambda_{III} \approx 200^\circ$  in western longitude. Warwick (1963) later determined the direction of the dipole and found that the radial component of the magnetic field is positive at Jupiter's north pole and negative at its south pole, contrary to Earth's magnetic dipole. Constraining higher moments of the magnetic field was first possible with the arrival of spacecraft in Jupiter's magnetosphere. With Pioneer 11 and Voyager 1 data as well as the position of the Io flux tube footprint, Connerney et al. (1998) derived a multipole magnetic field model of Jupiter's internal field up to fourth order, called the VIP4 model (**V**oyager**I**o**P**ioneer). The multipole model is applicable in the absence of currents, when Ampère's law states that the magnetic field is curl-free. Therefore, we can define the magnetic field as conservative  $\mathbf{B} = -\nabla V$  and we can represent the magnetic potential  $V$  by a spherical harmonic expansion (e.g. Chapman and Bartels (1940))

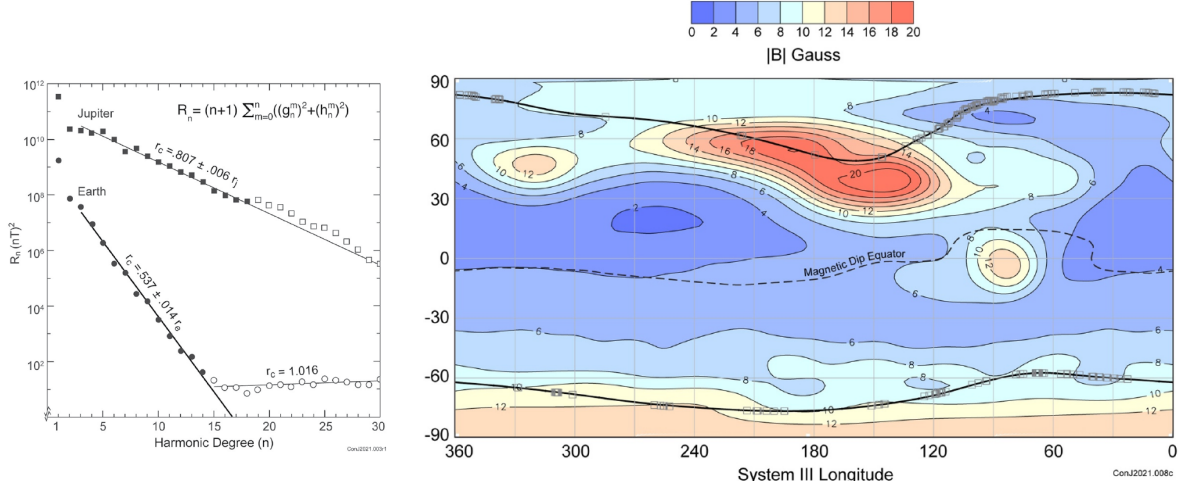


**Figure 2.1.:** Left: Mauersberger/Lowes spectrum of the JRM33 model (squares) by Connerney et al. (2021) compared to that of Earth (circles). The internal Gauss coefficients  $g_n^m$  and  $h_n^m$  calculated with Equation 2.1 are combined for each degree  $n$  to a value  $R_n$  representing the magnetic energy for each degree. The spectrum of  $R_n$  is then fitted by a linear regression for all degrees  $n > 2$ . Right: Surface magnetic field strength on the flattened ellipsoid of Jupiter ( $f = 1/15.4$ ) calculated with the JRM33 model (Connerney et al., 2021). The black lines near the poles indicate the predicted positions of the Io footprint with the measured locations as grey squares. The magnetic equator ( $B_r = 0$ ) is shown as dashed line.

$$V = a \sum_{n=1}^{N_{max}} \left(\frac{a}{r}\right)^{n+1} \sum_{m=0}^n P_n^m(\cos(\vartheta)) (g_n^m \cos(m\varphi) + h_n^m \sin(m\varphi)), \quad (2.1)$$

with  $a = 71492$  km being Jupiter’s equatorial radius,  $r$  the distance to Jupiter’s center, colatitude  $\vartheta$  and longitude  $\varphi$ . The associated Legendre polynomials  $P_n^m$  are of degree  $n$  and order  $m$ . The Gauss coefficients  $g_n^m$  and  $h_n^m$  are Schmidt semi-normalized. Since no magnetic monopoles exist ( $\nabla \cdot \mathbf{B} = 0$ ), the minimum degree is  $n = 1$ . Here, only the potential  $V$  for the internal field is given. The external field is not associated with the Jovian dynamo, but is dominated by the magnetodisc (Connerney et al., 2020). With arrival of the Juno spacecraft that orbits around Jupiter in close polar orbits, a new multipole model was created, first up to tenth order (Connerney et al., 2018), called JRM09 model and by now up to 18<sup>th</sup> order, called JRM33 model (Connerney et al., 2021). The models are named as *Juno Reference Model* and the number refers to the number of used Juno perijoves used for the inversion. Figure 2.1 shows the Mauersberger/Lowes spectrum of the JRM33 model as well as the calculated magnetic field strength on the surface of Jupiter, which is much more dynamically flattened ( $f = 1/15.4$ ) than Earth due to its fast rotation period and low density. The Lowes spectrum shows a much slower decline of the magnetic energy  $R_n$  in higher degrees  $n$ , indicating a dynamo much closer to the surface. The linear fit suggests a dynamo depth of  $0.81R_J$ , which most likely marks the edge of the convective metallic hydrogen region (Connerney et al., 2021).

Jupiter’s magnetic field on the surface is much more variable than Earth’s due to the contribution of higher degree multipoles. A very distinct feature is the high magnetic field strength region at about  $40^\circ - 60^\circ$  co-latitude and  $120^\circ - 140^\circ$  western longitude. This features draws the Io footprint (black line) and the aurora closer to the equator. There is no similar feature on the southern hemisphere, where the aurora is much more circular

shaped. Another interesting feature is the so called *Great Blue Spot* (GBS), located at the equator at about  $90^\circ$  longitude, where the magnetic field strength towards Jupiter, i.e.  $-B_r$ , is the highest. At the vicinity of Io, the magnetic field can well be approximated by a dipole with a tilt of  $\vartheta_D = 10.25^\circ$  towards  $\varphi_D = 196.38^\circ$  western longitude and a dipole moment of  $M = 4.177$  G. There, the plasma is frozen into the magnetic field and it can be assumed to be close to perfect co-rotation. Further outside towards the middle magnetosphere, the co-rotation breaks down and the magnetic field starts to lag behind. The corresponding currents morph the magnetic field and the Laplace equation does not hold anymore. Therefore, the multipole magnetic field description is extended by the current sheet (CAN) model to account for the magnetic field associated with these currents (Connerney, 1981). At Io however, the dipole approximation is sufficient.

## 2.2. The Innermost Galilean Moon: Io

With its radius of  $R_{Io} = 1822$  km, Io is the second smallest of the Galilean moons after Europa. It is the Galilean moon closest to Jupiter with an orbital distance of about  $r_{Io} = 4.2 \cdot 10^6$  km or about 5.9 Jupiter radii  $R_J$ . Its orbital period of 42.5 h with an orbital velocity of about  $v_{orb} = 74$  km/s forms a 1:2:4 Laplace resonance with Europa and Ganymede. The corresponding Jovian synodic period is about 13 h. Therefore, the relative velocity between Io and its surrounding plasma is about  $v_{rel} = 57$  km/s. Io is tidally locked to Jupiter, roughly showing the same side towards Jupiter at all times. Peale et al. (1979) proposed that tidal heating due to Io's eccentricity of  $\epsilon = 0.004$  was significant enough to induce tides that result in considerable tidal dissipation, which would melt a major fraction of Io's interior. Data from the Voyager I mission confirmed this prediction and showed that Io is the volcanically most active body in the solar system. Galileo spacecraft measurements of Io's gravitational field suggested a differentiated interior. Io consists of a metal core and a silicate mantle with a crustal exterior that consists of silicate lava and  $\text{SO}_2$  frost.

### 2.2.1. Io's Atmosphere

Io possesses a tenuous atmosphere that was first confirmed by the *Pioneer 10* spacecraft in 1973 (Kliore et al., 1974, 1975). It is surrounded by neutral gas from different sources. It is assumed that the largest part of the atmosphere is from sublimation of  $\text{SO}_2$  due to heating from sun light (Lellouch et al., 2015; Tsang et al., 2013). A less substantial part is due to volcanic out-gassing. It is assumed that sputtering plays a negligible role for the atmosphere of Io. Earth-based telescope observation can be used to give insight about the day-side atmospheric column density of Io. The equatorial surface pressure at the day-sight was concluded to be in the range of  $100 - 1000 \mu\text{Pa}$  (Lellouch et al., 2007). Since the sublimation is dependent on the insulation, the atmosphere collapses, when Io is in eclipse (Tsang et al., 2016). Furthermore, the atmosphere is mostly confined to a band around the equator. At the poles, the atmospheric density drops to about  $\approx 2\%$  of the equatorial density Strobel and Wolven (2001); Feaga et al. (2009), where the vertical column density is in the range of  $1.5 \cdot 10^{16}$  to  $1.5 \cdot 10^{17} \text{ cm}^{-2}$  (Feaga et al., 2009; Lellouch et al., 2015). This together with the transient and localized volcanic out-gassing makes for a inhomogeneous and time variable atmosphere. The composition close to the surface of Io is mostly the

sublimated  $SO_2$ , which can be dissociated by electron impacts to SO and O. At the night side and at the poles, where the volcanic plumes contribute a more considerable part to the atmosphere, the relative contributions  $S_2$  and SO increase (Spencer et al., 2000; Moses et al., 2002). Io's ionosphere mostly consists of  $SO_2^+$  ions, created by mass loading, i.e. by the impact of thermal electrons on the neutral atmospheric particles. It has been shown that photoionization contributes only a minor part to the total ionization (Saur et al., 1999). The main sink for ionospheric ions is recombination of  $SO_2^+$  ions to S and SO. The temperatures of the ions upstream of Io is in the range of 20-90 eV (Kivelson et al., 2004; Frank and Paterson, 2001) and consists mostly of sulfur and oxygen ions.

### 2.2.2. The Io Torus

Particles lost around Io to Jupiter's magnetosphere form a plasma torus (e.g. Bagenal et al. (2017)). The neutral particles form a banana shaped neutral cloud around Io which moves with its orbital period (Mendillo et al., 2007). The neutrals then can become ionized by charge exchange or electron impacts. The newly generated ions are then frozen into Jupiter's magnetic field and accelerated to co-rotation. This creates a torus of charged particles around Io's orbit. The trapped particles can move along the magnetic field lines but are mostly confined by centrifugal forces to a disc approximately  $6.9^\circ$  tilted against the rotational equatorial plane. This is about  $2/3$  of the way from the rotational equator to the magnetic equator with a tilt of about  $10.31^\circ$  (Connerney et al., 2018) and defines the region where the magnetic field lines are farthest away from the rotational axis. The torus is often described to consist of three distinct regions defined by their distance to Jupiter. These regions differ in density and temperature and therefore scale height. They are called the cold torus, ribbon and warm torus (Bagenal and Sullivan, 1981; Bagenal, 1994). The cold torus likely arises from the diffusion of ions towards Jupiter and is centered at about  $r_{CT} = 5.23R_J$  (Thomas et al., 2004). While diffusing inward the ions cool by radiation (Richardson et al., 1980). The peak number density of the cold torus is about  $n_{CT} = 1000 \text{ cm}^{-3}$  with a low ion temperature of  $T_{i,CT} = 2 - 4 \text{ eV}$  (Thomas et al., 2004). The thin and sharply defined ribbon is centered at  $r_R = 5.6R_J$ . It is an inward extension of the warm outer torus and was defined by the small band of bright SII emissions (Trauger, 1984). It has a higher peak number density than the cold torus of around  $n_R = 3000 \text{ cm}^{-3}$  and the temperature increases from  $T_{i,CT} = 2 - 4 \text{ eV}$  at the cold torus to about  $T_{i,R} = 70 \text{ eV}$  near Io's orbit at  $r_{Io} = 5.9R_J$  (Thomas et al., 2004). At Io's position, the warm torus begins with a almost constant temperature of  $T_{i,WT} = 70 - 100 \text{ eV}$  (Bagenal, 1994). The number density at Io is about  $n_{WT} = 2000 \text{ cm}^{-3}$  and decreases outwards, reaching about  $n_E = 20 \text{ cm}^{-3}$  at Europa's orbit. The density distribution of the torus is shown in Figure 2.2. The main loss mechanism in the ribbon and warm torus is the outward diffusion of the plasma through the Jovian magnetosphere (Bagenal and Delamere, 2011), which takes about 20-80 days (Bolton et al., 2015). With the Juno spacecraft in orbit around Jupiter, radio occultation measurements helped to determine the location and extension of the different regions (Phipps and Withers, 2017; Phipps et al., 2018, 2019, 2020, 2021). It has been shown that the location of the torus is fixed within Jupiter's rotational rest frame and does not change noticeable with time. Yet, the peak number densities of the different region do not seem to vary with longitude, but are not constant in time.

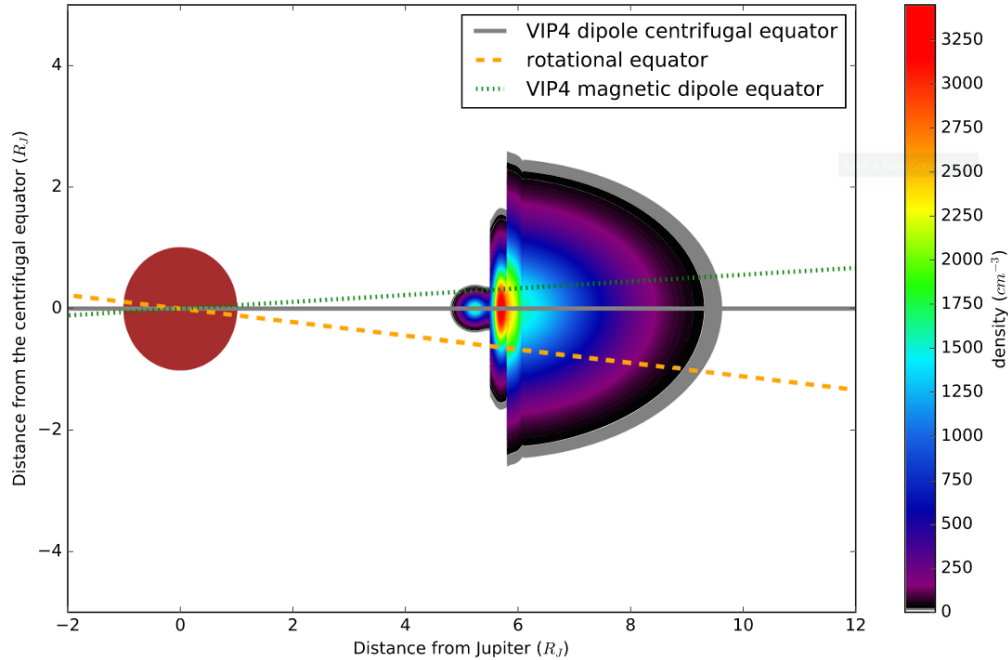


**Figure 2.2.:** Best fit model for the density distribution of the Io torus. It consists of three distinct regions: The cold torus at about  $r = 5.2R_J$  with the smallest scale height, the dense small region at  $r = 5.6 - 5.9R_J$ , called ribbon and the warm torus starting from  $r = 5.9R_J$  with the largest scale height. The torus is roughly confined within the centrifugal equator, here represented by the older VIP4 model dipole (Connerney, 1981). Figure taken from Phipps et al. (2020).

**Table 2.1.:** Best fit parameters of the Io torus model (Phipps et al., 2019)

Region	$\rho_{max}$ [ $\text{cm}^{-3}$ ]	$r_{max}$ [ $R_J$ ]	$H$ [ $R_J$ ]	$T_i$ [eV]	$\langle m \rangle$ [amu]
Cold Torus	1740	5.23	0.18	2.2	27.3
Ribbon	3240	5.63	0.71	31.6	25.3
Warm Torus	2430	5.89	1.13	78	24.4

The peak densities  $\rho_{max}$ , scale heights  $H$ , radial distances of peak densities  $r_{max}$ , ion temperatures  $T_i$  and average ion masses  $\langle m \rangle$  of the three regions inferred from the radio occultation by Phipps et al. (2019) are shown in Table 2.1.

Dougherty et al. (2017) used Voyager plasma science data by Bagenal et al. (2017) to investigate the radial profile of the Io plasma torus and current sheet and derive an empirical radial model. They arrive at similar values as Phipps et al. (2019) for peak densities and ion temperatures for the warm torus region and beyond. In their work they used the model by Delamere et al. (2005) for their ion composition of the torus region and beyond and concluded an average ion mass of  $\langle m \rangle \approx 24$  amu. Furthermore, they presented a force balance model to determine the density profiles along the magnetic field lines, where they included the centrifugal force, anisotropic pressure, gravitation of Jupiter and ambipolar electric fields. This model will be used as a reference for further modelling in this work.

## 2.3. The Io Footprint

The first observation of a coupling between Io and the Jovian magnetosphere was published by Bigg (1964), where decametric radiation radio bursts in intervals of Io's orbital period were observed. The absence of a permanent signal was indicative to a localized interaction that moves with Io's orbital period. This led to the development of models that can explain this moon-magnetosphere interaction. Goldreich and Lynden-Bell (1969) developed the unipolar inductor model, where Io can be treated as a unipolar generator and develops a current system along the magnetic field lines that connects to the Jovian ionosphere. The current is closed by the Jovian ionosphere on one side and Io on the other side, creating a stationary current system that moves around Jupiter with Io's orbital period. The decametric radio bursts were argued to originate from beam instabilities in the current sheets. For this model to be applicable, the current system connecting Io and Jupiter needs to build up fast enough for the currents reflected at the Jovian ionosphere to connect back to Io, before Io moves away from the magnetic field line. In other words, the convection time  $\tau = 2v_0 \cdot R_{Io}$ , with the plasma velocity  $v_0$  relative to Io needs to be larger than the travel time  $t_0 = \int v_A^{-1} ds$  of the current carrying Alfvén waves that propagate with the Alfvén velocity  $v_A = B/\sqrt{\mu_0\rho}$ , with  $B$  the magnetic field strength,  $\mu_0$  the free space permeability and  $\rho$  the mass density. Since it was assumed that the Jovian inner magnetosphere was depleted of plasma, the Alfvén velocity was expected to be high enough to fulfill this condition. However, in the late 1970's, multiple measurements indicated that there is considerable plasma density in the Jovian inner magnetosphere, especially in the orbital distance of Io. With the arrival of the Pioneer 10 spacecraft at Jupiter, occultation measurements indicated a ionosphere around Io. Brown and Chaffee Jr (1974) and later Kupo et al. (1976) have detected a neutral Sodium cloud around Jupiter in the vicinity of Io with earthbound telescopes. This cloud could add plasma mass to the inner Jovian magnetosphere by ionizing processes like impact ionization, photoionization or charge exchange. With the Voyager 1 spacecraft passing Jupiter, remote observations in the ultraviolet (Broadfoot et al., 1979) and in situ observations of the plasma number density (Bridge et al., 1979) confirmed the Io plasma torus. Since the Alfvén travel time  $t_0$  can no more considered to be short compared to the convection time  $\tau$ , the unipolar inductor model is not applicable anymore. For that purpose, Neubauer (1980) developed the Alfvén wing model, which expands the linear model by Drell et al. (1965) into the non-linear regime. In this single fluid non-linear MHD model, Alfvén waves are generated in Io's vicinity that propagate along their characteristics towards Jupiter. These waves carry field aligned Alfvén currents that are generated by Pedersen and Hall currents due to collisions in Io's ionosphere or by pickup currents due to plasma production processes (Goertz, 1980). The Alfvén wave travel time from Io to Jupiter is too long for the current to close directly at Jupiter's ionosphere and form a closed circuit like in the unipolar inductor model. However, the Alfvén waves can trigger wave particle interaction close to Jupiter and accelerate particles that precipitate down on Jupiter, creating auroral emissions in the process. Theoretical studies have shown that Alfvén waves can generate parallel electric fields that create electron beams (Crary, 1997; Saur et al., 2018). Juno observations of accelerated electrons (Szalay et al., 2018) and protons (Szalay et al., 2020) in the wake of Io indicated broadband acceleration processes that coincide with acceleration processes of kinetic Alfvén waves (Damiano et al., 2019). Due to reflections of the Alfvén wave at density gradients like the Io torus boundary or Jupiter's

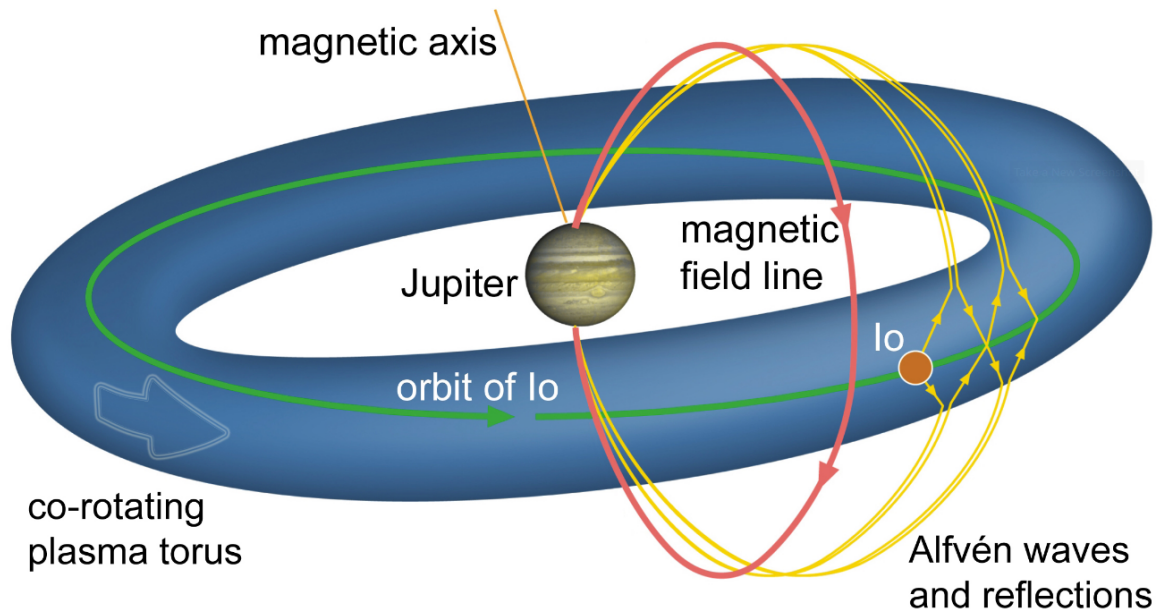


**Figure 2.3.:** Sketch of the propagation of the Alfvén wing by Jacobsen et al. (2007). The characteristics of the Alfvén wing (yellow) are tilted against the background magnetic field (red) due to the decreased Alfvén velocity in the Io torus (blue) and get reflected. The torus is tilted against the magnetic field and Io’s orbital plane (green) and lies in the centrifugal equator.

ionosphere, the Alfvén wing can generate multiple auroral emissions downstream of the main emission (Neubauer, 1980; Gurnett and Goertz, 1983; Bagenal, 1983). A sketch of the far-field interaction with the Alfvén wing and its reflections is shown in Figure 2.3.

Connerney et al. (1993) found the first evidence of auroral emission associated with Io’s Alfvén wing in the infrared. Later observations by the Hubble Space Telescope confirmed the auroral footprint emissions in the ultraviolet (Clarke et al., 1996) and observations by the Galileo spacecraft confirmed the footprint at visible wavelengths (Vasavada et al., 1999). Connerney and Satoh (2000) detected multiple secondary spots downstream of Io’s main footprint emissions. Clarke et al. (2002) obtained the first observations of the footprints of two of the other Galilean satellites, Europa and Ganymede. They furthermore detected elongated tail emissions downstream of the Io main emission that persists for multiple hours. The observations by Connerney et al. (1993), Connerney and Satoh (2000) and Clarke et al. (2002) are shown in Figure 2.4.

The footprint emission of Callisto remains elusive since it is at higher latitudes close to or inside the auroral main emission, but might have been detected on two occasions (Bhattacharyya et al., 2018). Gérard et al. (2006) analyzed 74 different images of the Io footprint made by the Hubble Space Telescope in the ultraviolet. Their study concluded that the relative position of the main footprint and the secondary spots are consistent with reflections of Alfvén waves inside the torus and depend on the relative position of Io inside the torus. Bonfond et al. (2008) detected a faint leading spot upstream of the Io footprint main emission. This leading spot was only visible at the northern or southern hemisphere when Io was at the southern or northern part of the Io torus, respectively. Therefore, they concluded that the leading spot was created by Alfvén waves that accelerate particles not only down towards their respective ionosphere but also back towards Io and to the opposite ionosphere, overtaking the Alfvén wave that is slowed by the high mass density inside the torus. Hence, these transhemispheric electron

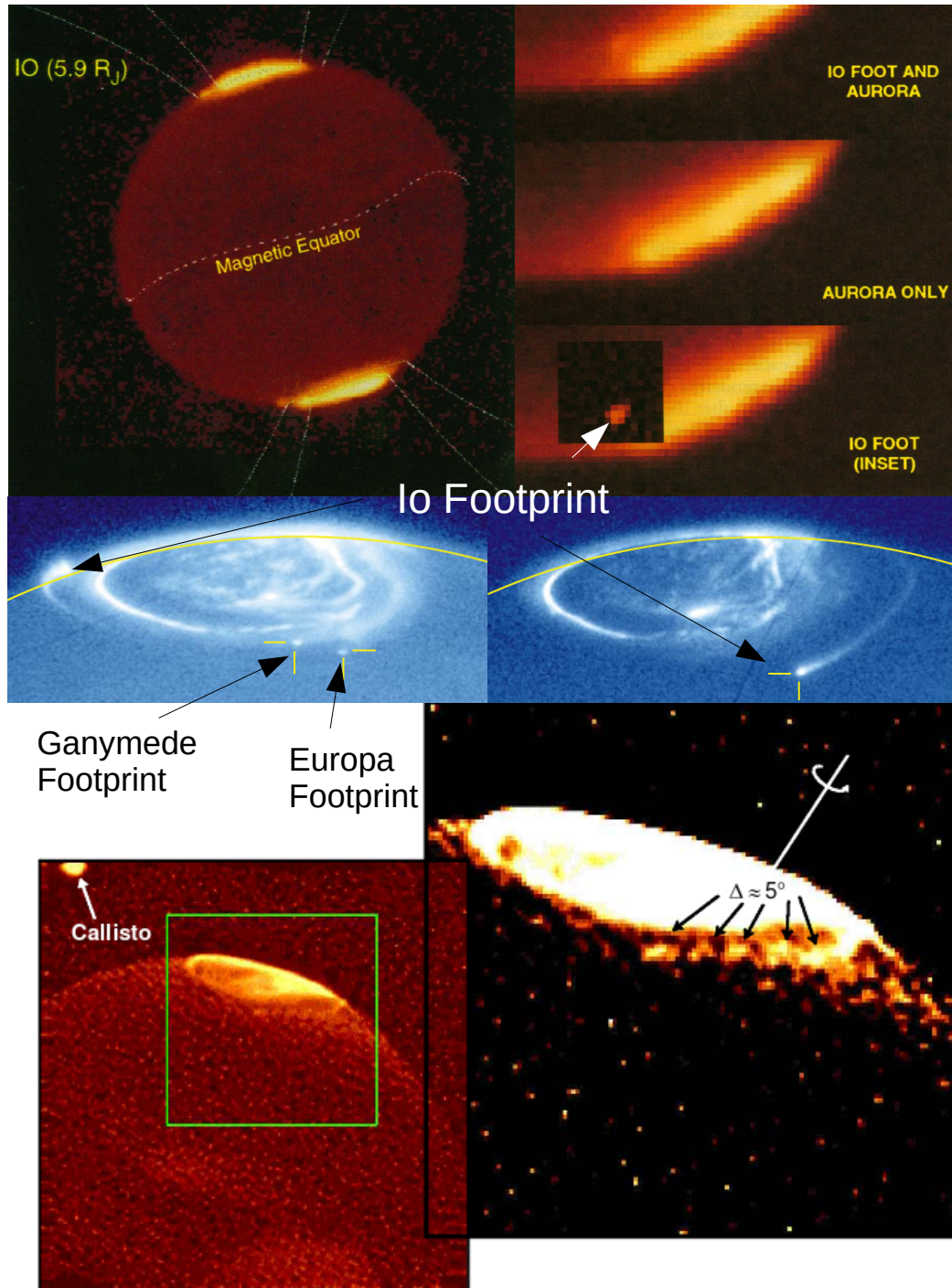


**Figure 2.4.:** The first observations of the Io footprint. Connerney et al. (1993) (top) observed the first evidence of the Io footprint in the infrared. Later observations by Clarke et al. (2002) with the Hubble Space Telescope (center) detected tail emissions in the wake of the Io footprint and found footprints for the other Galilean satellites Europa and Ganymede. Connerney and Satoh (2000) furthermore detected multiple secondary spots downstream of the Io footprint in the infrared.

beams (TEB) can generate emissions before the Alfvén wave arrives close to the Jovian ionosphere, where it triggers wave particle interactions. This hypothesis was supported by the detection of bidirectional electron beams with the Galileo spacecraft at Io’s vicinity (Williams et al., 1996, 1999). Observations of the leading spot and the model are shown in Figure 2.5.

With the Juno spacecraft in orbit around Jupiter, high resolution images of the Io footprint were possible. The Jovian InfraRed Auroral Mapper (JIRAM) has made high resolution infrared images of the footprints and tails of Io (Mura et al., 2018; Moirano et al., 2021) and Europa and Ganymede (Moirano et al., 2021). These observations show substructure in the Io footprint tail spots downstream of the main spot that are not explained by current models. The observations by Mura et al. (2018) are shown in Figure 2.6. The images, taken at September 1<sup>st</sup> 2017, show the Io footprint, leading spot and tail in the infrared, produced by  $\text{H}_3^+$  emissions in the range of 3.3 to 3.6  $\mu\text{m}$ . The top two images show the Io footprint emissions near the south pole. By the time Io was at  $\approx 135^\circ$  western latitude, when it was located roughly  $3.3^\circ$  or  $13R_{Io}$  north of the torus center. Therefore, we can also see a leading spot. The tail spots show alternating displacement of secondary spots towards the equator and the pole from the track predicted by the VIP4 magnetic field model (Connerney et al., 1998). The secondary spots are separated about 350 km along the track and are about 100 km displaced perpendicular to it. The bottom three images show the Io footprint emissions near the north pole about two hours earlier, when Io was at  $\approx 80^\circ$  western longitude. Since by that time Io was about  $3.1^\circ$  or  $12R_{Io}$  below the torus center, we can also see a leading spot here. Furthermore, we can also see the alternating structures in the tail. We will refer to these structures as *Alternating Alfvén Spot Street* (AASS). Later observations showed substructures that are fixed within Jupiter’s rest frame, for which Moirano et al. (2021) suggested a feedback mechanism between Jupiter’s ionosphere and the magnetosphere.

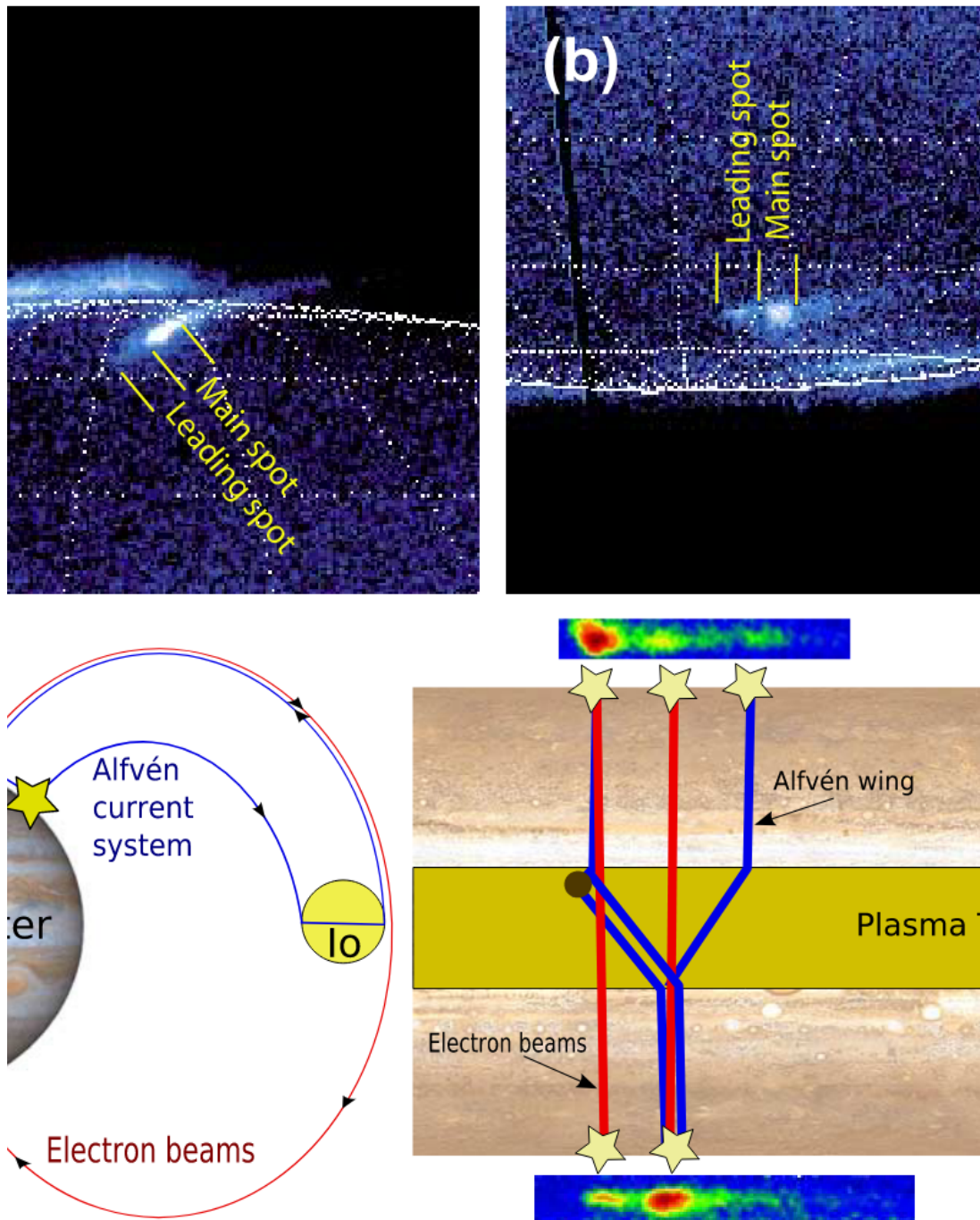


**Figure 2.5.:** Top: Hubble Space Telescope observations of the faint leading spot upstream of the main spot for the northern Io footprint (left) and southern Io footprint (right). Bottom: The TEB model. Waves at the acceleration region at one hemisphere accelerate particles in both direction creating auroral emissions at both hemispheres. When Io is close to one border of the plasma torus, these TEBs can generate auroral emissions upstream of the main spot on the respective opposite hemisphere. Images taken from Bonfond et al. (2008).

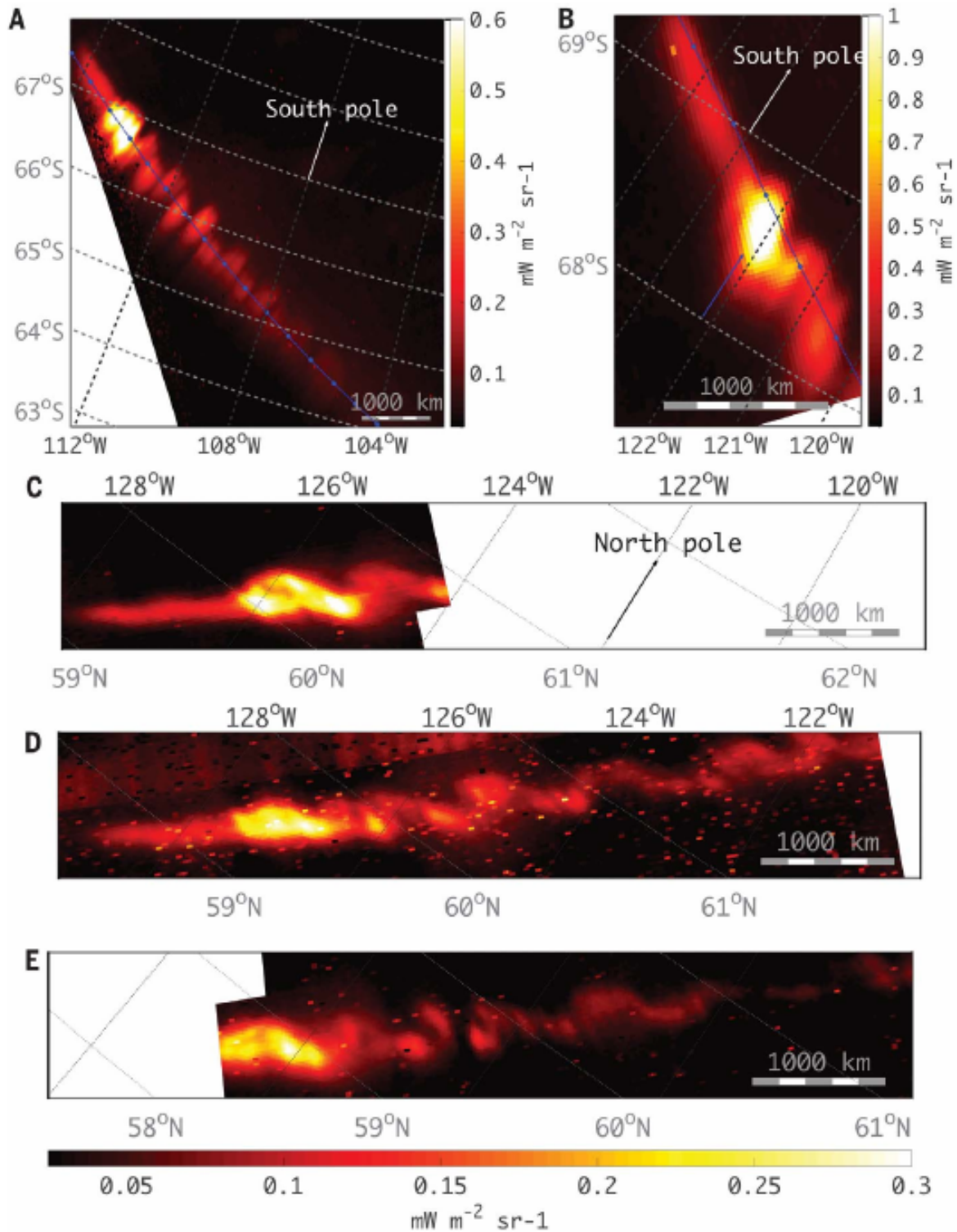


**Figure 2.6.:** JIRAM observations of the Io footprint and tail by Mura et al. (2018). **A** and **B**: Io footprint with leading spot on the south pole, **A** with alternating tail emissions. Images were taken when Io was at  $\approx 135^\circ$  western longitude, when Io is closer to the northern edge of the Io torus. **B** was taken 19 minutes later. The blue arc in **A** shows the predicted track of the Io footprint tail. **C**, **D** and **E**: Io footprint with leading spot and tail on the north pole. The position of Io was at  $\approx 80^\circ$  western longitude, when Io is slightly closer to the southern edge of the torus. Each image was taken approximately 5 minutes apart. Both observations (south and north) show alternating structures in the tail that are displaced towards the pole and the equator.

## 2.4. Previous Modelling

In this work, we will study whether the location of the spots in the AASS can be explained by reflected Alfvén wings and explore mechanisms that can break the asymmetry and create an alternating structure as the observed AASS. For that purpose, we will use MHD simulations that include Io as a Alfvén wave generator and a density model that resembles the travel time and reflections of Alfvén wave along the magnetic field lines. To investigate location and morphology of the presumed emission features in Jupiter’s ionosphere, we will use the available energy carried as Poynting flux by the Alfvén waves as a proxy. A similar study has been conducted by Jacobsen et al. (2007, 2010) to assess the importance of non-linear reflections at the torus boundary. In their study the authors used a simplified geometry of the system with a homogeneous magnetic field in z-direction and a density gradient along this magnetic field. The background density was constant in a region around Io at the center of the simulation domain, resembling the dense torus. Then in a small transition region, the density drops linear to the constant density resembling the high latitudes before the density rapidly rises again near the edge of the simulation domain representing the Jovian ionosphere. The density model and a sketch of the Alfvén wing characteristics is shown in Figure 2.7. In their simulations they compared the reflection pattern of the Alfvén wings in the case of a weak interaction with the one in the case of a strong interaction. In a weak interaction, where the velocity and magnetic field perturbation due to the incident Alfvén waves are negligible to the background velocity and magnetic field, the characteristic of the reflected wave is basically unaltered allowing for a linear reflection, where incident and reflection angle are similar as shown in the left image in Figure 2.8. In the case of a strong interaction however, the velocity and magnetic field perturbations are considerable. Therefore, the characteristic of the reflected wave is distorted and the wave is reflected back into the incident Alfvén wing. This results in a much more complicated reflection pattern where multiple Alfvén wings are superposed and interact non-linearly. The results of this simulation is shown in the right image of Figure 2.8. Since the interaction strength of Io is considered to be high, we can not neglect the non-linearity of reflections and need to include the in the model and considerations going forward as this study shows. However in the modeling in this work, we will use a more realistic density model along the field lines and add different mechanisms to break the symmetry between the Jupiter facing and its opposite side.

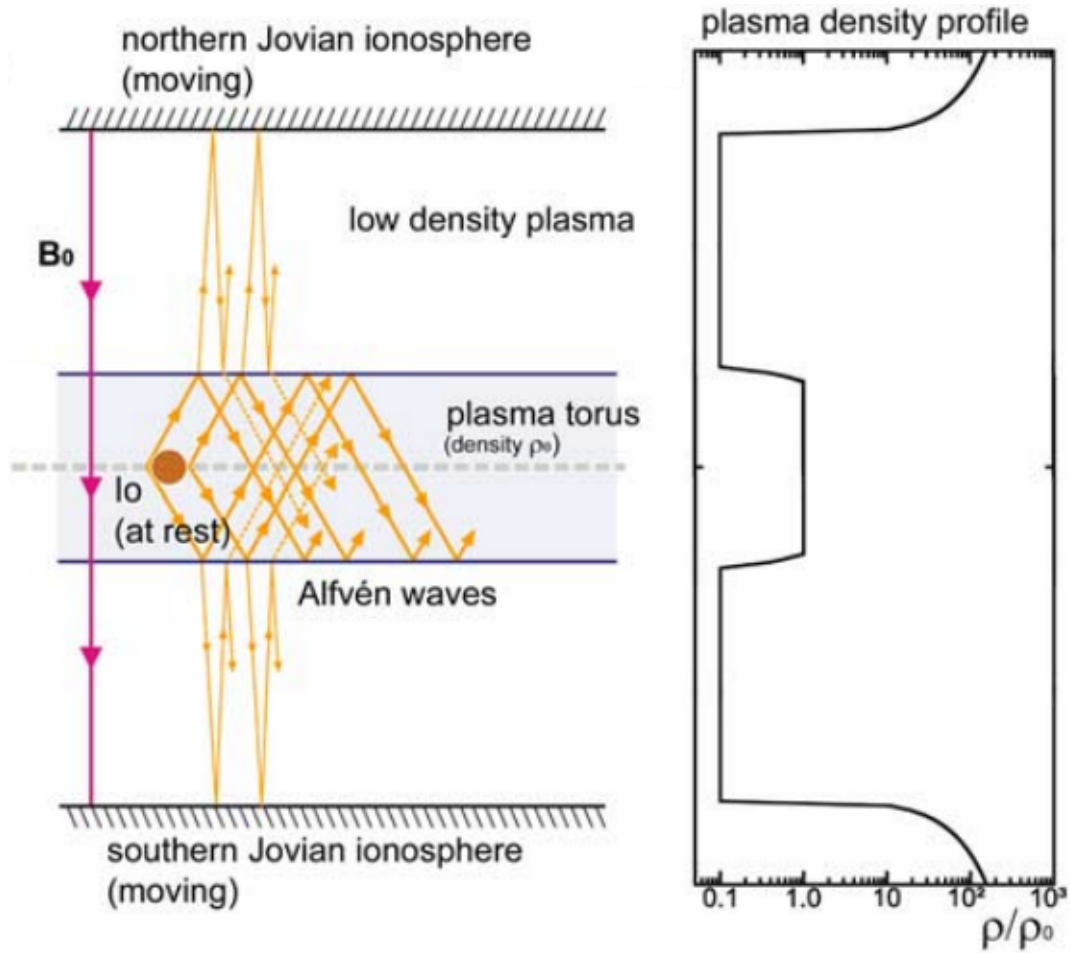


**Figure 2.7.:** Left: The simulation domain with a constant background magnetic field in negative  $z$ -direction (downwards). The density model (right) is created to resemble the density along the magnetic field lines and allow reflections at the torus boundary and the ionosphere. The simulation is conducted in the rest frame of Io, where the Alfvén wing and its reflections (yellow arrows) transition to a steady state (Jacobsen et al., 2007)

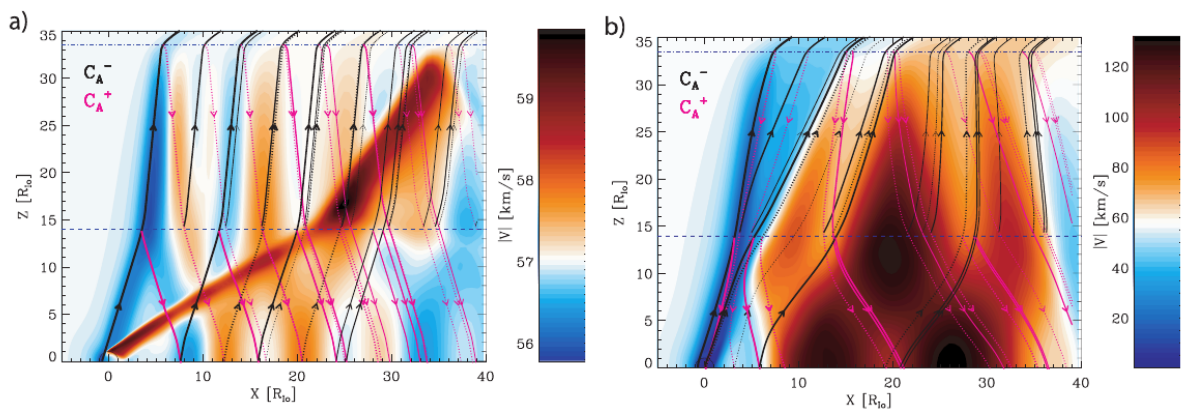


**Figure 2.8.:** Simulation results for weak interaction (left) and strong interaction (right) by Jacobsen et al. (2007). For the weak interaction with a velocity perturbation of about  $\delta v/v = 2\%$  the reflection pattern is linear and the reflected Alfvén wings follow the mostly unperturbed characteristics (black and pink arrows). Furthermore, the increased velocity by the slow mode is well visible. For the strong interaction the velocity perturbation is much higher at about  $\delta v/v \approx 90\%$ . The reflections become non-linear and the characteristics of the Alfvén wings (black and pink arrows) are strongly distorted.



---

Magnetohydrodynamic Framework

---

A geophysical plasma mainly consists of charged particles, ions and electrons. Therefore, it can not be treated as a simple hydrodynamical fluid. The particles are influenced by electrodynamic fields, which in turn are changed by the plasma. There are different theoretical frameworks, which can be used to describe plasmas on different scales. The most rigorous approach would be to describe each particle separately, derive the equations of motion and solve them for all particles. This is normally not feasible. Alternatively, one can describe the plasma by a distribution function  $f(\mathbf{r}, \mathbf{v})$  in phase space and solve the Vlasov equation or the Boltzmann equation for  $f$ . The Vlasov equation is given by

$$\frac{\partial f}{\partial t} + \mathbf{v} \cdot \nabla f + \frac{\mathbf{F}}{m} \cdot \nabla_v f = 0, \quad (3.1)$$

where  $\mathbf{F}$  is any force acting on the particles, normally the Coulomb and Lorentz force and  $\nabla$  and  $\nabla_v$  are the gradient operators with respect to position  $\mathbf{r}$  and velocity  $\mathbf{v}$ , respectively. If the right hand side of Equation (3.1) is not zero, but has term accounting for collisions between particles, the equation is called Boltzmann's equation. The different macroscopic quantities related to the plasma can be derived as velocity moments of  $f$ . This is the case for number the density

$$n_s = \int f_s d^3 \mathbf{v}, \quad (3.2)$$

the bulk velocity

$$\mathbf{v}_s = \frac{1}{n_s} \int \mathbf{v} f_s d^3 \mathbf{v}, \quad (3.3)$$

and the pressure

$$p_s = \frac{m_s}{3} \int (\mathbf{v} - \mathbf{v}_s)^2 f_s d^3 \mathbf{v}. \quad (3.4)$$

Here, the subscript  $s$  defines the species (e.g. electrons or ions) and  $m_s$  is the mass of the particles. In the case where the length scales of the plasma are much larger than the ion gyroradius

$$\rho_i = \frac{m_i v_\perp}{qB}, \quad (3.5)$$

with  $m_i$  the ion mass,  $v_\perp$  the speed of the particles perpendicular to the magnetic field with strength  $B$  and  $q$  the charge of the ion and also the time scales are much longer than the ion gyrofrequency

$$\Omega_i = \frac{qB}{m_i}, \quad (3.6)$$

the plasma can be described as a fluid using magnetohydrodynamics (MHD). In this work, we use the framework of single fluid MHD to describe the plasma.

### 3.1. Ideal Magnetohydrodynamics

In the framework of MHD, the plasma is treated as a continuum with bulk properties that depend on the position  $\mathbf{r}$  in space. The most common properties describing the plasma are the mass density  $\rho(\mathbf{r}) = mn$ , bulk velocity  $\mathbf{v}(\mathbf{r})$  and pressure  $p(\mathbf{r})$  or specific internal energy  $\epsilon(\mathbf{r})$ . Furthermore, MHD connects these plasma parameters with the field parameters from electromagnetism, namely the magnetic field  $\mathbf{B}(\mathbf{r})$ , electric field  $\mathbf{E}(\mathbf{r})$  and current density  $\mathbf{j}(\mathbf{r})$ . MHD combines macroscopic equations derived from the Vlasov equation with Maxwell's equations for the electromagnetic fields. This results in a set of partial differential equation for all species, ions and electrons, called the multi-fluid MHD equations. These can further be combined to the single fluid MHD equations. In the case of ideal MHD, where the conductivity along the magnetic field lines is infinite and the conductivity perpendicular is negligible, the MHD equations read

$$\frac{\partial \rho}{\partial t} + \nabla \cdot (\rho \mathbf{v}) = 0 \quad (3.7)$$

$$\rho \frac{\partial \mathbf{v}}{\partial t} + \rho \mathbf{v} \cdot \nabla \mathbf{v} = -\nabla p + \frac{1}{\mu_0} (\nabla \times \mathbf{B}) \times \mathbf{B} \quad (3.8)$$

$$\frac{\partial}{\partial t} \left( \epsilon + \rho \frac{v^2}{2} + \frac{B^2}{2\mu_0} \right) = -\nabla \cdot \left[ \left( \rho \frac{v^2}{2} + \epsilon + p \right) \mathbf{v} + \frac{\mathbf{E} \times \mathbf{B}}{\mu_0} \right] \quad (3.9)$$

$$\frac{\partial \mathbf{B}}{\partial t} = -\nabla \times \mathbf{E} \quad (3.10)$$

$$\mathbf{E} = -\mathbf{v} \times \mathbf{B} \quad (3.11)$$

$$\epsilon = \frac{1}{\gamma - 1} p \quad (3.12)$$

$$\nabla \cdot \mathbf{B} = 0 \quad (3.13)$$

Equations (3.7), (3.8) and (3.9) are the zeroth, first and scalar second velocity moments of the Vlasov equation. Equation (3.7) is called the continuity equation and states that in ideal MHD, when there are no sources or sinks, the plasma mass density is only changed by advection. Equation (3.8) is the velocity equation and in ideal MHD is similar to the collisionless Navier-Stokes equation in fluid dynamics. However, due to the charged nature of the plasma, the Lorentz force  $\mathbf{F}_L = 1/\mu_0 (\nabla \times \mathbf{B}) \times \mathbf{B}$  also acts as a source of momentum. Here, the current  $\mathbf{j} = \nabla \times \mathbf{B}/\mu_0$  is substituted by the curl of the magnetic field using Ampère's law neglecting displacement currents. The velocity equation can also be rewritten as momentum equation for the momentum  $\rho \mathbf{v}$  of the plasma. Equation (3.9) is the energy equation and states that the total energy of the plasma, consisting

of internal energy  $\epsilon$ , kinetic energy  $\rho v^2/2$  and magnetic field energy  $B^2/(2\mu_0)$  is either changed by energy advection or by electromagnetic field transport by the Poynting flux  $\mathbf{S} = \mathbf{E} \times \mathbf{B}/\mu_0$ . Equation (3.10) is Faraday's law from the Maxwell equations, also referred to as the induction equation. In ideal MHD, the plasma is frozen into the magnetic field line and the electric field can be described as in equation (3.11). The ideal MHD induction equation therefore reads

$$\frac{\partial \mathbf{B}}{\partial t} = \nabla \times (\mathbf{v} \times \mathbf{B}). \quad (3.14)$$

The electric field can be understood as a Gallilei transformation to a reference frame with non-zero plasma movement perpendicular to the magnetic field. In this reference frame, the bulk velocity perpendicular to the magnetic field can in turn be described as the  $\mathbf{E} \times \mathbf{B}$  drift motion. Equation (3.12) relates the pressure and the internal energy.  $\gamma$  is the polytropic index and depends whether the plasma is considered isothermal ( $\gamma = 1$ ), adiabatic ( $\gamma = 5/3$ ) or has constant pressure ( $\gamma = 0$ ). In the scope of this work, the plasma is considered adiabatic, i.e.  $\epsilon = 3/2p$ . The internal energy in the energy equation (3.9) can be substituted by the pressure and we can derive an evolution equation for the pressure:

$$\frac{\partial p}{\partial t} + \mathbf{v} \cdot \nabla p + \gamma p \nabla \cdot \mathbf{v} = 0 \quad (3.15)$$

Equation (3.13) states that the magnetic field is solenoidal and therefore magnetic monopoles do not exist. Thus, equations (3.7), (3.8), (3.14) and (3.15) with the constraint of equation (3.13) is a set of eight coupled scalar differential equations with eight scalar unknowns  $\mathbf{B}, \mathbf{v}, \rho$  and  $p$  and forms a closed system, referred to here as ideal single fluid MHD equations. Since the single fluid MHD equations are derived from the multi-fluid MHD equations, we will shortly describe the combined quantities  $\rho, p$  and  $\mathbf{v}$  in terms of the quantities of ions with subscripts  $i$  and electrons with subscript  $e$ . The pressure is just a combination of the partial pressures of each species  $p = p_i + p_e$ . The same is true for the density  $\rho = \rho_i + \rho_e$ , which is dominated by the much heavier ions. Also the momentum is mainly carried by the ions:

$$\mathbf{v}\rho = \mathbf{v}_i\rho_i + \mathbf{v}_e\rho_e, \quad (3.16)$$

which means that the bulk velocity is also determined by the movement of the ions. The current density  $\mathbf{j}$ , which is the relative movement of ions and electrons, can be described as

$$\mathbf{j} = ne(\mathbf{v}_i - \mathbf{v}_e). \quad (3.17)$$

### 3.1.1. Ideal MHD Waves

Using the linearized ideal MHD equations for small perturbations in velocity  $\delta\mathbf{v}$ , magnetic field  $\delta\mathbf{B}$ , density  $\rho$ , and pressure  $p$ , one can derive a set of ideal MHD wave modes. These are called the slow and fast magnetosonic modes and the Alfvén mode. The dispersion relation for the magnetosonic modes (e.g. Baumjohann and Treumann (2012)) is given by

$$\omega^2 = \frac{k^2}{2} \left[ v_A^2 + c_s^2 \pm \sqrt{(v_A^2 + c_s^2)^2 - 4v_A^2 c_s^2 \cos^2(\theta)} \right], \quad (3.18)$$

where  $\omega$  is the wave frequency,  $k$  the wavenumber,  $\cos\theta = k_{\parallel}/k$  the angle between  $\mathbf{k}$  and the background magnetic field and  $v_A$  and  $c_s$  the Alfvén speed and magnetosonic speed,

respectively. They are given by

$$\mathbf{v}_A = \frac{\mathbf{B}}{\sqrt{\mu_0 \rho}} \quad (3.19)$$

and

$$c_s = \sqrt{\frac{\gamma p}{\rho}}. \quad (3.20)$$

Equation (3.18) is both the dispersion relation for the magnetosonic slow mode and fast mode, depending on the sign before the square root. In case of a negative sign, the dispersion relation for the slow mode is given, in case of a positive sign, the dispersion relation describes the fast mode. It can be seen, that for a propagation along the magnetic field line, i.e.  $\cos \theta = 1$ , Equation (3.18) gives us

$$\frac{\omega^2}{k^2} = \frac{1}{2} (v_A^2 + c_s^2 \pm |v_A^2 - c_s^2|). \quad (3.21)$$

Hence, if  $v_A > c_s$ , the fast mode propagates with the Alfvén speed along the magnetic field lines. However, if  $c_s > v_A$ , the slow mode propagates with the Alfvén speed along the magnetic field line. The dispersion relation for the Alfvén mode is given by

$$\omega = \mathbf{v}_A \cdot \mathbf{k} = v_A k \cos \theta. \quad (3.22)$$

The group velocity  $\nabla_k \omega$  of the Alfvén mode is therefore only parallel or anti-parallel to the magnetic field. This is an important property of the Alfvén mode. Since in the MHD framework, it is also not dispersive ( $\omega/k = v_A \cos \theta = \text{const.}$ ), its energy density is conserved while propagating along the magnetic field lines. Therefore, it can have far field interactions and can couple systems, that are very distant from each other. One example is the moon-planet or star-planet interaction via Alfvén wings (Neubauer, 1980). Their physics and theoretical framework is discussed in detail in Chapter 4. The phase velocity diagram for all three modes for different angles  $\theta$  is shown in Figure 3.1. The phase velocity for any angle is shown as the distance  $r(\theta)$  from the center. As discussed, the phase velocity (anti-)parallel to the background magnetic field of either the fast mode or the slow mode matches the Alfvén velocity. Furthermore, the fast mode is the only mode with a potential pure perpendicular phase velocity. Like the Alfvén mode, the slow mode mainly propagates along the magnetic field line. It perturbs the velocity  $\delta v_{\parallel}$  parallel to the wave vector  $\mathbf{k}$ . This longitudinal perturbation is connected to a perturbation in pressure

$$\delta p = \gamma \frac{p}{c_s} \delta v_{\parallel} \quad (3.23)$$

and density

$$\delta \rho = \frac{\rho}{c_s} \delta v_{\parallel}. \quad (3.24)$$

Contrary to the slow mode, the Alfvén wave is a non-compressional and transversal wave in the MHD limit. It perturbs the magnetic field and the velocity  $\delta \mathbf{v}_{\perp}$  perpendicular to the background magnetic field. The magnetic field perturbation is connected to the velocity perturbation by

$$\delta \mathbf{B} = \mp \sqrt{\mu_0 \rho} \delta \mathbf{v}_{\perp}. \quad (3.25)$$

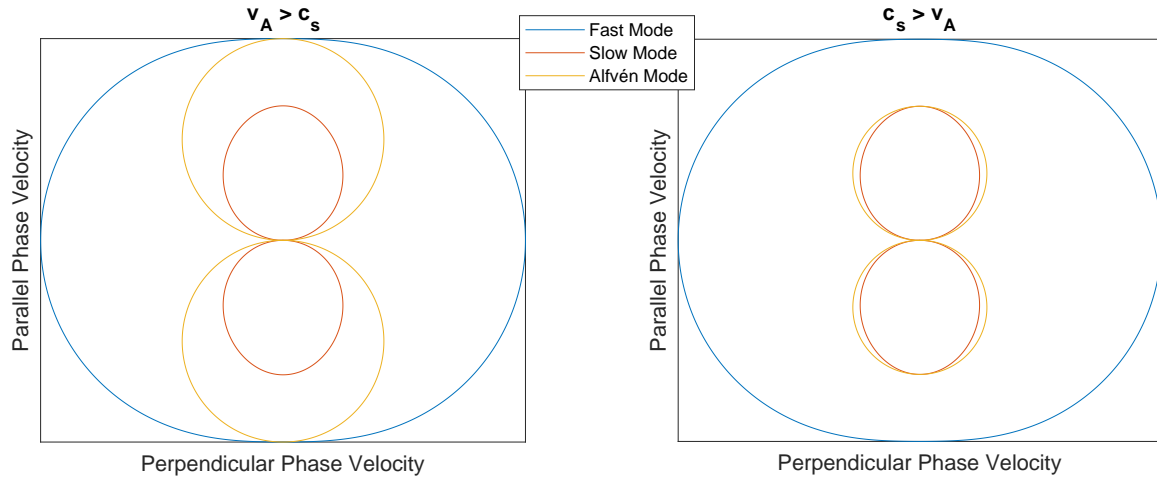


**Figure 3.1.:** Sketch of the phase velocity of the fast magnetosonic mode (blue), the slow magnetosonic mode (red) and the Alfvén mode (yellow) in the case of  $v_A > c_s$  (left) and  $c_s > v_A$  (right). The phase velocity for an angle  $\theta$  is given by the distance of the respective curve from the center. The phase velocity parallel and anti-parallel to the background field, i.e.  $\theta = 0^\circ, 180^\circ$ , is shown along the y-axis.

The different signs in equation (3.25) are for the different propagation directions, parallel (minus) and anti-parallel (plus) to the magnetic field. The restoring force in the Alfvén wave is the magnetic tension

$$I = \frac{(\mathbf{B} \cdot \nabla)\mathbf{B}}{\mu_0}. \quad (3.26)$$

Even though the magnetic field is perturbed by the Alfvén wave, it does not change the magnitude of the magnetic field strength and the magnetic pressure

$$p_B = \frac{B^2}{2\mu_0} \quad (3.27)$$

remains unchanged.

## 3.2. Alfvén Waves in an Inhomogeneous Medium

In the Jovian magnetosphere the assumption that the background magnetic field or density are constant does not necessarily apply. Even though the magnetic field varies slowly, the high density gradients at the Io torus boundary and Jupiter’s ionosphere trigger reflections and refraction of the incoming Alfvén waves. In this section, we will only cover reflection and refraction of small amplitude waves and will only discuss linear effects.

### 3.2.1. Reflection and Transmission at Discontinuities

We will first look into discontinuities, where the refractive index changes on length scales much smaller than the wavelength. The refractive index  $n$  here is the relative change in phase velocity of the wave. If the magnetic field is assumed to be constant, the phase velocity changes due to density gradients.

$$n = \frac{v_A(\mathbf{r})}{v_{A,0}} = \sqrt{\frac{\rho_0}{\rho(\mathbf{r})}} \quad (3.28)$$

The gradient length scale  $L_n = 1/|\mathbf{e}_z \cdot \nabla \log(n)|$  of the relative change in  $n$  can be calculated as the inverse of the relative gradient of  $n$  in direction of the wave propagation, here denoted as  $x$ . Since the phase velocity gradient here is mainly due to the change in density, the condition for a discontinuity reads

$$\lambda \left| \frac{\partial \log(\rho/\rho_0)}{\partial z} \right| \ll 1. \quad (3.29)$$

For an exponential increasing or decreasing density, as it is the case at Jupiter's ionosphere, this simplifies to  $\lambda H \ll 1$ , with  $H$  being the scale height. Even regarding high frequency Alfvén waves with frequencies of multiple times the characteristic frequency  $f_0 = \frac{1}{\tau} \approx 0.01$  Hz (Deift and Goertz, 1973), the assumption of a discontinuity is well fulfilled at Jupiter's ionosphere, because the wave in the high latitude region of Jupiter's inner magnetosphere travels with velocities close to the speed of light.

For discontinuities, the reflection coefficient  $R$  and transmission coefficient  $T$  of the magnetic field perturbation  $\delta \mathbf{B}$  and the velocity perturbation  $\delta \mathbf{v}$  can be calculated as (e.g. Wright (1987)):

$$R = R_{B,v} = \frac{n_2 - n_1}{n_2 + n_1} \quad (3.30)$$

$$T_v = \frac{2n_1}{n_2 + n_1} \quad (3.31)$$

$$T_B = \frac{2n_2}{n_2 + n_1} \quad (3.32)$$

Because the proportionality factor between magnetic field perturbation and velocity perturbation is not constant (see Equation (3.25)), the transmission coefficients for magnetic field  $T_B$  and velocity  $T_v$  differ from each other, even though their respective reflection coefficients are the same. Depending on the type of discontinuity, either the magnetic field perturbation or the velocity perturbation changes sign. For an increase in phase velocity, i.e. a negative density gradient, the magnetic field perturbation changes sign  $\delta \mathbf{B}_r = \mp R \delta \mathbf{B}_i$ . In the case of a decrease in phase velocity, i.e. a positive density gradient as it is at Jupiter's ionosphere, the velocity perturbation changes sign  $\delta \mathbf{v}_r = \pm R \delta \mathbf{v}_i$ . This means that the Poynting flux always changes sign when reflected and the reflection coefficient  $R_S$  and transmission coefficient  $T_S$  for the Poynting flux can be calculated as

$$R_S = R^2 = \frac{(n_2 - n_1)^2}{(n_2 + n_1)^2} \quad (3.33)$$

$$T_S = 1 - R_S = T_B T_v = \frac{4n_2 n_1}{(n_2 + n_1)^2}. \quad (3.34)$$

### 3.2.2. The WKB Approximation

The *Wentzel-Kramers-Brillouin* (WKB) approximation is applied in an inhomogeneous medium, when the wavelength is much smaller than the gradient length scale, i.e.  $\lambda \ll L_n$ . In this case, the medium does not change significantly for the wave. Deift and Goertz (1973) discussed the propagation of Alfvén waves in the inner Jovian magnetosphere under

the aspect of the WKB approximation. To recapture their results, we will introduce the substitutions they made in their work:

$$a = \frac{\delta v \sqrt{\mu_0 \rho}}{B_0} \quad (3.35)$$

$$\tau = \frac{B_0 t}{\sqrt{\mu_0 \rho_0}} \quad (3.36)$$

$$\beta = \sqrt{\frac{\rho}{\rho_0}} = \frac{v_{A,0}}{v_A}. \quad (3.37)$$

Here,  $a$  can be regarded as the ratio between velocity perturbation  $\delta v$  and alfvénic phase velocity  $v_A$ . Therefore, we can write a simplified equation for the Alfvén wave as

$$\frac{\partial^2 a}{\partial z^2} - \beta(z)^2 \frac{\partial^2 a}{\partial \tau^2} = 0 \quad (3.38)$$

Since the density is not homogeneous, i.e.  $\beta$  is not constant, this wave equation can not generally be solved analytically. To get an approximation, they assume the solution has the form  $a = a_0 \exp(i(\omega\tau + \Phi(z)))$  with the generalized frequency  $\omega$ , which leads to

$$- \left( \frac{\partial \Phi}{\partial z} \right)^2 + i \frac{\partial^2 \Phi}{\partial z^2} + \omega^2 \beta^2 = 0 \quad (3.39)$$

In the case of slowly varying medium, where we can neglect the second derivative of  $\Phi(z)$ , we get the WKB solution

$$\Phi = \pm \int \omega \beta dz. \quad (3.40)$$

This is true, when  $\frac{\partial^2 \Phi}{\partial z^2} \ll \omega^2 \beta^2$  or when the length scale of the relative change in phase velocity is large against the wavelength, i.e.  $\lambda \frac{\partial(\log v_A)}{\partial z} \ll 1$  (cf. Equation (3.29)). In that case the velocity perturbation can be written as

$$\delta v = \delta v_0 \frac{v_A}{v_{A,0}} \exp \left( i 2\pi f \left( t \pm \int \frac{1}{v_A} dx \right) \right), \quad (3.41)$$

with  $f$  being the real frequency of the wave. This is the equation of a wave in a slowly changing medium where no reflections occur and the wave does not lose energy. The velocity perturbation amplitude of the wave scales with  $v_A$ . Assuming the magnetic field stays constant and with equation (3.25) to connect the magnetic field perturbation with the velocity perturbation, we get

$$\delta v \propto \rho^{-1/4} \quad (3.42)$$

$$\delta B \propto \rho^{1/4} \quad (3.43)$$

in accordance to the findings by Wright (1987). As mentioned in the previous section, the energy of the wave which is carried by the Poynting flux  $\mathbf{S}$  is therefore conserved, detailed in Appendix B.4.

### 3.2.3. Reflection in Slowly Changing Media

The WKB approximation holds when the length scale of the Alfvén velocity gradient is much larger than the wavelength. When Deift and Goertz (1973) proposed it for the inner Jovian magnetosphere, they concluded that it holds for the whole Io flux tube excluding only the vicinity of the Jovian ionosphere. However, when the Io plasma torus was discovered, this had to be reevaluated. Especially near the torus boundary this approximation does not necessarily hold anymore. But the torus boundary can also not be described as a discontinuity with the reflection coefficient introduced as in Equation (3.30). To understand this better, it is helpful to imagine a medium with slowly changing refractive index  $n(x) = n_0 + \alpha x/x_1$  over a domain  $x \in [0, x_1]$ . If we use Equation (3.30), the reflection coefficient would be  $R = \alpha/(2n_0 + \alpha)$ . This equation only holds when the wavelength  $\lambda > x_1/\alpha$  is much larger than the lengths scale associated with the change in refractive index. The reason for this is that the reflected wave has only constructive interference with itself, i.e. all waves reflected at a boundary in the range of  $0 < x < x_0$  have practically the same phase. This changes for smaller wavelengths. In this case we have to sum up all reflections at the boundary. For this let us look at a wave with wave number  $k = 2\pi/\lambda$  with phase  $\phi_0$  at  $x = 0$  and regard the slowly changing refractive index as a superposition of step functions with width  $\delta x$ . At each step, the wave is reflected regarding Equation (3.30) using the reflection coefficient

$$\delta R = \frac{\delta n}{2n(x) + \delta n}, \quad (3.44)$$

with  $\delta n = \alpha \delta x/x_1$ . We want to look at the superposition of all those waves before the boundary at  $x_0 = 0$ . Each reflected wave, indicated with  $j$ , has the amplitude  $\delta R_j$  and the phase shift

$$\Delta\phi_j = \Delta\phi_0 - 2 \int_0^{x_j} k(x') dx'. \quad (3.45)$$

$\Delta\phi_0$  is either 0 or  $\pi$ , depending if there is a phase shift at the point of reflection, while the second term is the phase change due to the propagation towards the point of reflection and the propagation back to  $x_0 = 0$ . From equations (3.44) and (3.45) the complex amplitude for each reflected wave can be written as

$$r_j = A_j \delta R(x_j) e^{i(\phi_0 + \Delta\phi(x_j))}, \quad (3.46)$$

where  $x_j$  is the location of reflection and  $A_j$  is the amplitude of the transmitted wave at  $x_j$ . To solve Equation (3.46) analytically, we introduce the following simplifications: First, we say that the wave number  $k$  does not change noticeably in the domain, therefore  $\int k(x') dx' \approx kx_j$ . This is connected to the second approximation, where we treat the refractive index as constant in the denominator of equation (3.44), leading to  $2n(x) + \delta n \approx 2n_0 + \alpha =: \bar{n}$ . Third, we assume that the amplitude of the incident wave does not diminish significantly in the domain. This leads to  $A_j = A_0$  in equation (3.46) and consequently to

$$r_j = \left( A_0 \frac{\alpha \delta x}{\bar{n} x_1} e^{i(\phi_0 + \Delta\phi_0)} \right) e^{-2ik_0 x_j}. \quad (3.47)$$

The total reflected wave amplitude  $r$  at  $x_0 = 0$  is now a superposition of all waves  $r_j$ . To make this approach more rigorous we introduce infinitesimal step lengths  $\delta x \rightarrow dx$  and

integrate:

$$r = \left( A_0 \frac{\alpha}{\bar{n}x_1} e^{i(\phi_0 + \Delta\phi_0)} \right) \int_{x_0=0}^{x_1} e^{-2ik_0x} dx. \quad (3.48)$$

Carrying out the integration and calculating the absolute value gives us the amplitude of the reflected wave

$$\begin{aligned} A_r &= ||r|| \\ &= A_0 \frac{\alpha}{\bar{n}x_1} \frac{1}{2k_0} ||e^{-2ik_0x_1} - 1|| \\ &= A_0 \frac{\alpha}{\bar{n}x_1} \frac{1}{2k_0} \sqrt{(\cos(2k_0x_1) - 1)^2 + \sin^2(2k_0x_1)} \\ &= A_0 \frac{\alpha}{\bar{n}x_1} \frac{1}{k_0} |\sin(k_0x)| \\ &\approx A_0 \frac{\alpha}{\bar{n}x_1} \frac{\lambda_0}{\sqrt{8\pi}} \end{aligned} \quad (3.49)$$

The last step is the zeroth order Taylor expansion for small wavelengths  $\lambda_0 = 2\pi/k_0 \ll x_1$ . This result reveals some interesting behaviors. There are wave numbers, that have total destructive interference, when the width of the discontinuous domain  $x_1$  is a multiple of  $\lambda/4$ . Furthermore, in the limit of long wavelengths  $k_0x_1 \ll 1$ , i.e. the second order Taylor expansion for small wavenumbers, the reflected amplitude approaches

$$A_r = A_0 \frac{\alpha}{\bar{n}} \left( 1 - \frac{(k_0x_1)^2}{6} \right). \quad (3.50)$$

This let us subdivide the effective reflection coefficient  $R_{eff} = A_r/A_0$  into three wavelength regimes as shown in Figure 3.2. At the WKB limit up to a wavelength of about  $\lambda \approx 4x_1$ ,  $R_{eff} \propto \lambda$  increases linearly including some local minima. After that,  $R_{eff}$  rises with increasing  $\lambda$  and asymptotically reaches the reflection coefficient  $R$  of a discontinuity. Since in the Jovian inner magnetosphere almost all wave numbers are large compared to the Alfvén velocity gradient, i.e.  $k_{||} \gg |\nabla n|$ , the reflection coefficient is proportional to the wavelength and therefore the Alfvén velocity and the relative change in refractive index  $\nabla n/n = \nabla \log(n)$  (e.g. Hess et al. (2010))

$$R_{eff} \propto \mathbf{v}_A \cdot \nabla \log(n) \quad (3.51)$$

In this section we saw that when we have a slowly changing medium parts of the transmitted wave at a location  $0 < x_j < x_0$  undergo a phase shift, which is not negligible. Superposition of reflected wave amplitude contributions from varying locations along the gradient lead to a modified reflection coefficient compared to the discontinuous approach. Hence, a continuous medium can not be decomposed into a sequence of discontinuous segments in order to determine the resulting amplitude of the reflected wave.

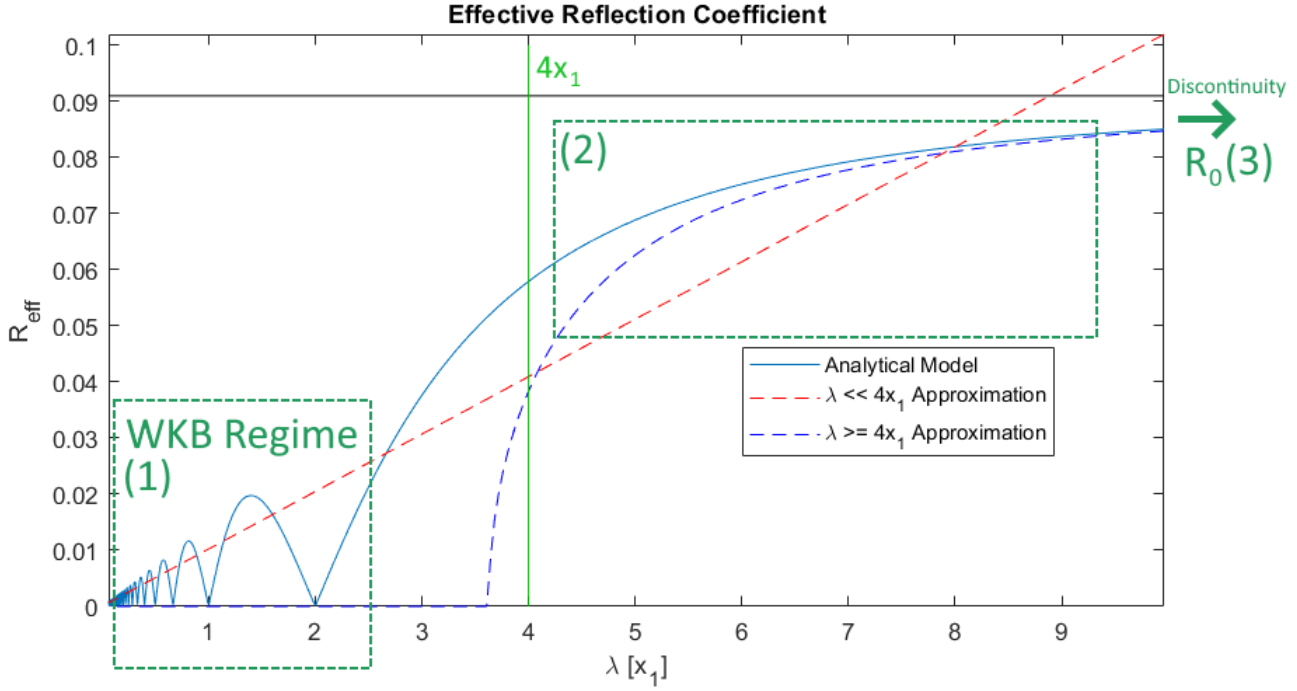


**Figure 3.2.:** The effective reflection coefficient  $R_{eff}$  for different wavelengths can be divided into different regimes. The analytical solution of Equation (3.49) is shown as solid line. For wavelengths small compared to the length scale of the change in refraction index, also referred to as the WKB regime (1), the average  $R_{eff}$  grows linearly, corresponding to the last line in Equation (3.49) as shown by the red dashed line. When the wavelengths and length scale are comparable (2),  $R_{eff}$  grows as shown by the blue dashed line in accordance to Equation (3.50). It asymptotically reaches the reflection coefficient  $R_0$  of a discontinuity with the same overall change in refractive index (3).

### 3.3. The Hall Effect

The derivations in this section are also found in the general literature, e.g. Baumjohann and Treumann (2012); Chen et al. (1984). From the equation for the current density (3.17), we see that we can build the difference of the two fluid evolution equations for the velocities of ions and electrons to derive an evolution equation for the current density  $\mathbf{j}$ . With the quasi neutrality condition  $n = n_i = n_e$ , neglecting quadratic terms in velocity, i.e. the advection terms, and using the fact that electron mass is much smaller than the ion mass ( $m_e/m_i \ll 1$ ), the current density evolution equation for the single fluid MHD reads:

$$\frac{m_e}{e} \frac{\partial \mathbf{j}}{\partial t} = \nabla p_e + ne(\mathbf{E} + \mathbf{v}_e \times \mathbf{B}) - \eta ne \mathbf{j}, \quad (3.52)$$

with the electron pressure  $p_e$  and electron mass  $m_e$ . The last term here is due to the collisions between ions and electrons with the resistivity  $\eta$ . Since they do not change the total momentum of the plasma, this term does not appear in the single fluid velocity equation. We now use the already mentioned fact that the velocity of the single fluid plasma is mainly determined by the velocity of the ions  $\mathbf{v} \approx \mathbf{v}_i$  and the velocity of the electrons can therefore be stated as  $\mathbf{v}_e = \mathbf{v} - \mathbf{j}/ne$ . This leads to the generalized Ohm's law of the single fluid MHD:

$$\mathbf{E} + \mathbf{v} \times \mathbf{B} = \frac{1}{ne} \mathbf{j} \times \mathbf{B} + \eta \mathbf{j} - \frac{1}{ne} \nabla p_e + \frac{m_e}{ne^2} \frac{\partial \mathbf{j}}{\partial t}. \quad (3.53)$$

When the right hand side is small against the electric field  $\mathbf{E}$ , we can state Ohm's law as in equation (3.11). As can be seen, mostly the electron pressure adds to the current density. Furthermore, the resistive term  $\eta \mathbf{j}$  due to electron-ion collisions results in a diffusion of the magnetic field if we include it in the induction equation. The first term on the right hand side is the Hall term. If we ignore all other terms on the right hand side, the electric field can be written as

$$\mathbf{E} = - \left( \mathbf{v} - \frac{1}{ne} \mathbf{j} \right) \times \mathbf{B} = -\mathbf{v}_e \times \mathbf{B} \quad (3.54)$$

This means, that only the electrons are frozen into the magnetic field. The ions however react slower to changes in magnetic flux and their movement can therefore deviate on small time scales. If the Hall term is included, the induction equation reads

$$\frac{\partial \mathbf{B}}{\partial t} = \nabla \times \left( \mathbf{v} \times \mathbf{B} - \frac{m}{\rho e} \mathbf{j} \times \mathbf{B} \right) \quad (3.55)$$

### 3.4. Collision and Production in MHD

In the vicinity of a planetary object, space is not only filled with plasma but also with neutral particles. On the one hand these particles can be ionized, for example by photoionization, electron impact or charge exchange. On the other hand they can act as collision partners for the plasma particles. In this section, we will see how collision and production arise in different terms in the MHD equations and how they can physically be understood. Even though the production is not used in the forthcoming simulations, its implication will be discussed and whether it can be neglected. Both, collision and production, can be seen as source terms in the Vlasov equation (3.1). The full evolution equation for the phase space density distribution  $f(\mathbf{r}, \mathbf{v})$  then reads

$$\frac{\partial f}{\partial t} + \mathbf{v} \cdot \nabla f + \frac{\mathbf{F}}{m} \cdot \nabla_v f = \left( \frac{\partial f}{\partial t} \right)_C + \left( \frac{\partial f}{\partial t} \right)_P. \quad (3.56)$$

The velocity moments of the left hand side of (3.56) gives us the already known MHD equations for density (3.7), velocity (3.8) and energy (3.9). Building the velocity moments for the right hand side therefore leads to source and sink terms for those equations. First, we need to define the two terms. Here, we use the most simple description of the collision term. The collision cross section does not depend on the relative velocity between the particles or the angle. The collision term reads (Schunk, 1975)

$$\left( \frac{\partial f}{\partial t} \right)_C = \frac{\nu}{n_n} (n f_n - n_n f) = \nu \left( \frac{n}{n_n} f_n - f \right). \quad (3.57)$$

In this description,  $\nu$  is the collision frequency,  $n_n$  is the number density of the neutral particles  $n$  the plasma number density and  $f$  and  $f_n$  the phase space density distributions for the plasma and neutral particles, respectively. It is important to note that the collision frequency here is an averaged ensemble value and does not reflect the true number of

collisions a single particle experiences. The first term can be understood as the transfer of momentum from the neutral particle to the plasma particle, whereas the second term is the transfer of momentum from the plasma particle to the neutral collision partner. Whether the neutral particles are considered to have pressure  $p_n$  or a bulk velocity  $\mathbf{v}_n$  depends on the nature of  $f_n$  and can be calculated analogous to equations (3.2) to (3.4). For particle production, we assume that  $N$  particles with a constant velocity  $\mathbf{v}_0$  are produced with frequency  $P/N$ . The unit of  $P$  is therefore  $[P] = \text{cm}^{-3} \text{s}^{-1}$ . This leads us to a simple description of the production term

$$\left(\frac{\partial f}{\partial t}\right)_P = P\delta(\mathbf{v} - \mathbf{v}_0) \quad (3.58)$$

Here, we will only state the MHD equations with the derived source and sink terms arising from the collision and production terms. A more detailed derivation is shown in appendix A. These equations are in agreement with Schunk (1975), Chané et al. (2013) and Blöcker et al. (2018). The new set of non-ideal MHD equations for density, velocity and pressure can now be stated as:

$$\frac{\partial \rho}{\partial t} + \nabla \cdot (\rho \mathbf{v}) = mP \quad (3.59)$$

$$\rho \frac{\partial \mathbf{v}}{\partial t} + \rho \mathbf{v} \cdot \nabla \mathbf{v} = -\nabla p + \frac{1}{\mu_0} (\nabla \times \mathbf{B}) \times \mathbf{B} + \nu \rho (\mathbf{v}_n - \mathbf{v}) + mP(\mathbf{v}_0 - \mathbf{v}) \quad (3.60)$$

$$\frac{\partial p}{\partial t} + \mathbf{v} \cdot \nabla p + \gamma p \nabla \cdot \mathbf{v} = \frac{\nu \rho}{2} (\mathbf{v}_n - \mathbf{v})^2 + \nu (p_n - p) + \frac{m}{2} P (\mathbf{v}_0 - \mathbf{v})^2 \quad (3.61)$$

The red terms correspond to particle collisions while the blue terms are due to particle production. Note, that there is no pressure associated with the particle production, since we defined the produced particles to have a defined velocity  $\mathbf{v}_0$ . We will now discuss each term to understand the underlying physics. The production term in the continuity equation (3.59) is simply the production of new mass. Collisions do not change the plasma density, therefore no collision term shows up in the continuity equation. In the velocity equation (3.60), the collisions exert a force on the plasma relative to the velocity difference. This causes the plasma to approach the velocity of the neutral particles  $\mathbf{v}_n$ . The production term works in a similar way. The newly generated particles have all the same speed  $\mathbf{v}_0$  which causes the mean velocity of the plasma to approach the velocity of the newly generated particles. However, unlike the collision term, the production term changes, when we consider the momentum equation instead of the velocity equation:

$$\left(\frac{\partial \rho \mathbf{v}}{\partial t}\right)_P = mP\mathbf{v}_0 \quad (3.62)$$

The production term adds constant momentum to the plasma. In the rest frame of the newly generated particles, i.e.  $\mathbf{v}_0 = 0$ , the momentum change due to the production is zero. If the calculations are performed in the reference frame of the neutral gas, the velocity of produced and neutral particles can sometimes be considered to be zero. Then the sink term in the velocity equation simplifies to

$$\left(\rho \frac{\partial \mathbf{v}}{\partial t}\right)_{C,P} = -\mathbf{v}(\nu \rho + mP). \quad (3.63)$$

In the pressure equation (3.61), the first term considers the kinetic energy exchange between neutral particles and plasma. In the rest frame of the neutral particles, i.e.  $\mathbf{v}_n = 0$ , the plasma loses kinetic energy in the shape of bulk velocity as it can be seen in the velocity equation (3.60). This energetic loss however is partly balanced by a increase in pressure. The same mechanism takes place considering the production term in Equation (3.61). The second source term in this equation relates the pressure exchange by collisions between neutrals and plasma particles. Sometimes, one can assume  $\mathbf{v}_n = \mathbf{v}_0$ , when the neutrals that get ionized do not gain or lose considerable energy in the process. If we now neglect pressure of the neutrals and do not consider the continuity equation, collision and production act exactly the same. We therefore can combine production and collision to an effective collision frequency

$$\nu^* = \nu + \frac{P}{n}. \quad (3.64)$$

In this work, the simulations are carried out in the rest frame of Io and therefore  $\mathbf{v}_n = \mathbf{v}_0 = 0$  holds. Neglecting the production in the continuity equation, the set of differential equations are

$$\frac{\partial \rho}{\partial t} + \nabla \cdot (\rho \mathbf{v}) = 0 \quad (3.65)$$

$$\rho \frac{\partial \mathbf{v}}{\partial t} + \rho \mathbf{v} \cdot \nabla \mathbf{v} = -\nabla p + \frac{1}{\mu_0} (\nabla \times \mathbf{B}) \times \mathbf{B} - \nu \rho \mathbf{v} \quad (3.66)$$

$$\frac{\partial p}{\partial t} + \mathbf{v} \cdot \nabla p + \gamma p \nabla \cdot \mathbf{v} = \frac{\nu \rho}{2} v^2 - \nu p. \quad (3.67)$$

### 3.5. Pedersen and Hall Conductance

In ideal MHD, the conductivity of the plasma along the magnetic field line is nearly infinite, while particles can not easily move perpendicular to the magnetic field. This changes, when we consider collisions. Here, we will explain the currents due to collisions in the single particle picture. Afterwards, we derive the equations for the currents arising from drift motions and show that they agree with similar considerations in the MHD framework.

In the single particle picture, the charged particles of the plasma move along the flow perpendicular to the magnetic field as the result of the  $\mathbf{E} \times \mathbf{B}$  drift. At the same time, the particle gyrates around the magnetic field line with the gyrofrequency  $\Omega$ . When a particle collides with a neutral, it changes direction and is therefore shifted depending on the current relative velocity to the neutral particle at the time of the collision. Due to the electric field the particle on average has a velocity in the  $\mathbf{E} \times \mathbf{B}$  direction and the shift is not random, but has a preferred direction. Ions are shifted parallel to the electric field, while electrons are shifted anti-parallel to it. This displacement can be regarded as the Pedersen current on a single particle level. Exemplarily, Figure 3.3 shows a sketch of trajectories for an ion and an electron, each with and without collisions. As it can be seen, the Pedersen current results from a net shift of the particles towards larger gyroradii. The increase of the gyroradius follows from the conservation of total energy  $E_{tot} = E_{kin} - qU$  of the particle, where  $q$  is the particles charge,  $U$  is the electric potential and  $E_{kin} = 1/2mv^2$  is the particles kinetic energy. When the particle shifts to lower potential energy, the kinetic energy increases. Since the displacement of electrons and ions is opposed to each

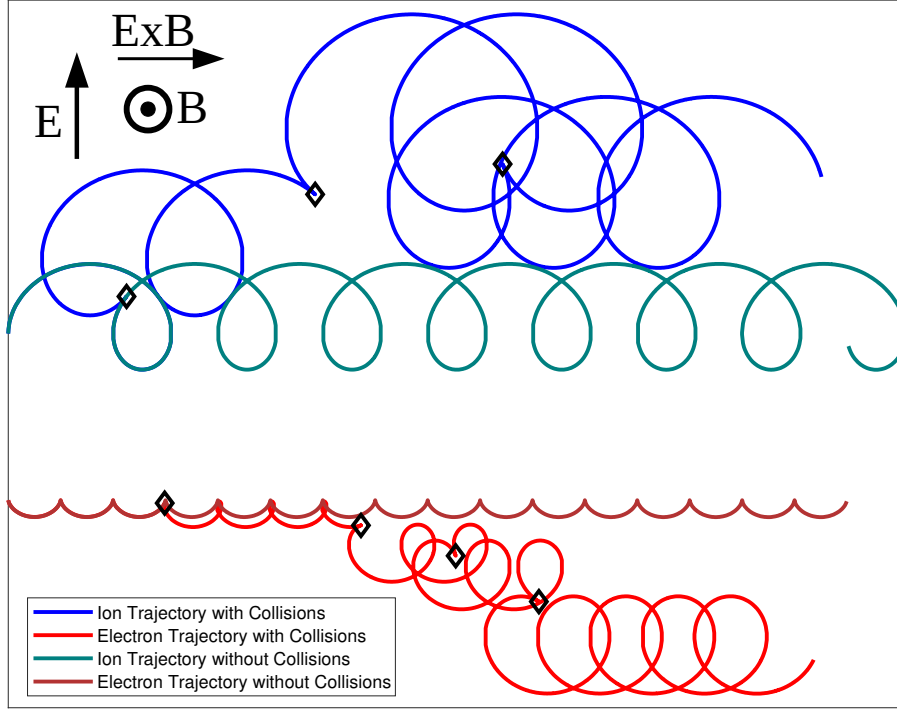


**Figure 3.3.:** Sketch of the particle displacement due to collisions. The blue and green lines are the trajectories of the ion with and without collisions, respectively. The ion that experiences collisions is shifted in the direction of the electric field and along  $-\mathbf{E} \times \mathbf{B}$ . The red and brown lines are the trajectories of the electron with and without collisions, respectively. The electron that collides with the neutrals is shifted anti-parallel to the electric field and along  $-\mathbf{E} \times \mathbf{B}$ . The locations of collisions are marked as black diamonds.

other, both species add to the Pedersen currents in the direction of  $\mathbf{E}$ .

The collisions also hinder the particles to move freely with their  $\mathbf{E} \times \mathbf{B}$  drift velocity. This can be seen in Figure 3.3 as ions and electrons don't move as far to the right, when collisions occur. This is the reason behind the Hall current. Since this shift is in the same direction for ions and electrons, the Hall current can be parallel to  $\mathbf{E} \times \mathbf{B}$ , when the slowdown of the electrons dominates, and anti-parallel, when the slowdown of the ions dominates.

To derive the equations of Hall and Pedersen currents, we will first calculate the drift motion of the particles with the help of general force drift. If we have a force  $\mathbf{F}$  acting on a particle with mass  $m$  and charge  $q$  in a background magnetic field  $\mathbf{B}$ , the drift  $\mathbf{v}_\perp$  perpendicular to the magnetic field can be calculated as

$$\mathbf{v}_\perp = \frac{1}{qB^2} \mathbf{F} \times \mathbf{B}. \quad (3.68)$$

We consider here two forces acting on the particles. First the Coulomb force  $\mathbf{F}_E = q\mathbf{E}$  due to a background electric field  $\mathbf{E}$  perpendicular to the background magnetic field. Second, the force due to collisions  $\mathbf{F}_{Col} = -\nu m \mathbf{v}$ , that slows the particle down with an effective collision frequency  $\nu$ , which can be regarded as the number of collisions per time that occur multiplied with the relative change in momentum per collisions. If we insert the forces into equation (3.68), we get

$$\mathbf{v}_\perp = \frac{\mathbf{E} \times \mathbf{B}}{B^2} - \frac{\nu m}{qB^2} \mathbf{v}_\perp \times \mathbf{B}. \quad (3.69)$$

With the definition of the gyrofrequency  $\Omega = \pm|q|B/m$ , with the positive sign for ions and negative sign for electrons, the drift velocity can be written as

$$\mathbf{v}_\perp = \frac{1}{B} \left( \underbrace{\frac{\nu\Omega}{\nu^2 + \Omega^2} \mathbf{E}}_{\text{Pedersen Drift}} + \underbrace{\frac{\Omega^2}{\nu^2 + \Omega^2} \frac{\mathbf{E} \times \mathbf{B}}{B}}_{\text{Hall Drift}} \right). \quad (3.70)$$

The first term in Equation (3.70) is the Pedersen drift. It is parallel to  $\mathbf{E}$  for ions and anti-parallel for electrons. For low collision frequencies  $\nu \ll \Omega$ , the drift increases linearly with  $\nu$  and reaches its maximum for  $\nu = \Omega$ . However, in the case of  $\nu \gg \Omega$  the many collisions hinder the particles to complete their gyromotions. This results in the particles to stay in place and the Pedersen drift tends to zero. The second term in Equation (3.70) is the Hall drift and points in  $\mathbf{E} \times \mathbf{B}$  direction for both species. However, this drift is generally slower than the  $\mathbf{E} \times \mathbf{B}$  drift without collisions. As for the Pedersen drift, high collision frequencies decelerates the particles and the Hall drift motion comes to rest. We can calculate the current density  $\mathbf{j} = \sum n_s q_s \mathbf{v}_s$  resulting from the sum of the drift motion of all species  $s$ . Here, we assume the particles to be single charged, i.e.  $q_i = e$  and  $q_e = -e$ , and use quasi neutrality  $n_i = n_e = n$ . The current with the gyrofrequencies  $\Omega_e = eB/m_e$  and  $\Omega_i = eB/m_i$  and collision frequencies  $\nu_e$  and  $\nu_i$  for electrons and ions, respectively, yields

$$\mathbf{j} = \frac{ne}{B} \left( \left( \frac{\nu_i \Omega_i}{\nu_i^2 + \Omega_i^2} + \frac{\nu_e \Omega_e}{\nu_e^2 + \Omega_e^2} \right) \mathbf{E} + \left( \frac{\Omega_i^2}{\nu_i^2 + \Omega_i^2} - \frac{\Omega_e^2}{\nu_e^2 + \Omega_e^2} \right) \frac{\mathbf{E} \times \mathbf{B}}{B} \right). \quad (3.71)$$

As discussed previously, the Pedersen current, i.e. the first term in equation (3.71) always points in the direction of  $\mathbf{E}$  and the currents due to electron and ion drift add up. The Hall current, which is represented by second term in equation (3.71), points parallel to  $\mathbf{E} \times \mathbf{B}$ , if the electron collisions dominate, i.e. when  $\nu_e/\Omega_e > \nu_i/\Omega_i$ , but anti-parallel in the case of dominating ion collisions. If we only consider ion collisions with  $\nu = \nu_i$  and  $\Omega = \Omega_i$ , Equation (3.71) simplifies to

$$\mathbf{j} = \frac{ne}{B} \left( \sigma_P \mathbf{E} - \sigma_H \frac{\mathbf{E} \times \mathbf{B}}{B} \right), \quad (3.72)$$

with the Pedersen conductivity

$$\sigma_P = \frac{ne}{B} \frac{\nu\Omega}{\nu^2 + \Omega^2} \quad (3.73)$$

and the Hall conductivity

$$\sigma_H = \frac{ne}{B} \frac{\nu^2}{\nu^2 + \Omega^2}. \quad (3.74)$$

These findings are in agreement with similar derivations of the Hall and Pedersen conductivity (e.g. Baumjohann and Treumann (2012)). The Hall conductivity increases with collision frequency and asymptotically reaches  $\Sigma_{H,max} = ne/B$  for  $\nu \ll \Omega$ . In that

limit, the ions are practically at rest and the electrons move due to the  $\mathbf{E} \times \mathbf{B}$  drift unhindered. However, neither the electrons nor the ions have a net movement parallel to the electric field, which results in vanishing Pedersen conductivity in that case. Since the currents due to collisions need to be included in the simulations that are carried out in the single fluid MHD, we need to confirm that the conductivities arising from the collision terms are the same as the ones derived in the single particle case and reflect the physics well. For this purpose we use the velocity equation with collision terms (3.60). In the case of atmospheric neutral particles, we assume that there is a force balance between the Lorentz force and the collision term (e.g. Chané et al. (2013); Blöcker et al. (2016)) and neglect the other terms:

$$\mathbf{j} \times \mathbf{B} = \rho \nu \mathbf{v}. \quad (3.75)$$

Together with the Ohm's law for the electric field with the Hall term

$$\mathbf{E} = \left( -\mathbf{v} + \frac{\mathbf{j}}{ne} \right) \times \mathbf{B}, \quad (3.76)$$

replacing the velocity term with the help of Equation (3.75), we obtain an equation for the current density

$$-\frac{m\nu}{e} \mathbf{j} \times \mathbf{B} + (\mathbf{j} \times \mathbf{B}) \times \mathbf{B} + \rho \nu \mathbf{E} = 0. \quad (3.77)$$

This leads to the equation of the current density

$$\mathbf{j} = \frac{ne}{B} \left( \frac{\nu \Omega}{\nu^2 + \Omega^2} \mathbf{E} - \frac{\nu^2}{\nu^2 + \Omega^2} \frac{\mathbf{E} \times \mathbf{B}}{B} \right), \quad (3.78)$$

with  $\Omega = eB/m$ . This is exactly the same current density as in the equation derived with the drift motion. Thus, the collision term in the velocity equation comprises the same physics under the stated assumption of force balance. Note that in MHD without Hall term, the mass of a particle is not defined, but only the mass density  $\rho = mn$ . This can be used to regulate the strength of the Hall effect in simulations by changing the particle mass  $m$  while leaving the mass density  $\rho$  constant. Pedersen currents are present even without including the Hall term in the induction equation. Howeverm the Pedersen conductivity changes to the limiting case for  $m \rightarrow 0$ :

$$\sigma_P = \frac{\nu \rho}{B^2}. \quad (3.79)$$

As stated before, the collision frequency  $\nu$  can be regarded as an effective frequency at which a particle loses its entire momentum due to collisions. One could also regard it as the reciprocal of the characteristic time scale of the plasma's deceleration due to collisions in the reference frame of the moving plasma

$$\mathbf{v}(t) = \mathbf{v}_0 e^{-\nu t} \quad (3.80)$$

Here, we considered  $\nu$  as a constant. It is important to understand the underlying physics of the collision frequency. If we assume a plasma particle to transfer its entire momentum to the neutral during the collision process, we can calculate  $\nu$  using an effective cross section  $\sigma_C$  for the collision and computing the mean free path of a particle  $L = 1/(n_n \sigma_C)$ ,

with  $n_n$  the number density of the neutrals. The collision frequency of particle with velocity  $v$  is therefore  $\nu = v/L$  and thus

$$\nu = n_n v \sigma_C. \quad (3.81)$$

If the effective cross section is constant, the collision frequency would depend on the velocity. In this thesis, the relative velocity between ions and neutrals are considered low enough, that the effective cross section is determined by the induced dipole polarization and not by charge exchange, which becomes an important factor at higher velocities (Saur et al., 1999). In that limit, the momentum transfer between ions and neutrals depends on the time the particles are in close range to each other. Since the number of collision increases linearly with the velocity, but the time and therefore effective cross section is proportional to  $1/v$ , the product of velocity and effective cross section remains unchanged. Saur et al. (1999) state the cross section of  $\text{SO}_2$  due to induced dipole polarization

$$\sigma_C(v) = 2.21\pi \sqrt{\left(\frac{\alpha e^2}{32m_i v^2}\right)} \quad (3.82)$$

with the polarizability  $\alpha = 4.28 \cdot 10^{-20} \text{ m}^2$ . With that, we can calculate the product of cross section and velocity for an ion with an average mass of 22 amu:

$$v\sigma_C \approx 2 \cdot 10^{-16} \frac{\text{m}^3}{\text{s}}. \quad (3.83)$$



---

The Alfvén Wing Model

---

When a plasma flow with bulk speed  $v_0$  is perturbed by an obstacle at speeds below the Alfvén velocity  $v_A$ , i.e. the alfvénic Mach number  $M_A = v_0/v_A$  is below 1, Alfvén waves can travel upstream and no bow shock can form. This sub-alfvénic interaction was first discussed by Drell et al. (1965) for a linear interaction. Later, this model was extended by Neubauer (1980) for the fully non-linear case. Here, this model will be explained. First, the geometry and model assumptions are stated. In a second step the governing equations are presented. Afterwards, the currents and fields inside and outside of the Alfvén wing are derived and the physical implications are explained. To round up the understanding of Alfvén wings, we created a numerical model of the system using the presented equations. In the last part, this model is used to get a better understanding of the interaction of counter propagating Alfvén wings, e.g. in the case of non-linear reflections.

### 4.1. General Idea of the Alfvén Wing Model and Geometry

Neubauer (1980) presented an analytical model of the Alfvén wings that are generated when plasma moves relative to a conducting obstacle, in our case Io. At Io, the plasma moves almost perpendicular to the background magnetic field so we can assume simplified geometry of the interaction. A sketch of the interaction is shown in Figure 4.1. The plasma is flowing in positive x direction with sub-alfvénic relative speed  $\mathbf{v}_0$  to Io while the background magnetic field  $\mathbf{B}_0$  is homogeneous in negative z direction. The y coordinate completes the right-hand cartesian coordinate system and points roughly towards Jupiter. In this model, we consider the distance to the perturbing object to be sufficiently large that we can neglect disturbance of fast MHD waves. If we also make the assumption  $\beta < 1$ , i.e. the magnetic field pressure exceeds the thermal pressure, the characteristic of the slow mode differs from the characteristic of the Alfvén mode and we can restrict the analysis of a purely alfvénic interaction. Therefore, we can assume the density  $\rho$ , the pressure  $p$ , the magnitude  $B_0$  of the magnetic field and the Alfvén characteristics

$$\mathbf{c}^{\pm} = \mathbf{v} \pm \frac{\mathbf{B}}{\sqrt{\mu_0 \rho}} = \mathbf{v}_0 \pm \frac{\mathbf{B}_0}{\sqrt{\mu_0 \rho}} \quad (4.1)$$

to be constant. Equation (4.1) is a direct result of ideal MHD in incompressible plasma, which is well fulfilled in the case of Alfvén waves. This correlates the plasma velocity  $\mathbf{v}$  directly with the magnetic field strength  $\mathbf{B}$ .

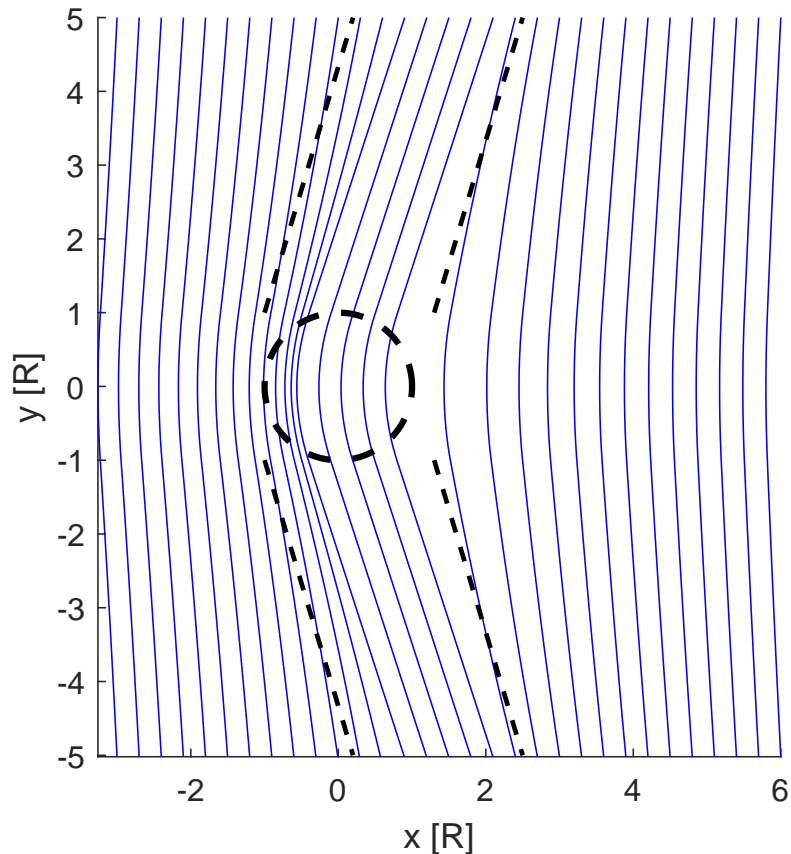


**Figure 4.1.:** Sketch of the Alfvén wing. The dashed straight lines show the outlines of the Alfvén wing parallel to its characteristics  $\mathbf{c}^{\pm}$ . The blue lines indicate the magnetic field perturbed by the Alfvén waves. Here the alfvénic Mach number  $MA = 0.3$  is chosen. Inside the wing, the magnetic field is tilted towards the characteristic, depending on interaction strength. In front of the obstacle (dashed circle) the magnetic field lines pile up.

## 4.2. Current System Inside the Alfvén Wing

Here, we focus on the positive Alfvén wing ( $\mathbf{c}^+$ ), where the waves propagate parallel to the background field. The equations derived from the negative Alfvén wing are analogous. Io’s Alfvén wings can be regarded as current tubes, where currents travel towards Io at the Jupiter facing side, continue through Io and its ionosphere and travel towards Jupiter at the anti-jovian side. To calculate the current, we use the ideal MHD induction equation, Ampère’s law disregarding displacement currents and equation (4.1).

$$\begin{aligned}
\nabla \cdot \mathbf{E} &= \nabla \cdot (\mathbf{B} \times \mathbf{v}) \\
&= -\mathbf{B} \cdot \nabla \times \mathbf{v} - \mathbf{v} \cdot \nabla \times \mathbf{B} \\
&= -\mathbf{B} \cdot \nabla \times \left( \mathbf{e}^* - \frac{\mathbf{B}}{\sqrt{\mu_0 \rho}} \right) + \left( \mathbf{c}^+ - \frac{\mathbf{B}}{\sqrt{\mu_0 \rho}} \right) \cdot \nabla \times \mathbf{B} \\
&= \mathbf{c}^+ \cdot \nabla \times \mathbf{B} \\
&= \mu_0 \mathbf{c}^+ \cdot \mathbf{j}
\end{aligned} \tag{4.2}$$

This shows, that the current  $j_{\parallel}$  along the characteristic  $\mathbf{c}^+$  can be written as

$$j_{\parallel} = \Sigma_A \nabla \cdot \mathbf{E} \tag{4.3}$$

with the Alfvén conductance

$$\Sigma_A = \frac{1}{\mu_0 v_A \sqrt{1 + M_A^2}}. \tag{4.4}$$

The current can be closed by reflections of the Alfvén waves at Alfvén velocity gradients, e.g. at the Jovian ionosphere or the torus boundary. Current perpendicular to the characteristic flows along the border of the Alfvén flux tube. In the absence of reflection or absorption, this current is divergence free on its own and does therefore not contribute to the current closure of the parallel currents. The magnetic field vortices corresponding to the parallel currents are shown in the simplified numerical simulations of the Alfvén wing in chapter 4.4.

### 4.3. Field Equations Inside the Alfvén Wing

In a strongly magnetized plasma, the conductivity parallel to the magnetic field lines is much higher than the perpendicular conductivity. Therefore, the perpendicular electric field is much larger than the parallel electric field. This fact has been used by Neubauer (1998) to derive a partial differential equation for the electric potential  $\Phi$  in the plane perpendicular to the magnetic field. In this derivation the current parallel to the magnetic field lines is closed by the perpendicular Pedersen and Hall currents, yielding  $\nabla \cdot \mathbf{j} = 0$ . Adding up all the contributions of the current  $\mathbf{j} = \underline{\underline{\sigma}} \mathbf{E}$  and integrating along the background magnetic field, i.e. the z-direction, we get

$$(\Sigma_P + \Sigma_A) \Delta \Phi + \left( \frac{\partial \Sigma_P}{\partial x} - \frac{\partial \Sigma_H}{\partial y} \right) \frac{\partial \Phi}{\partial x} + \left( \frac{\partial \Sigma_P}{\partial y} + \frac{\partial \Sigma_H}{\partial x} \right) \frac{\partial \Phi}{\partial y} = 0, \tag{4.5}$$

where y points in the direction of the background electric field  $\mathbf{E}_0 = E_0 \mathbf{e}_y = -\mathbf{v}_0 \times \mathbf{B}_0$  and

$$\Sigma_{P,H} = \int \sigma_{p,h} dz \tag{4.6}$$

are the Pedersen and Hall conductances, integrated along the field lines. This has been solved analytically for some simplified radially symmetric Pedersen conductances ignoring the Hall conductance Simon et al. (2021). However, to get a better understanding of the fields inside the Alfvén wing in the presence of non-negligible Hall conductance, we can look at the electric potential of a constant Pedersen  $\Sigma_P$  and Hall  $\Sigma_H$  conductance inside

the radius  $r < R$  and no conductance perpendicular to the background magnetic field outside. Saur et al. (1999) used equation (4.5) in polar coordinates

$$\begin{aligned} \frac{1}{r} \frac{\partial}{\partial \varphi} \left( (\Sigma_P + \Sigma_A) \frac{\partial \Phi}{\partial \varphi} \right) + \frac{\partial}{\partial r} \left( r (\Sigma_P + \Sigma_A) \frac{\partial \Phi}{\partial r} \right) \\ + \frac{\partial \Sigma_H}{\partial r} \frac{\partial \Phi}{\partial \varphi} - \frac{\partial \Sigma_H}{\partial \varphi} \frac{\partial \Phi}{\partial r} = 0, \end{aligned} \quad (4.7)$$

which simplifies to

$$\frac{1}{r} \frac{\partial^2 \Phi}{\partial \varphi^2} + \frac{\partial}{\partial r} \left( r \frac{\partial \Phi}{\partial r} \right) = 0 \quad (4.8)$$

and used continuity of the Potential  $\Phi$  at  $r = R$ , the boundary condition that the electric field needs to be uniformly in  $y$  direction at infinity and the jump condition

$$\lim_{\varepsilon \rightarrow 0} \left[ r (\Sigma_P + \Sigma_A) \frac{\partial \Phi}{\partial r} + \Sigma_H \frac{\partial \Phi}{\partial \phi} \right]_{R-\varepsilon}^{R+\varepsilon} = 0 \quad (4.9)$$

to derive the electric Potential and field inside and outside of the Alfvén wing. Note that for  $r > R$ , the Pedersen and Hall conductance vanishes in the jump condition, but the Alfvén conductance is constant for the whole interaction. A derivation of the jump condition can be found in appendix B.2. The resulting perpendicular electric field perturbation inside the Alfvén wing has a magnitude given by

$$\delta E = E_0 \sqrt{\frac{\Sigma_P^2 + \Sigma_H^2}{\Sigma_H^2 + (\Sigma_P + 2\Sigma_A)^2}} \quad (4.10)$$

and its direction is tilted against the  $y$  direction with the angle

$$\vartheta_p = \arctan \left( \frac{2\Sigma_H \Sigma_A}{\Sigma_H^2 + \Sigma_P (\Sigma_P + 2\Sigma_A)} \right). \quad (4.11)$$

The interior electric field is thus

$$\mathbf{E}^i = \mathbf{E}_0 - \delta E (\cos(\vartheta_p) \mathbf{e}_x + \sin(\vartheta_p) \mathbf{e}_y) \quad (4.12)$$

The external, i.e.  $r > R$ , electric field is derived similarly and can be expressed as

$$E_x^e = -\delta E \left( \frac{R}{r} \right)^2 \left( \sin(\vartheta_P) - 2 \frac{\sin(\vartheta_P) x^2 + \cos(\vartheta_P) xy}{r^2} \right) \quad (4.13)$$

$$E_y^e = E_0 - \delta E \left( \frac{R}{r} \right)^2 \left( \cos(\vartheta_P) - 2 \frac{\sin(\vartheta_P) xy + \cos(\vartheta_P) y^2}{r^2} \right). \quad (4.14)$$

With ideal MHD  $\mathbf{E} = -\mathbf{v} \times \mathbf{B}$  and constant characteristic  $\mathbf{c}^+$ , the magnetic field  $\mathbf{B}_\perp$  perpendicular to the Alfvén characteristic can be calculated. The short derivation is shown in appendix B.1.

$$\mathbf{B}_\perp = \mu_0 \Sigma_A \mathbf{e}_\parallel \times \mathbf{E} \quad (4.15)$$

Since  $|\mathbf{B}|$  is constant, the magnetic field parallel to the characteristic can therefore easily be calculated as

$$B_{\parallel} = \pm \sqrt{B_0^2 - B_{\perp}^2} \quad (4.16)$$

Note, that parallel ( $\parallel$ ) and perpendicular ( $\perp$ ) here are in the reference frame with respect to the Alfvén wing, which is tilted to the background magnetic field in z direction with the Alfvén angle

$$\tan(\vartheta_A) = M_A. \quad (4.17)$$

These analytical derivations show us some important features of the Alfvén wing. Since the characteristic in one direction does not change as it is described by equation (4.1), we see that a change in magnetic field  $\delta\mathbf{B}$  is always connected to a change in velocity  $\delta\mathbf{v}$ .

$$\delta\mathbf{v} = \mp \frac{\delta\mathbf{B}}{\sqrt{\mu_0\rho}} \quad (4.18)$$

In the Alfvén wing corresponding to the waves propagating along the magnetic field line, i.e. the southern wing in the case of Io, the change in velocity is anti-correlated with the change in magnetic field. In the Alfvén wing with anti-parallel propagating waves, i.e. the northern wing, the change in velocity is in the same direction as the change in magnetic field. Not only the velocity perpendicular to the characteristic, or to the background magnetic field for that matter, is altered, but there is also a velocity component parallel to the characteristic, or background magnetic field, as shown by equations (4.16) and (4.18).

The electric field inside the wing is perturbed by the change in magnetic field and plasma flow velocity. The amplitude of the perturbation in electric field is described by equation (4.10). In the absence of Hall conductivity, the change in electric field is opposite to the background magnetic field and scales with

$$\bar{\alpha} = \frac{\delta E}{E_0} = \frac{\Sigma_P}{\Sigma_P + 2\Sigma_A}, \quad (4.19)$$

which is often referred to as interaction strength (Saur et al. (2013), Southwood et al. (1980)). Since the change in parallel magnetic field is often relatively small in the case of a low alfvénic Mach number  $M_A$ , the relative velocity perturbation is of similar value as the electric field perturbation.

$$\frac{\delta v}{v_0} \approx \bar{\alpha} = \frac{\Sigma_P}{\Sigma_P + 2\Sigma_A} \quad (4.20)$$

Without reflections and Hall conductance, the velocity perturbation inside the Alfvén wing perpendicular to the background magnetic field is opposite to the incoming plasma flow. This can be seen from the equations regarding the electric field perturbation in the case of ideal MHD, where  $\mathbf{E} = -\mathbf{v} \times \mathbf{B}$  holds. This is a direct consequence of the deceleration of the particles by the obstacle. The deceleration travels as Alfvén waves along the characteristic and is therefore opposite to the incoming plasma flow. However, since Alfvén waves do not compress plasma or increase magnetic pressure, the flow around the obstacle and the Alfvén wing is accelerated.

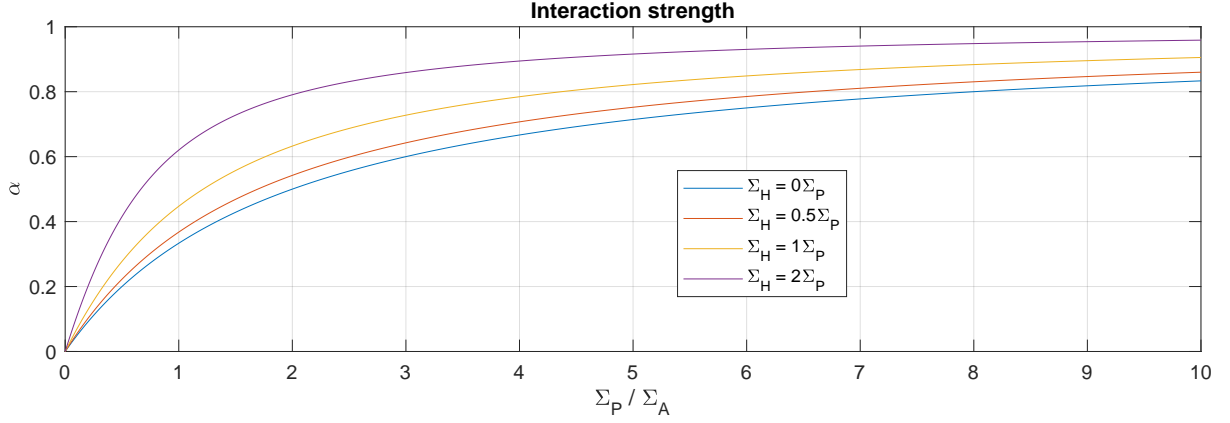


**Figure 4.2.:** Relative strengths of the perturbed electric field inside the Alfvén wing for different ratios of Hall and Pedersen conductances according to equation (4.10).

If Hall conductance is present, the electric field inside the Alfvén wing is twisted by an angle  $\vartheta_{twist}$  Saur et al. (1999)

$$\vartheta_{twist} = -\frac{E_x}{E_y} = \frac{\Sigma_H}{\Sigma_P + 2\Sigma_A} \quad (4.21)$$

Therefore also the magnetic field and velocity flow perturbation is twisted inside the Alfvén wing and the symmetry along the  $y$ -axis is broken. This can play an important role especially regarding non-linear reflections, where this asymmetry is self-reinforcing. This is discussed in more detail in chapter 4.5. Furthermore, the Hall effect increases the overall strength of the perturbation as shown in Figure 4.2.

### 4.3.1. Energy Transport

Alfvén waves carry electromagnetic energy in form of the Poynting flux  $\mathbf{S}$ , which is defined as

$$\mathbf{S} = \frac{\mathbf{E} \times \mathbf{B}}{\mu_0}. \quad (4.22)$$

The Poynting flux in an ideal MHD plasma moving perpendicular to the background magnetic field is non-negligible and has a value of  $\mathbf{S}_0 = -(\mathbf{v}_0 \times \mathbf{B}_0) \times \mathbf{B}_0 / \mu_0 = v_0 B_0^2 / \mu_0 \mathbf{e}_x$ . Also in the rest frame of the obstacle, the electric field perturbation outside the Alfvén wing decreases roughly with  $r^{-2}$  as can be seen by equations (4.13) and (4.14) and therefore the total Poynting flux integrated over the plane perpendicular to the propagation direction of the Alfvén wave is infinite. Additionally, we are interested in the energy flux towards Jupiter in the rest frame of Jupiter. Therefore, in this work Poynting flux is always calculated in the rest frame of the unperturbed plasma, as proposed by Saur et al. (2013). Since the perturbation of the magnetic field  $\delta\mathbf{B}$  and the electric field  $\delta\mathbf{E}$  is correlated by equation (4.18) and  $\mathbf{E} = -\mathbf{v} \times \mathbf{B}$ , the Poynting flux  $\mathbf{S}_z$  along the propagation direction, i.e. parallel or anti-parallel to the background magnetic field, can be written as

$$S_z = \pm B_0 \sqrt{\frac{\rho}{\mu_0}} \delta v_{\perp}^2 = \pm v_A \frac{\delta B_{\perp}^2}{\mu_0} \quad (4.23)$$

with  $v_A = \frac{B_0}{\sqrt{\mu_0 \rho}}$ . A full derivation is shown in appendix B.4. The Poynting flux along the propagation direction of the Alfvén waves can therefore be seen as the propagation of magnetic energy  $\delta B_{\perp}^2/2\mu_0$  with the Alfvén velocity  $v_A$ . As discussed in chapter 3.2 about the change in direction of the magnetic field and the velocity perturbation at reflections, either the magnetic or the velocity changes sign which results in the Poynting flux also changing sign at every reflection. Therefore, the Poynting flux always has a component parallel to the propagation direction and never anti-parallel to it.

## 4.4. Semi-Analytical Model

The distribution of Pedersen and Hall conductance of moons is not necessarily constant but can be structured due to asymmetries in the ionosphere and also in general the integration of the conductivities along the magnetic field lines. Equation (4.7) has no general analytical solution. To solve it numerically for a azimuthally symmetric Pedersen and Hall conductance, the differential equation is subdivided in a system of similar differential equations with an equation for each ring of constant conductances with defined jump and continuity conditions between them, similarly applied by Blöcker et al. (2016). A full derivation of the numerical solver can be found in Appendix B.2. This simulation is helpful to understand the equations and statements of the former chapter more clearly and to illustrate the fields inside and outside the Alfvén wing. Starting with a constant Pedersen conductance as in the analytical case of Saur et al. (1999), but neglecting the Hall conductance we get the most simple case of an Alfvén wing. The results are shown in the appendix B.3 and compared to the analytical solutions to evaluate the numerical solutions. A more realistic model with a continuously changing Pedersen conductance is used to show how the plasma flow velocity and the magnetic field is perturbed around the Alfvén wing. In this model, we assume the Pedersen conductance of a radially symmetric gas cloud with a constant density that exponentially decreases outside the sphere of radius  $R = 1$ . The conductance is then calculated using equations (3.81), (3.73) and (4.6). The result is an Alfvén wing with nearly constant perturbations inside corresponding to an interaction strength of  $\bar{\alpha} \approx 0.8$  with a smooth transition region at the border of the wing. The values taken for the initial conditions are shown in Table 4.1.

In the following, slides through the plane perpendicular to the background magnetic field, i.e. the x-y-plane, are shown. The absolute velocity and stream lines of the velocity field in this plane are shown in Figure 4.3. White color corresponds to flow with unperturbed magnitude, while red regions show accelerated plasma and blue regions show decelerated plasma. The flow is decelerated at the center of the Alfvén wing, caused by the slowdown of the plasma by the obstacle. This deceleration decreases towards the border and fades out in front of the wing ( $x < -1$ ) and in the wake ( $x > 1$ ). At the flanks of the wing, the flow is accelerated, caused by the flow around the obstacle. The rapid change from decelerated to accelerated plasma are equivalent to vortices in the perturbation of the velocity field and therefore in the magnetic field. This can be seen in figure 4.4, where the Poynting flux along the unperturbed magnetic field and the magnetic field perpendicular to it is shown. The magnetic field vortices are located at the flanks of the Alfvén wing,

**Table 4.1.:** Parameters for the numerical calculations of the Alfvén wing

Parameter	Symbol	Value [unit]
Bulk velocity	$v_0$	57000 [m/s]
Background magnetic field	$B_0$	1720 [nT]
Interaction strength	$\bar{\alpha}$	0.8 / 0.9
Electric field strength	$E_0$	0.1 [V/m]
Alfvénic Mach number	$M_A$	0.3
Alfvén conductance	$\Sigma_A$	4 [S]
Maximum Pedersen conductance	$\Sigma_P$	30 [S]
Maximum Hall conductance	$\Sigma_H$	0 [S] / 30 [S]

where the Poynting flux is zero. This results in crescent-shaped current sheets towards ( $y \approx 1.5$ ) and away from ( $y \approx -1.5$ ) the obstacle as shown in Figure 4.5. The minimum in Poynting flux is caused by the minimum in perturbation of velocity and magnetic field at the flanks, where the direction of the perturbation changes sign.

As a next step, Hall conductance is included. This increases the interaction strength corresponding to Figure 4.2 to about  $\bar{\alpha} = 0.9$ . Apart from the Hall conductance, that has now the same value as the Pedersen conductance, the parameters remain unchanged. The Poynting flux with perpendicular magnetic field lines and velocity field is shown in Figure 4.6. The overall structure of the Alfvén wing is twisted and rotated clockwise. The minima in the Poynting flux are displaced mainly in x direction. The same holds for the current maxima as shown in Figure 4.7.

The exact shape of the Poynting flux is determined by the distribution of Pedersen and Hall conductance. However, already with radially symmetric conductances, we can see how the symmetry with respect to the x-axis is broken and a displacement of extrema in magnitude of current, velocity, magnetic field and Poynting flux is formed. The presence of non-negligible Hall conductance therefore seems a viable candidate to explain the observed alternating Alfvén spot street.

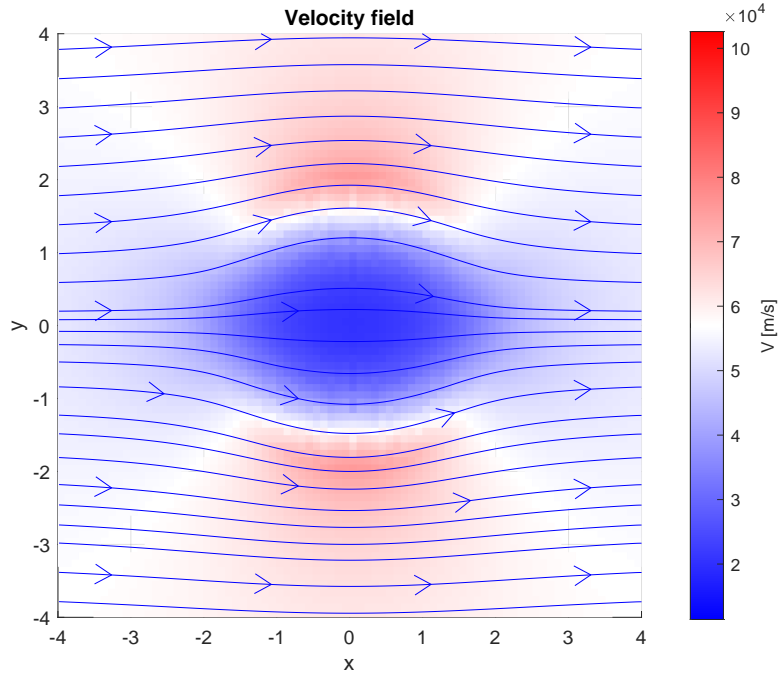


**Figure 4.3.:** Velocity Magnitude inside ( $r < 1$ ) and outside ( $r > 1$ ) of an Alfvén wing with radially symmetric exponentially decreasing Pedersen conductance and no Hall conductance. Red regions show accelerated plasma, while blue regions show decelerated plasma. The blue streamlines show the flow direction of the plasma inside the plane.

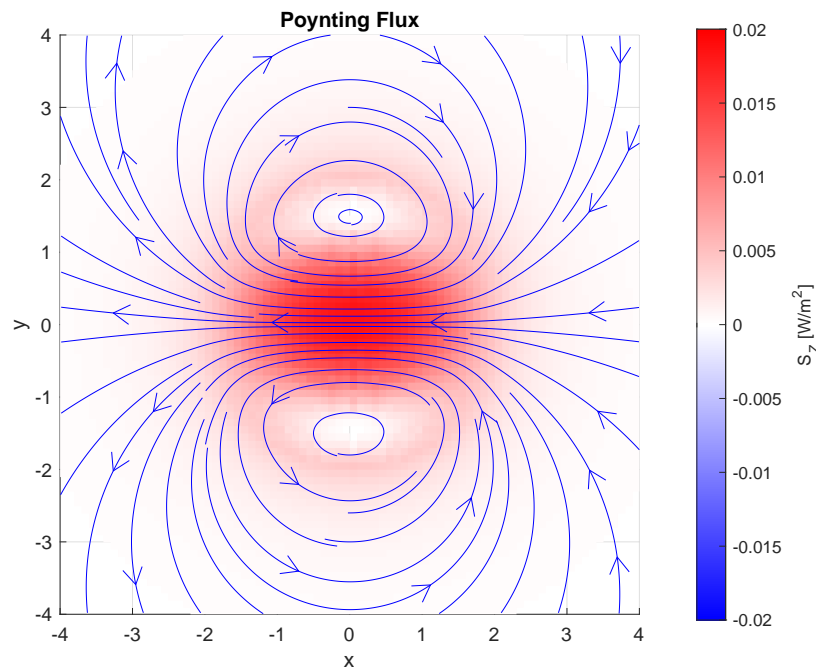


**Figure 4.4.:** Poynting flux inside ( $r < 1$ ) and outside ( $r > 1$ ) of an Alfvén wing with radially symmetric exponentially decreasing Pedersen conductance and no Hall conductance. The blue lines are the perpendicular magnetic field lines in the plane. They are anti-parallel (parallel in the case of the  $c^-$ -wing) to the flow direction (x-direction) inside the wing and along the flow direction outside. This results in vortices at the flanks of the wing, where the Poynting flux is zero.

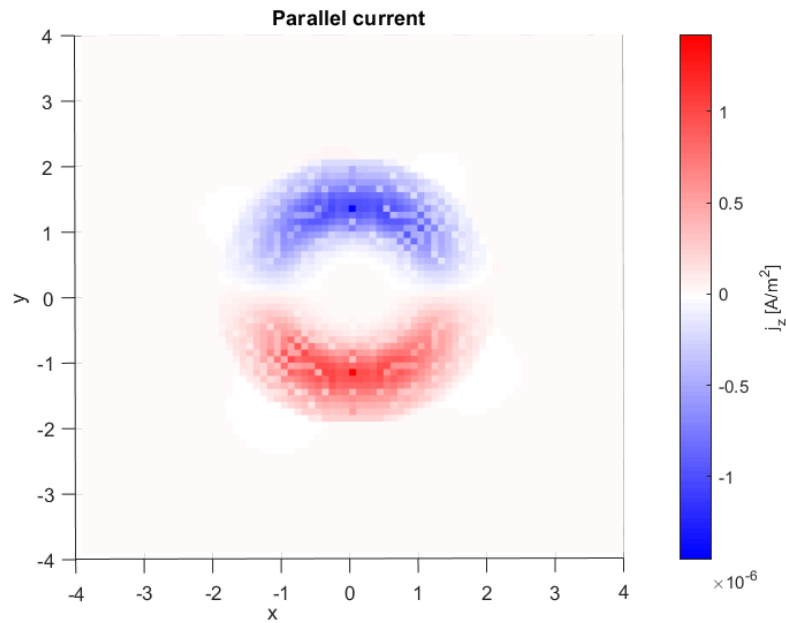


**Figure 4.5.:** Current towards (blue) and away from (red) the obstacle. The current is confined to the region of strongly changing perturbation, maximizing at the flanks of the Alfvén wing.

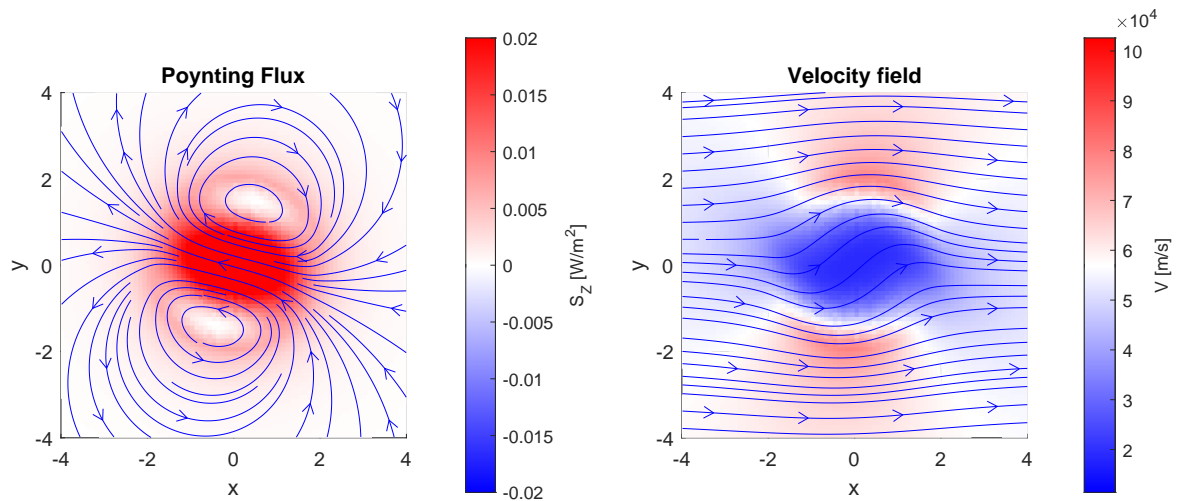


**Figure 4.6.:** Numeric simulations of the Alfvén wing with Hall conductance. The fields are tilted with respect to the horizontal  $x$  axis and the symmetry is broken. Left: Poynting flux along the unperturbed magnetic field and the magnetic field lines in the perpendicular plane. Right: Velocity magnitude and velocity stream lines in the plane. Regions with decreased plasma flow velocity are shown in blue, while accelerated plasma is shown in red.

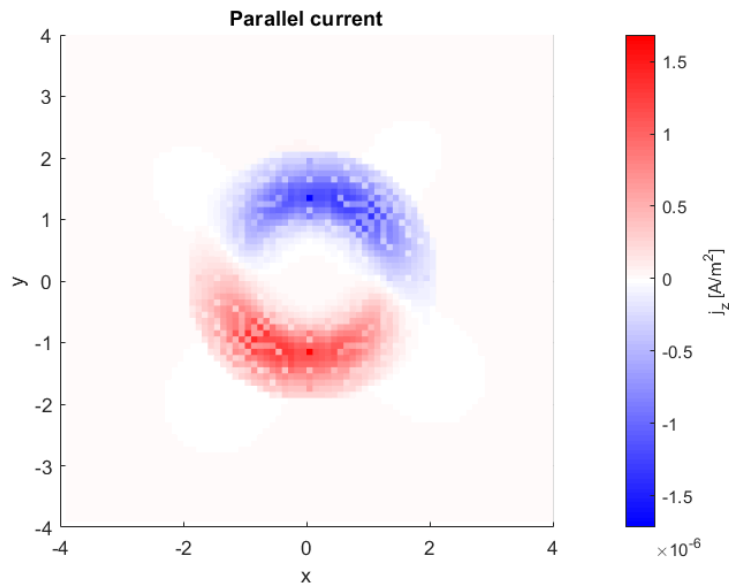


**Figure 4.7.:** Current towards (blue) and away from (red) the obstacle with Hall conductance. Compared to the simulation without Hall conductance, the current sheets a rotated clockwise.

## 4.5. Non-linear Reflections

An important feature of the Alfvén wing, especially in the case of Io, is the interaction of Alfvén waves with counter-propagating ones. In the linear case, the waves travel through each other without interacting. When the perturbation of the magnetic field is not-negligible compared to the background magnetic field, i.e. when  $\bar{\alpha}M_A \ll 1$ , the counter-propagating wave is affected by the perturbation of the incident wave. This results from the Alfvén wave carrying perturbations of magnetic field  $\delta\mathbf{B}$  and flow velocity  $\delta\mathbf{v}$ , which influence the velocity of the wave in both, direction and magnitude. For an Alfvén wave traveling in the same direction, these two effects would cancel out as seen by equation (4.1). However, a counter-propagating wave has the opposite characteristic, e.g.  $\mathbf{c}^-$  instead of  $\mathbf{c}^+$ . This results in a change of characteristic, so that the new characteristic of the counter propagating wave is

$$\mathbf{c}_{new}^{\mp} = \mathbf{c}^{\mp} \pm 2 \frac{\delta\mathbf{B}}{\sqrt{\mu_0\rho}}, \quad (4.24)$$

where  $\delta\mathbf{B}$  is the perturbation of the magnetic field by the incident wave. To get an insight about the shape of the field distribution of the reflected wave, we need to get a three dimensional model of the characteristics of the counter propagating wave. For that purpose, we take the perturbation  $\delta\mathbf{A}(x, y)$  of the Alfvén wing in the two dimensional plane  $(x, y)$  perpendicular to the background magnetic field as in chapter 4.4, with  $\delta\mathbf{A}$  being any alfvénic perturbation like velocity, electric field or magnetic field. Those perturbation are then mapped along their characteristics, which is in our case constant and given by the background magnetic field and bulk velocity  $\mathbf{c}^+ = \mathbf{v}_0 + \frac{\mathbf{B}_0}{\sqrt{\mu_0\rho}}$ , i.e.  $\delta\mathbf{A}(\mathbf{r}) = \delta\mathbf{A}(\mathbf{r} + \mathbf{c}^+ \delta t)$  for any travel time  $\delta t$ . This results in a three dimensional model of the incident Alfvén wing. With this perturbation model, we can calculate the characteristic of the counter-propagating

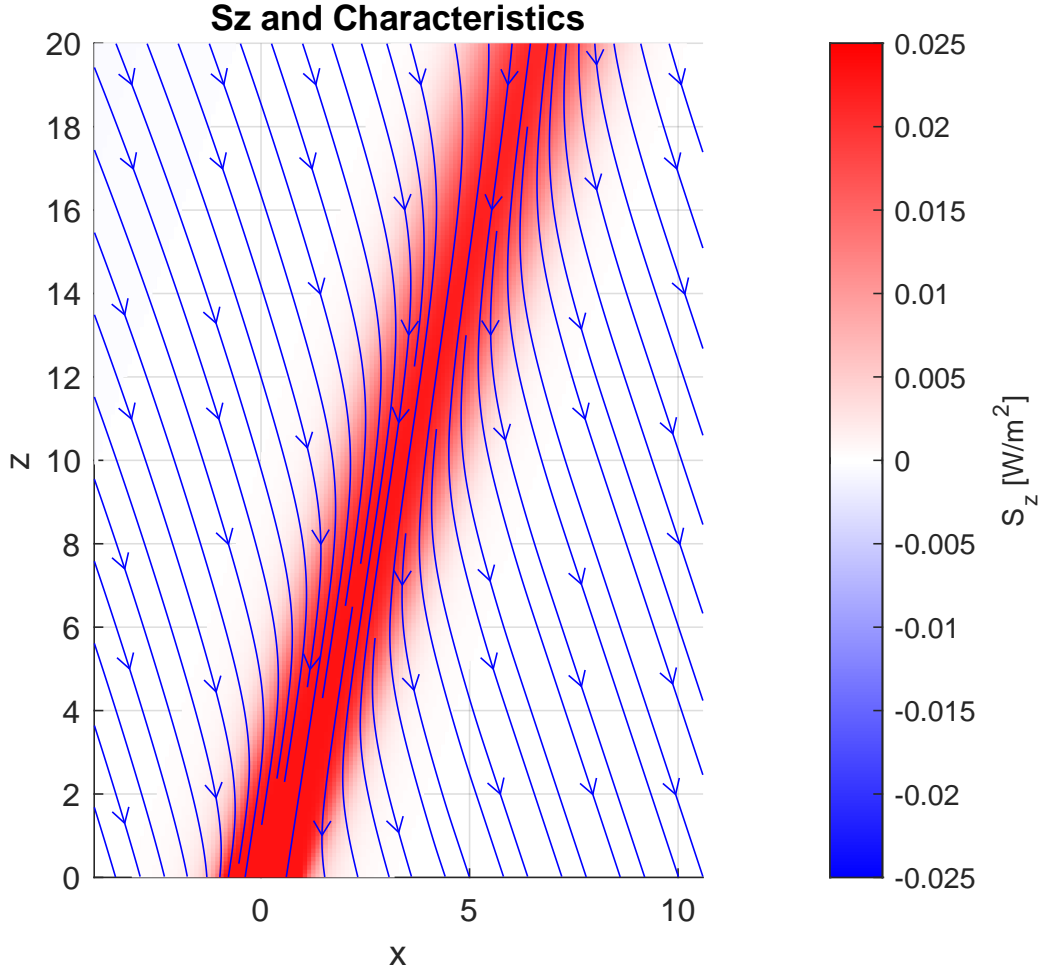


**Figure 4.8.:** The Poynting flux in the  $(x,z)$ -plane of the modelled Alfvén wing. The background magnetic field is along the  $z$ -axis and the bulk velocity is in  $x$  direction. The  $\mathbf{c}^-$  characteristic of a counter-propagating Alfvén wing are shown as blue lines. The  $\mathbf{c}^+$  characteristics are parallel to the Alfvén wing.

wave with equation (4.24). We now map a reflected  $\delta\mathbf{A}_{ref}(x,y) = \pm R\delta\mathbf{A}(x,y)$  along those newly calculated characteristics  $\mathbf{c}^-$  for the counter-propagating wave as shown in Figure 4.8. Depending on the reflection, either velocity or magnetic field changes sign and the amplitude depends on the reflection coefficient  $R$ . The mapping here is done with an explicit Runge-Kutta solver of fourth degree. For this purpose the characteristic is written as  $\mathbf{c}^- = c_x^- \mathbf{e}_x + c_y^- \mathbf{e}_y + c_z^- \mathbf{e}_z$ . Furthermore, the time steps in the explicit solvers are chosen, so that  $\delta t \cdot c_z^- = \Delta z = \text{const.}$ , yielding to a mapping onto equidistant  $z$ -layers.

$$\delta\mathbf{A}(x,y,z + \Delta z) = \delta\mathbf{A}(x - \delta t c_x^-, y - \delta t c_y^-, z) \cdot \sqrt{\frac{S_{new}}{S_{old}}} \quad (4.25)$$

This iteratively maps along the characteristic and also conserves total Poynting flux  $S_{total} = \int S_z dx dy$ . This is done by scaling the obtained perturbation  $\delta\mathbf{A}(x,y,z + \Delta z)$  with the square root of the relative change in area, because the Poynting flux is roughly proportional to the square of the perturbation as shown in equation (4.23). The change

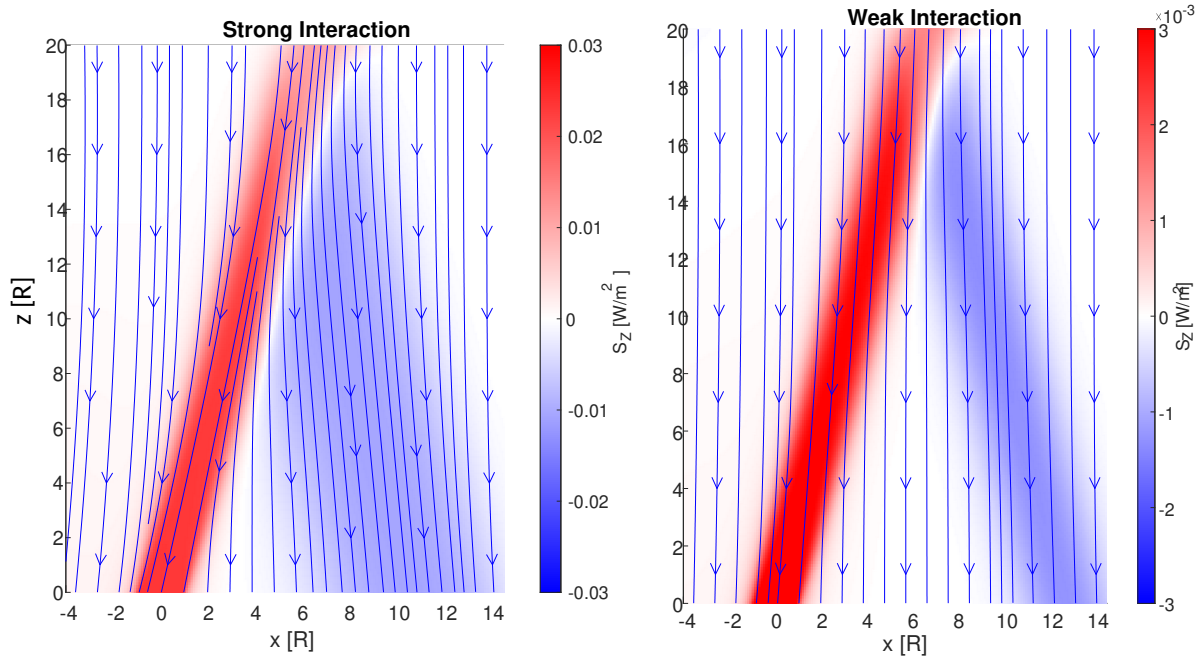


**Figure 4.9.:** Poynting Flux and magnetic field line for a strong interaction (left) with  $\Sigma_P/\Sigma_A = 8$  and weak interaction (right)  $\Sigma_P/\Sigma_A = 0.7$ . The maximum Poynting flux is one magnitude lower in the case of weak interaction and the magnetic field lines in the incident (red) and reflected (blue) Alfvén wing are only weakly perturbed. For the strong interaction, the reflected Alfvén wing is much broader due to the non-linear reflection.

in Alfvén speed is assumed to be negligible. The relative change in area is calculated numerically for each area grid cell of size  $\Delta x \Delta y$ , but can be approximated to first order by

$$\frac{S_{new}}{S_{old}} \approx 1 + \Delta z^2 \frac{\partial(c_x/c_z)}{\partial x} \frac{\partial(c_y/c_z)}{\partial y} \quad (4.26)$$

The incident Alfvén wing is gradually reflected at  $z = 20$  [R]. The resulting Poynting flux in the  $(x,z)$  plane is shown in Figure 4.9 for a high interaction strength and a low interaction strength. This difference is important, because the characteristic is fairly unchanged for the reflected wave in the case of a low interaction strength. Therefore, the incident and reflection angle are very similar and the reflected wing follows its characteristic resembling the incident wave in shape and size. In the case of strong interaction however, the plasma inside the incident wing is almost at halt. To keep the characteristic constant, this results in strongly tilting the magnetic field towards the characteristic. Therefore, the characteristic of the reflected wave is strongly perturbed by the incident wing and the wave is reflected back into the incident wing. This leads to a strong change in the shape and extend of the reflected wing. If the interaction strength is high enough, this could result in the reflected wave to be reflected back to the obstacle, which would result in a unipolar inductor as proposed by Goldreich and Lynden-Bell (1969). To see, how the reflection also changes the transmitted wing ( $z > 20$  [R]), we can now see how a new incident wing would propagate through the medium changed by the first incident and reflected wing. The reflection changes the new  $\mathbf{c}^+$  characteristic according to equation (4.24). The Poynting flux for the incident, transmitted and reflected wings is shown

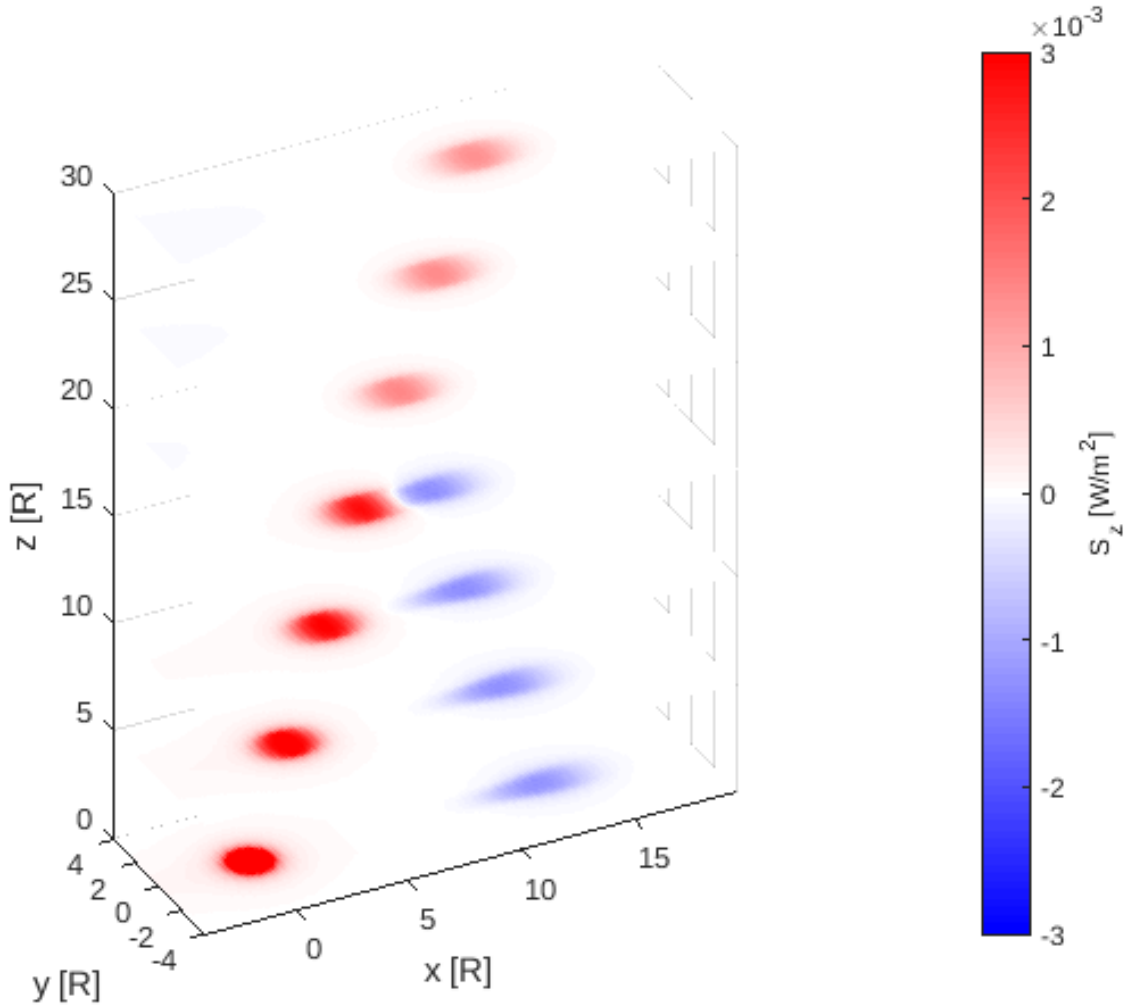


**Figure 4.10.:** Poynting Flux in for different distances  $z$  from the  $(x,y)$  plane in the case of weak interaction. The Poynting flux of the incident wing (red) is only reduced after the reflection, but the shape is unaltered. The reflected wing (blue) resembles the incident in shape apart from a slight stretching along the  $x$  direction.

for different offsets  $z$  in Figure 4.10 for weak interaction and in Figure 4.11 for strong interaction. In the case of weak interaction a linear reflection takes place.

This results in the incident, reflected and transmitted wing to be similar in shape albeit the reflected and transmitted each carry only a part of the energy carried by the incident wing. In the case of strong interaction however, the shape of reflected and transmitted wing is strongly deformed. The reflected wing, as shown in blue in Figure 4.11, is elongated as already discussed. Furthermore the upstream part of it is narrowed in  $y$  direction, perpendicular to the flow. This can be understood, if we look at the characteristic  $\mathbf{c}^-$  of the reflected wing in the plane  $z = \text{const.}$  perpendicular of the background magnetic field as shown in Figure 4.13. The deviation of the characteristic for the reflected wing  $\delta\mathbf{c}^- = \mathbf{c}^- - \mathbf{v}_0 + \mathbf{B}_0/\sqrt{\mu_0\rho}$  is shown as stream lines. Those are similar to the magnetic field perturbations shown in Figure 4.4 as described by equation (4.24). Without perturbation, the reflected Alfvén wing would continuously propagate along the unaltered characteristic  $\mathbf{c}^-$ , which would by itself place the reflected Alfvén at the blue dashed outline. However, on its way its deformed by the characteristic perturbation in the plane. These are pointing

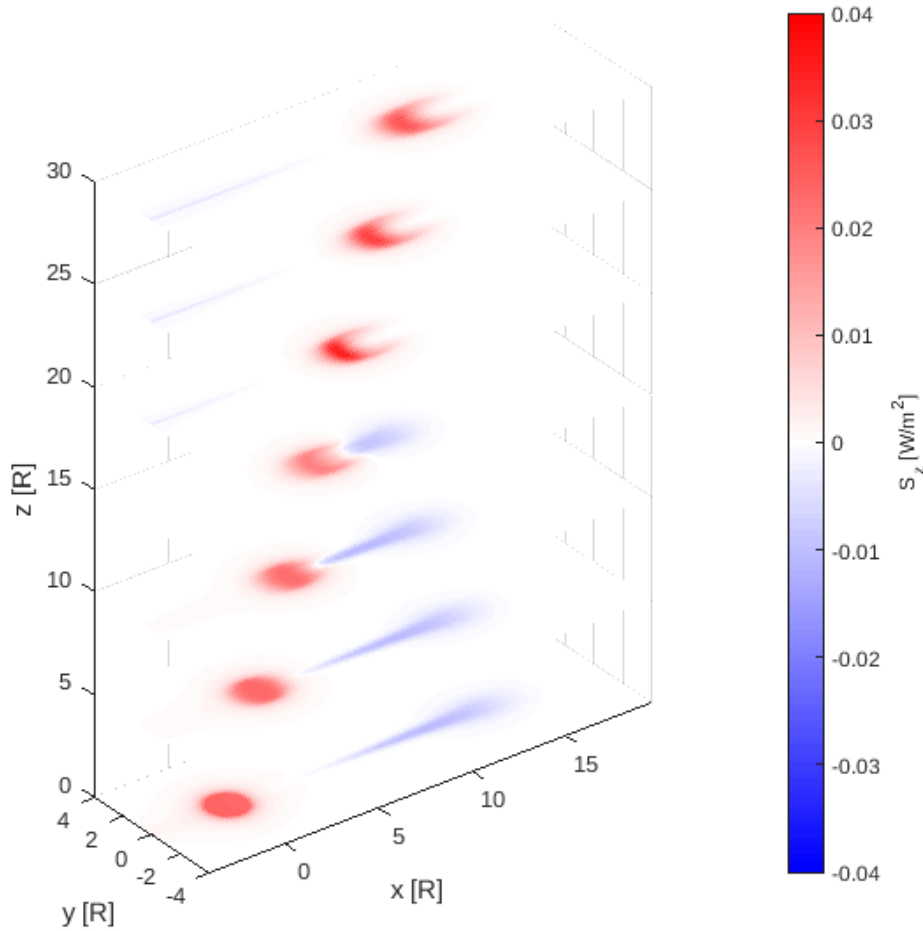


**Figure 4.11.:** Poynting Flux in for different distances  $z$  from the  $(x,y)$  plane in the case of strong interaction. The reflected wing (blue) is stretched and the upstream part closer to the incident wing is narrowed. The incident wing (red,  $z < 20$ ) changes shape when the reflected wing change its characteristics. This carves out the downstream part of the incident wing and gives the transmitted wing (red,  $z > 20$ ) its horseshoe shape.

in negative  $x$  direction, moving parts of the reflected wing towards the incident wing and stretching it. The characteristics are also pointing inwards, compressing the wing and therefore narrowed. Since the upstream part is more affected by the perturbation, which are stronger closer to the incident wing, this part is more stretched and narrowed.

To understand the horseshoe shape of the transmitted wing, we can similarly look, how the reflected wing changes the characteristics of the incident wing. This is shown in Figure 4.12. The Poynting flux of the incident and reflected wing are already deformed and do no longer fit the circular shape as outlined by the dashed circles. The perturbation of the characteristic  $\delta\mathbf{c}^+ = \mathbf{c}^+ - \mathbf{v}_0 - \mathbf{B}_0/\sqrt{\mu_0\rho}$  for the incident wing is shown in streamlines. These mainly point in  $-x$  direction, similar to the  $\delta\mathbf{c}^-$ . Since this effect is stronger downstream closer to the reflected wing, the incident Alfvén wing is compressed in  $x$  direction. Because this effect is stronger in the center and the characteristic also points slightly outwards, the incident Alfvén wing gets continuously carved out downstream and it gets shaped like a horseshoe.

These simplified numerical simulations give us a lot of insight about what to expect from different aspects of the interaction. First, the Hall effect has a strong symmetry breaking

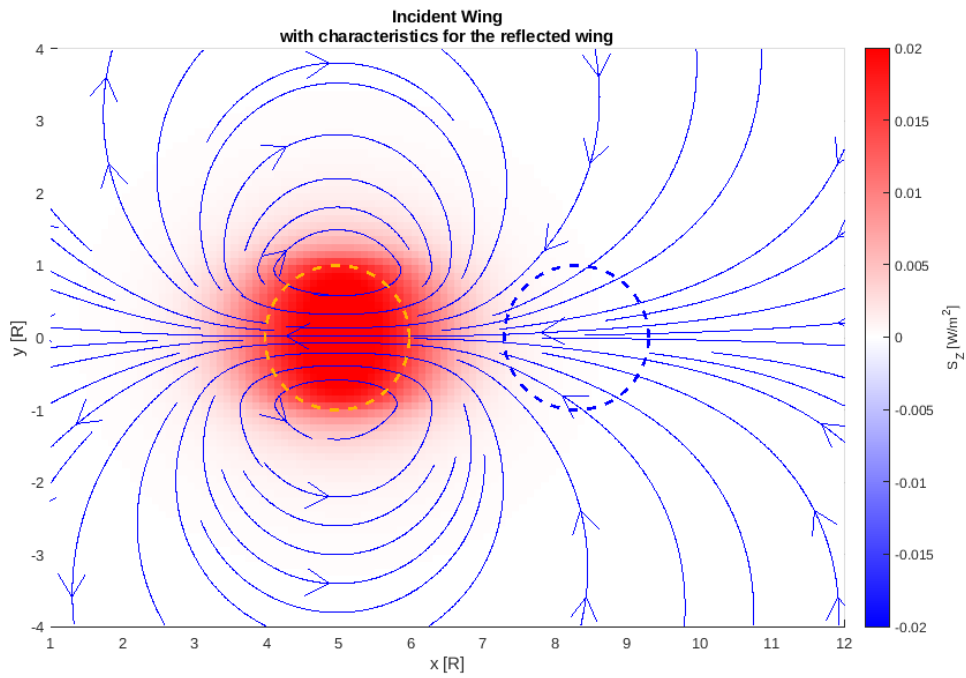


**Figure 4.12.:** Poynting flux in the  $z = 15$  R plane for the incident wing. The characteristic perturbation  $\delta c^-$  for the reflected wing is shown as field lines. The projected outlines of the incident (orange) and reflected (blue) Alfvén wings are shown as dashed circles.

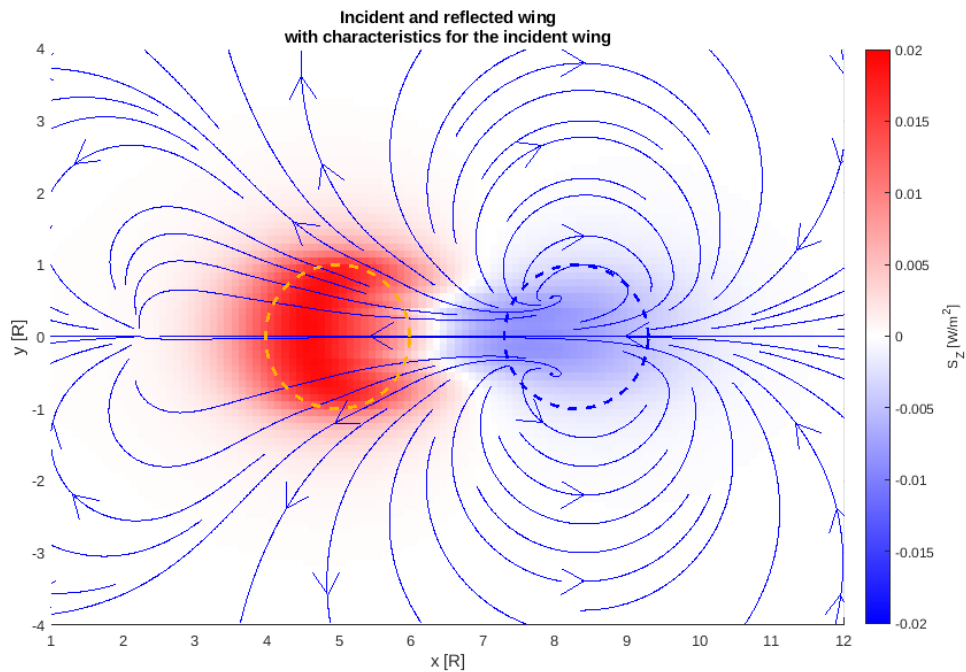


**Figure 4.13.:** Poynting flux in the  $z = 15$  R plane for the reflected wing. The characteristic perturbation  $\delta c^+$  for the incident wing is shown as field lines. The projected outlines of the incident (orange) and reflected (blue) Alfvén wings are shown as dashed circles.

---

and warping effect on the morphology of the Alfvén wing. The effect is stronger for higher ratios of Hall to Pedersen conductance. In the case of weak interaction, incident, reflected and transmitted Alfvén wing have similar shape and incident and reflection angle are similar. If the interaction grows stronger, we expect the reflected Alfvén wing to get closer to the incident wing and get stretched and narrowed. The opposite is true for the transmitted wing, that gets compressed and slightly widened. Since the compression and widening is not uniform but enhanced downstream near the reflected wing, the transmitted wing is shaped like a horseshoe. Therefore, we expect Hall conductances and non-linear reflections to have a major role in the morphology of the Poynting flux.



---

## Application of the Io Alfvén Wing Model

---

The general mechanism to produce the Galilean footprints is believed to be the propagation of Alfvén wings towards the Jovian ionosphere, where they accelerate particles via wave particle interaction. In the MHD limit, the propagation of the Alfvén wave packages depend only on the magnetic field  $\mathbf{B}$  and the mass density  $\rho$  along the path. In this chapter we will therefore discuss two questions: (1) Are the location and separation of the Io footprint and its tail spots consistent with established magnetic field and mass density models? (2) Can we use the footprint positions to constrain a model for the mass density? Here, we only are interested in the mass density model, since with the JRM09 model by Connerney et al. (2018) we already have an adequate magnetic field model for the inner Jovian magnetosphere.

### 5.1. JRM09 Magnetic Field Model

As discussed in Section 2.1, Jupiter’s magnetic field at Io’s vicinity can be regarded as a dipole of strength  $M = 4.177$  G and a tilt of  $\vartheta_D = 10.25^\circ$  colatitude in  $\varphi_D = 196.38^\circ$  western longitude. When getting close to the Jovian ionosphere, higher orders are needed to accurately describe the magnetic field lines governing the propagation direction of the Alfvén waves. We therefore use the JRM09 magnetic field model by Connerney et al. (2018). For that purpose, an MPI-parallelized C code was written to calculate the magnetic field at each position in the Jovian inner magnetosphere using the Gauss coefficients published in the supplementary material by Connerney et al. (2021). To validate the code, the magnetic field on the flattened surface of Jupiter was calculated as shown in Figure 5.1 and compared to the published values, which were identical.

The magnetic field itself is not enough to determine the position of the footprint when Io is at a specific location. However, it can be used to identify the entirety of possible footprint positions at both hemispheres by mapping the orbital position of Io along the magnetic field lines towards Jupiter’s surface as shown as black lines in Figure 5.1. The grey squares show the footprint of Io’s flux tube in  $5^\circ$  longitudinal separation in Io’s orbit. The northern footprints get closer to each other near the anomaly at  $200^\circ$  eastern longitude and are

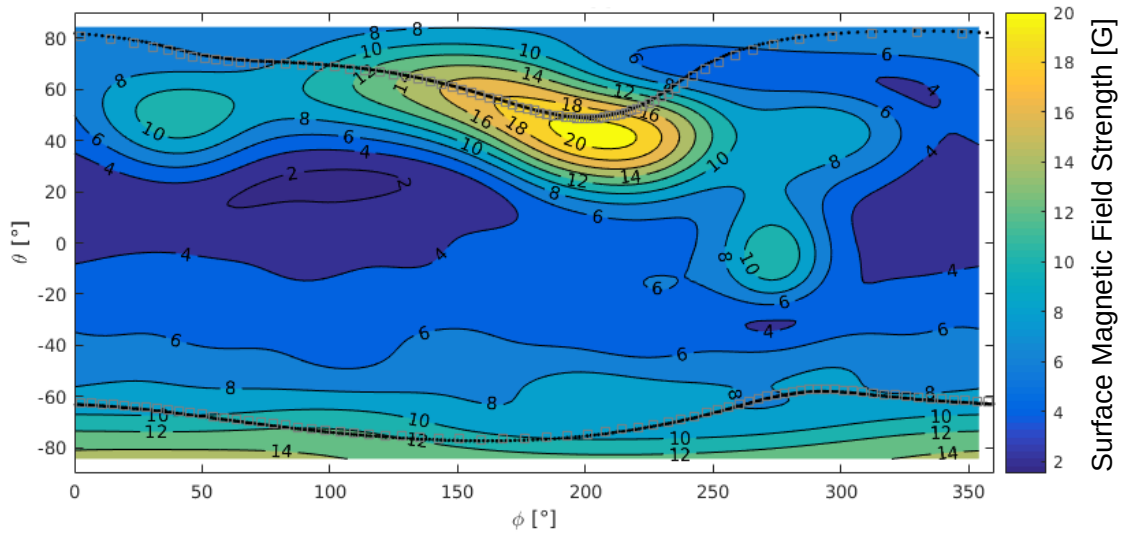


**Figure 5.1.:** Magnetic field strength on the flattened ( $f = 1/15.4$ ) surface of Jupiter, calculated with the JRM09 model as a function of eastern longitude and colatitude. The field lines mapping from the orbital position of Io at  $L = 5.9$  onto the Jovian surface are shown as black lines in both hemispheres. The grey squares depict the mapping of Io's orbital position in  $5^\circ$  separations in longitude.

stretched out near  $0^\circ$ , where they move to higher latitudes. The footprints are more evenly spaced at the southern hemisphere, where the magnetic field is better approximated by a dipole. Hinton et al. (2019) used the JRM09 model to calculate the positions of the footprints. They furthermore used a smooth torus model to calculate overall travel times, ranging from only slightly more than two minutes, when Io is near the close edge of the torus to about eleven minutes when Io is on the opposite side of the torus. They further found that the total round trip travel time for an Alfvén wave package, i.e. the travel time to one hemisphere then to the opposite hemisphere and back to Io, depends on the position of Io. It ranges from 25 minutes to 30 minutes in their model. The variability of this round-trip time should not depend on the density model and therefore solely results from the JRM09 magnetic field model (Hinton et al., 2019).

## 5.2. Torus Density Model

To calculate the position of the Io footprint relative to the position of Io itself, we need to account for the Alfvén wave travel times, which are not only dependent on the magnetic field strength but also on the plasma mass density  $\rho$  along the travel path. It is therefore necessary to consider an accurate torus density model. As a first approach, we can use the torus density model described by Phipps et al. (2020). The density distribution for this model is shown in Figure 5.2. The magnetic field line is mostly affected by the Io torus region referred to as ribbon. The torus itself is tilted against the magnetic equator plane.

With a density model, the travel times of alfvénic perturbation originating from Io towards Jupiter can be calculated. Therefore, we can determine the relative position of the longitude of Io  $\varphi_{Io}$  and the longitude  $\varphi_{IFP}$  of the corresponding footprint of the Io flux tube. This allows us to define a leading angle  $\Delta\varphi = \varphi_{Io} - \varphi_{IFP}$  for each position of

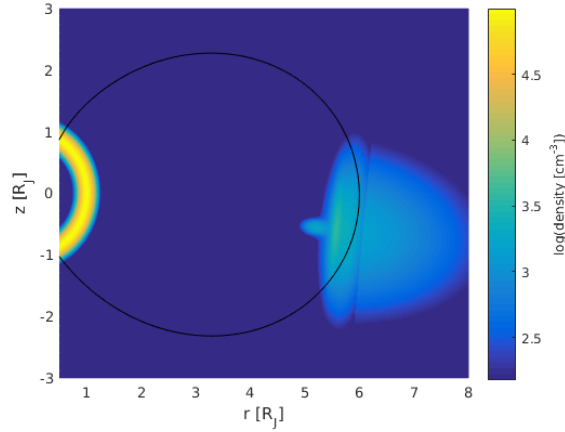


**Figure 5.2.:** Plasma number density distribution in the inner Jovian magnetosphere calculated with the empirical model given by Phipps et al. (2020). The  $z$ -axis is aligned with the JRM09 magnetic dipole. The magnetic field line (black) is mainly located within the ribbon region of the torus. The minimum density is set to  $n_{min} = 1 \text{ cm}^{-3}$  in the high latitude regions. Jupiter is characterized by a high density gradient in the ionosphere (left yellow circle) with a peak number density of  $n_{max} = 10^5 \text{ cm}^{-3}$ .

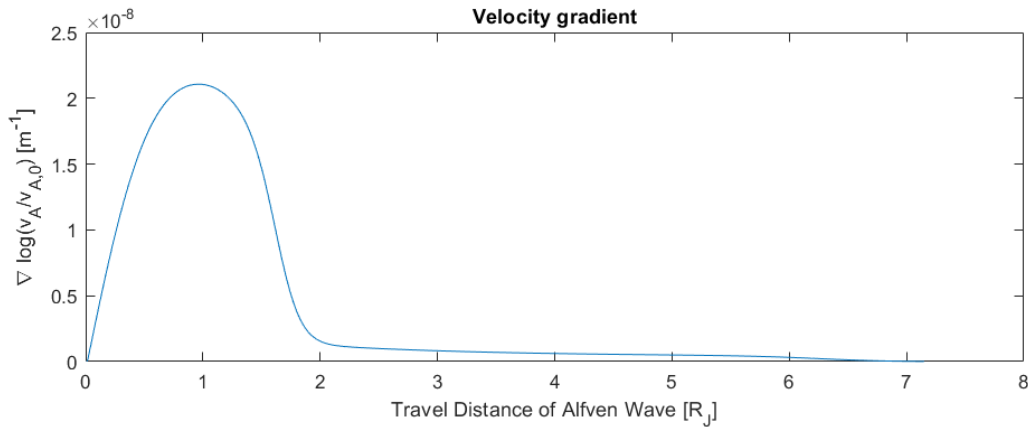


**Figure 5.3.:** The relative Alfvén phase velocity gradient along the Io flux tube starting at the torus center. Jupiter’s ionosphere is excluded in this plot. Here, the relativistic Alfvén velocity is used, which results in almost constant phase velocity close to the speed of light at higher latitudes after a travelled distance  $z$  along the flux tube of  $\approx 2R_J$ . The strongest relative phase velocity gradient is at  $z \approx 0.9R_J$ .

Io. The concept is shown in Figure 5.4. The Alfvén wings projected onto the surface of Jupiter are shown as red lines. They are reflected at the position of the highest relative phase velocity gradient  $\nabla(\log(v_A))$  along the magnetic field line, which is approximately  $0.9R_J$  from the torus center and corresponds to  $\theta = 8.4^\circ$  in latitude. The gradient of relative phase velocity along the Io flux tube starting from the torus center is shown in Figure 5.3.

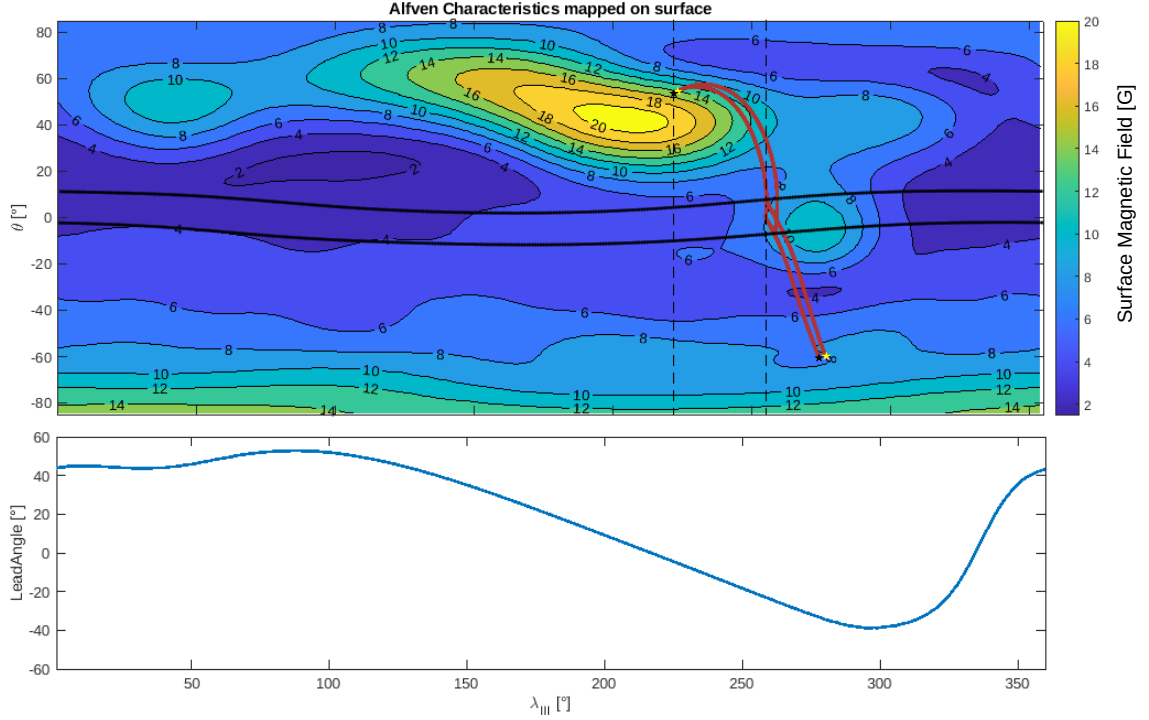


**Figure 5.4.:** Top: Surface magnetic field calculated with JRM09. The red lines indicate the projection of the northern and southern Alfvén wing on the surface, once reflected at both torus boundaries, represented as black lines. Therefore, four footprint positions are determined, two on both hemispheres indicated as black stars for the footprint of the main Alfvén wing and as yellow stars for the reflected Alfvén wing. The black dashed lines indicate the longitudinal positions of the northern main Alfvén wing footprint and Io. The difference between those longitude is called the leading angle. Bottom: The northern leading angle for the northern main Alfvén wing footprint.

### 5.3. Inversion of Footprint Position

In this section, we will address the second question posed at the beginning of this chapter. That is, whether it is possible to use the footprint positions to constrain a density model for the Io flux tube. Along the magnetic field lines, the density gradient of the torus region is mainly determined by the force balance between centrifugal force and thermal pressure. From these two forces, a scale height

$$H = \sqrt{\frac{2k_B T}{3\Omega_J^2 \langle m \rangle}}, \quad (5.1)$$

with  $k_B$  being the Boltzmann constant, can be approximated (Thomas et al., 2004; Phipps and Withers, 2017) and depends on Jupiter’s angular velocity  $\Omega_J$  and the average mass  $\langle m \rangle = 24$  amu. Therefore, the temperature can be inferred from the density distribution in the torus region. As mentioned before, the position of the footprints relative to Io’s position, i.e. the leading angle, depends on the density along the field line, in particular inside the torus. Therefore, observations of the location of the footprints can be used as data for an inversion of the density distribution along the Io flux tube. For that purpose, a force balance model is introduced similar to the one by Dougherty et al. (2017) to calculate the density along the flux tube given an ion temperature  $T_i$ .

$$k_B T_i \frac{\partial n}{\partial s} - n \langle m \rangle \Omega_J^2 \frac{1}{2} \frac{\partial r_{\perp}^2}{\partial s} + n \langle m \rangle G M_J \frac{\partial 1/r}{\partial s} = 0 \quad (5.2)$$

Here,  $n$  is the number density that depends on the position along the flux tube  $s$ . The second term is representing the centrifugal force and scales with the change in distance  $r_{\perp}$  to the rotation axis. This term is small near the centrifugal equator where the density is fairly constant. The last term stands for the gravitational force and is negligible near the torus, but is the driving contributor at the Jovian ionosphere. This force balance model has some simplifications. First, only one ion species with an average mass  $\langle m \rangle$  is assumed. Also the ion temperature is isotropic  $T_{i,\parallel} = T_{i,\perp}$  and constant in this model. Furthermore, the ambipolar electric field due to electrons is neglected. To account for the electrons, we can add the electron pressure in the first term and substitute the ion temperature  $T_i$  with the sum of the electron and ion temperature  $T^* = T_i + T_e$ . Since the electron mass is negligible, they don't have any influence on the other terms and we use quasi-neutrality and singly charged ions, therefore  $n = n_i = n_e$ . This results in a density model along the magnetic field line that depends on the density  $n_0 = n(z = 0)$  at the torus center and the temperature  $T^*$ . These two values span the modeling vector  $\mathbf{m} = (n_0, T^*)^T$  of the inversion. The data vector  $\mathbf{d} = (\Delta\varphi(\varphi_{Io}))_i$  are the observed leading angles, taken from the supplementary material of Bonfond et al. (2017). Those two values are connected by the forward operator  $\mathbf{F}(\rho(\mathbf{r}, n_0, T^*)) = \mathbf{F}(\varphi_{Io}, \mathbf{m})$ . It calculates the leading angle  $\Delta\varphi_0$  by mapping from Io's position  $\varphi_{Io}$  to Jupiter's flattened surface. Then the total leading angle  $\Delta\varphi = \Delta\varphi_0 + \Delta\varphi_t$  is computed by adding the angle

$$\Delta\varphi_t = \Omega_{J, syn} \int_{Io}^{Jupiter} \frac{ds}{v_A(B(\mathbf{r}), \rho(\mathbf{r}, n_0, T^*))} \quad (5.3)$$

to it, corresponding to the Alfvén travel time. Here, it is important to use the synodic period  $\Omega_{J, syn}$ , taking account of the movement of Io relative to Jupiter. The simple addition of the travel time dependent part  $\Delta\varphi_t$  to the leading angle  $\Delta\varphi_0$  for an instant development of an Alfvén wing along the Io flux tube is possible because the plasma is frozen into the magnetic field. Therefore, the Alfvén wave and corresponding Alfvén wing does not change the magnetic field line and  $\Delta\varphi_0$  does not by itself depend on the travel time. The cost function  $\Phi$  is the  $L_2$  norm between the model responses  $F_i(\varphi_{Io,i}, \mathbf{m})$  and the data vector  $d_i(\varphi_{Io,i})$  weighted by a matrix  $\mathbf{W} = \text{diag}(\epsilon_i)$  that incorporates the errors  $\epsilon_i$  of each observation  $d_i$ .

$$\Phi = (\mathbf{F} - \mathbf{d})\mathbf{W}^2(\mathbf{F} - \mathbf{d})^T \quad (5.4)$$

Since the model space is very small, i.e. only two parameters, the inversion algorithm to minimize the cost function  $\Phi$  was a simple hedgehog method that sweeps out the space of possible values via trial and error method. The cost function was calculated for 991 values for  $n_0$ , starting from  $50 \text{ cm}^{-3}$  in increments of  $5 \text{ cm}^{-3}$  to up to  $5000 \text{ cm}^{-3}$  and for 100 values of the combined temperature  $T^*$  starting from 2 K in 2 K intervals to up to 200 K. To characterize the result of the inversion an error weighted misfit

$$\chi = \sqrt{\frac{1}{N} \sum_i^N \frac{F_i - d_i}{\epsilon_i}} \quad (5.5)$$

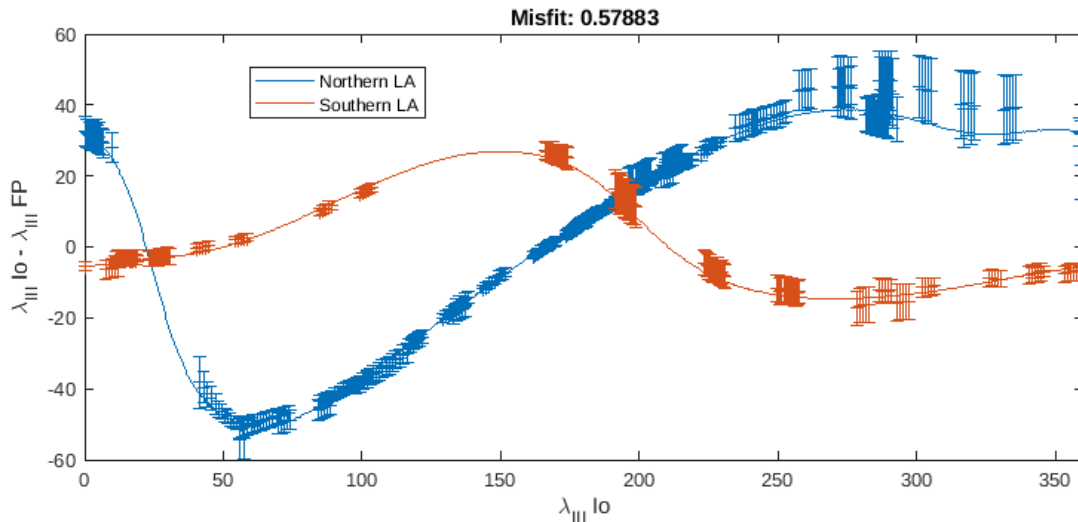


**Figure 5.5.:** The measurements by Bonfond et al. (2017) with error bars for the leading angle of the footprint for the northern (blue) and southern (red) main Alfvén wing. The best fit model with a misfit of  $\chi = 0.57883$  is shown as solid lines. The model was  $T^* = 96$  eV and  $n_0 = 1830$  cm $^{-3}$

is introduced. The basic concept behind the  $L_2$  norm and the corresponding cost function and misfit are the independence of the measurements and the assumption of a normal distributed error. Both conditions are not strictly fulfilled here, since the measurements were interdependent and might have systematic errors. For this fairly simple inversion the  $L_2$  norm however suffices. The best model fit with an error weighted misfit of  $\chi = 0.58$  is shown in Figure 5.5. A  $\chi < 1$  is traditionally regarded as over-fitted. However, since we can not regard the measurements as independent, this concept does not easily apply. The best fit model was a temperature of  $T^* = 96$  eV and a central torus number density of  $1830$  cm $^{-3}$ . The density value is slightly below other models in the literature. Phipps et al. (2018) suggested slightly higher values for the warm torus peak density of  $n_0 = 2430$  cm $^{-3}$ , similar to the value given by Dougherty et al. (2017) of  $n_0 = 2451$  cm $^{-3}$ . Bagenal and Delamere (2011) had a lower maximum torus number density of  $n_0 = 2001$  cm $^{-3}$  in their model. For the temperature Dougherty et al. (2017) had a very low electron temperature  $T_e \approx 5$  eV at Io's orbit with a suprathermal subpopulation of  $T_{e,hot} = 35$  eV, both temperatures rapidly increasing with distance to Jupiter. For the ion temperature, the model of Dougherty et al. (2017) provides a value of  $T_i = 79.3$  eV at Io, while Phipps et al. (2018) occultation measurements show a similar, albeit slightly lower value of  $T_i \approx 70$  eV. Generally, the temperatures are in good agreement with the given values. The density profile along the Io flux tube starting from the torus center is shown in Figure 5.6. The temperature and density value result in a one way travel time from the torus center towards Jupiter's ionosphere of  $t_0 = 365$  s. Furthermore, the temperature results in a scale height of about  $H = 0.9R_J$ , which is in between the values given for the scale height of the ribbon and warm torus by Phipps et al. (2018).

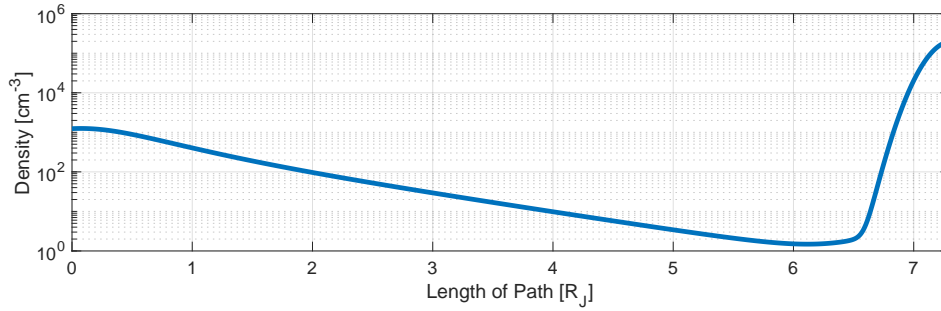


**Figure 5.6.:** Density distribution along the magnetic field line, starting at the torus at  $x = 0$  with a density of  $n_0 = 1830 \text{ cm}^{-3}$ , reaching a minimum of almost  $1 \text{ cm}^{-3}$  at high latitudes and then increasing towards the Jovian ionosphere.

## 5.4. Position of the Secondary Tail Spots

Parts of this section have been submitted to JGR-Space Physics and have been accepted for publication. With the JRM09 magnetic field model and a density model along the magnetic field lines, we can not only calculate the footprint of the main Alfvén wing, but also of the reflected Alfvén wings using the position of the ionosphere and the strongest relative Alfvén phase velocity gradient (cf. Figure 5.3) as reflection points for the Alfvén waves. This results in a multitude of reflected Alfvén wings, each with its own footprint. This can be used to answer the first question posed at the beginning of this chapter: Are the location and separation of the Io footprint and its tail spots consistent with established magnetic field and mass density models? Not included here are trans-hemispheric electron beams that can explain the leading spot emissions and might contribute to some emission features in the tail, albeit to a lesser extent. The observations by Mura et al. (2018) provided positions of the main Alfvén wing spot and secondary spots for two occasions, one at each hemisphere. Using the position of the strongest emission corresponding to the main Alfvén wing the position of Io can be inferred. For the observation of the northern footprint, when Io was roughly at  $\varphi_{Io} \approx 80^\circ$  and  $3.1^\circ$  north of the torus center, the results are shown in Figure 5.7. The calculated positions along the tail coincide with some of the emission maxima in the tail, referred to as tail spots. The reflection pattern corresponding to the calculated positions of the secondary spots is shown on the right hand side of 5.7. For the southern spots observed by Mura et al. (2018) the study yielded similar results. Even though not every feature in the tail can be mapped with this reflection pattern, this study shows that the separation between the main spot and tail spots can be explained with reflections at the torus boundary and Jovian ionosphere.

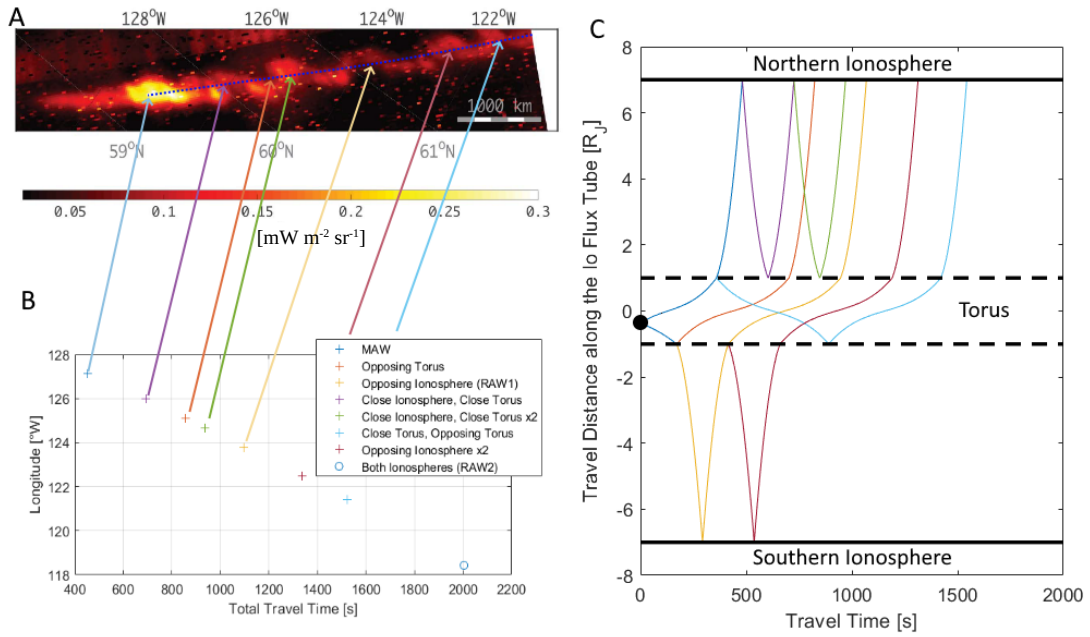


**Figure 5.7.:** **A:** JIRAM image of the northern footprint by Mura et al. (2018). The observation was taken when Io was at  $\varphi_{Io} \approx 80^\circ$  western longitude. With a leading angle of  $\Delta\varphi = -47^\circ$ , this results in a main Alfvén wing footprint at  $\approx 127^\circ$  W, in agreement with the observation shown here. **B:** Calculated longitudinal positions of footprints of secondary Alfvén wings for different reflection patterns. **C:** Reflection patterns corresponding to the footprint positions shown in **B**. The travel path of the first seven footprints on the northern Jovian ionosphere are shown.

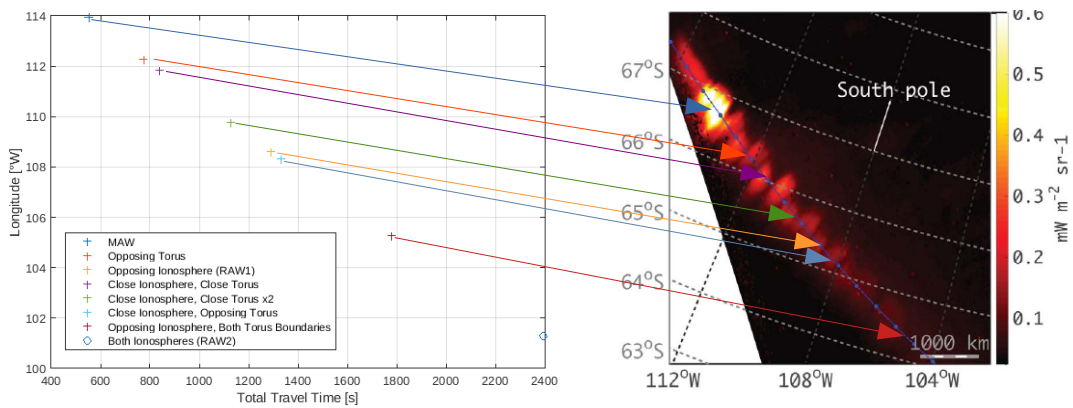


**Figure 5.8.:** Left: Calculated longitudinal positions of the footprints of secondary Alfvén wings for different reflection patterns when Io was at  $\approx 135^\circ$  W. Right: JIRAM observation of the southern Io footprint emissions by Mura et al. (2018) with the mapped positions of the secondary footprints. The reflection pattern of the corresponding Alfvén wing is similar to those shown in Figure 5.7

---

MHD Simulation Setup

---

Single fluid MHD simulations are carried out in order to investigate the different mechanisms that could lead to the alternating structures in the Io footprint tail observed by Mura et al. (2018) and Moirano et al. (2021). In this chapter the *PLUTO* code used for these simulations is presented. Afterwards, the basic model background model with the used parameters is introduced and the specifications of the domain, grid and the boundary conditions are defined. On some basic simulation setups the code is validated and compared to expected theoretical outcomes. The terms in the governing basic equations are compared to each other with a scale analysis followed by a short discussion, whether the assumptions made are justified. In the last part the reference model without symmetry breaking effects is presented.

## 6.1. The PLUTO Code

PLUTO is a multiphysics numerical code developed for the treatment of astrophysical fluids (Mignone et al., 2007). The code uses the finite volume (FV) scheme to integrate the governing equations formulated as conservation law.

$$\frac{\partial \mathbf{U}}{\partial t} = -\nabla \cdot \mathbf{T}(\mathbf{U}) + \mathbf{S}(\mathbf{U}) \quad (6.1)$$

Here,  $\mathbf{U}$  is the state vector of conservative quantities like density  $\rho$ , momentum  $\rho \mathbf{v}$ , pressure  $p$  or magnetic field strength  $\mathbf{B}$  and  $\mathbf{T}(\mathbf{U})$  defines the fluxes of  $\mathbf{U}$ , while  $\mathbf{S}(\mathbf{U})$  are the source and sink terms. The finite volume formalism has superior accuracy and robustness when used for conservation laws (Falle, 2002). In this work, PLUTO is used as a single fluid Hall-MHD code. It solves the following conservation laws:

$$\frac{\partial \rho}{\partial t} + \nabla \cdot (\rho \mathbf{v}) = 0 \quad (6.2)$$

$$\frac{\partial \rho \mathbf{v}}{\partial t} + \nabla \cdot \left( \rho \mathbf{v} \otimes \mathbf{v} - \mathbf{B} \otimes \mathbf{B} + \underline{\underline{I}} \left( p + \frac{B^2}{2} \right) \right)^T = 0 \quad (6.3)$$

$$\frac{\partial \mathbf{B}}{\partial t} + \nabla \cdot (-\mathbf{v} \times \mathbf{B}) = 0 \quad (6.4)$$

$$\frac{1}{2} \frac{\partial (3p + \rho v^2 + B^2)}{\partial t} + \nabla \cdot \left[ \left( \frac{\rho v^2}{2} + \frac{5}{2} p \right) \mathbf{v} - (\mathbf{v} \times \mathbf{B}) \times \mathbf{B} \right] = 0 \quad (6.5)$$

In equation (6.3),  $\otimes$  denotes the tensorial product and  $\underline{\underline{I}}$  is the identity matrix. Additionally to solving equations (6.2) to (6.5), the code supports different methods to keep the divergence of the magnetic field under control. This is important, since equations (6.3), (6.4) and (6.5) have non-zero flux terms that are proportional to  $\nabla \cdot \mathbf{B}$ .

## 6.2. Model, Grid and Parameters

PLUTO has the potential to support irregular grids and adapted mesh refinement. However, in this work we use a simple rectangular grid with constant grid spacing  $\Delta x = \Delta y = \Delta z = 0.2R_{Io}$ . Values for the grid size are given in Io radii  $R_{Io}$ . Grids with smaller cells have been tested, but no benefits regarding accuracy or numerical robustness have been found. The domain ranges from  $-20$  to  $100$  in x-direction,  $-12$  to  $12$  in y-direction and  $-65$  to  $65$  in z-direction. The domain was set up that possible reflections at the boundaries do not influence the results significantly. This results in a total number of [601x121x651] grid points. The total simulation time was set to 80 minutes. This on the one hand ensures that the plasma travels through the whole domain  $\tau = 120R_{Io}/v_0 \approx 64$  minutes, ensuring steady state, while on the other hand preventing reflections at the  $x = 120$  boundary to affect the simulation results significantly. We use two types of boundary conditions: inflow and outflow. Outflow boundaries have Neumann boundary conditions that copy the value of the boundary cells to the ghost cells. This ensures that the gradient through the boundary of the chosen quantity vanishes, i.e.  $\nabla_{boundary} \mathbf{U} = 0$ . The outflow boundary condition is used for all variables and all boundaries except at  $x = -20$ . At that boundary, inflow conditions are applied, which is a Dirichlet boundary conditions and sets a constant value in the ghost cells. The set values for  $\mathbf{v}_0$ ,  $p_0$  and  $\mathbf{B}_0$  are shown in table 6.1, while the density  $\rho_0 = \rho_0(z)$  is not constant along the boundary and given by the chosen background density model.

The Jovian ionosphere must be included to implement a region where the Alfvén velocity gradient is strong to permit reflections. Also a reference region is needed where energy fluxes can be used as a diagnostic to infer position, morphology and intensity of emission features created by particle acceleration. However, we used a simplified geometry, where the normally curved magnetic field lines are straightened and a homogeneous background magnetic field in negative z-direction can be used. This allows the application of a uniform rectangular grid and simplifies the separation of different effects from each other and from numerical inaccuracies. The constant magnetic field strength  $B_0 = 1720$  nT is chosen to match the values in the vicinity of Io, just as the maximum number density  $n_I$  at the torus center that were inferred from the modelling and inversion in Chapter 5. From that the mass density  $\rho = n \cdot m_i$  for an average ion mass of  $m_i = 24$  amu is calculated. The chosen ion mass is the approximated average ion mass of the torus region (e.g. Dougherty et al. (2017)). The simulation domain with the mass density model is shown in Figure 6.1. The number density model consists of three parts and is only dependent on the z-coordinate.

$$n(z) = n_0 + n_T(z) + n_I(z) \quad (6.6)$$

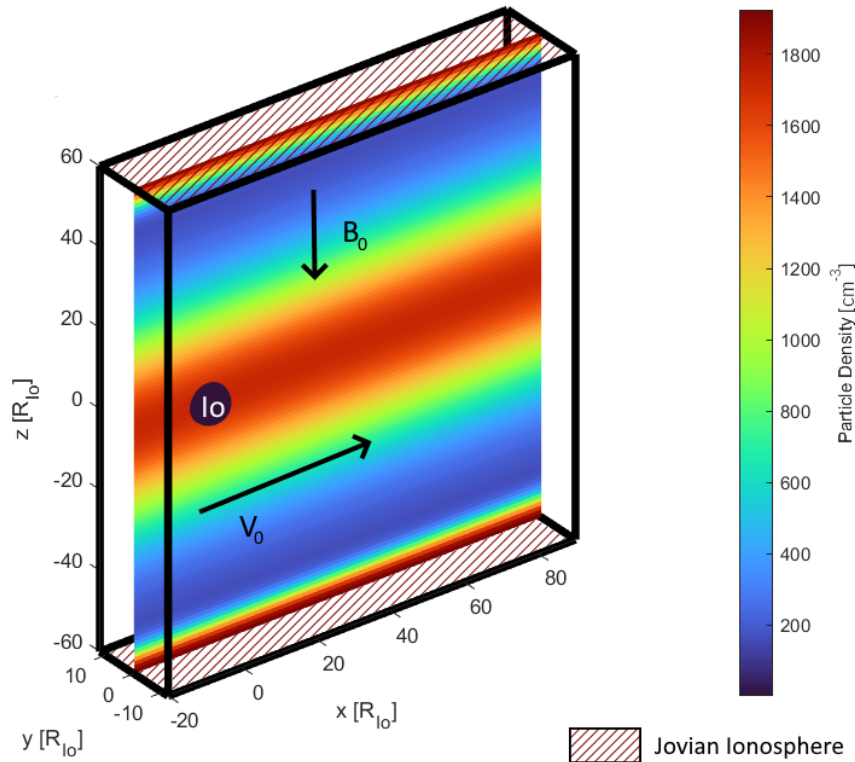


**Figure 6.1.:** Background mass density model. The mass density in the Io torus center ( $z = 0$ ) is  $\rho_0(z = 0) = 7 \cdot 10^{-17} \text{kg/m}^3$  with a chosen ion mass of  $m_i = 24$  amu and decreases with an exponential scale height law towards positive and negative  $z$ -direction. Near the Jovian ionosphere at  $z = \pm 60 R_{Io}$ , the density increases exponentially. The background magnetic field points towards negative  $z$ -direction whereas the incoming plasma flow in positive  $x$ -direction. Io is located at the center.

The first term on the right hand side controls the minimum number density  $n_0 = 1.8 \cdot 10^8 \text{ m}^{-3}$ , which is roughly 10% of the maximum number density in the torus. The second term shows the additional torus number density

$$n_T = (n_{T,0} - n_0) \exp \left[ -\frac{z^2}{H_T^2} \right] \quad (6.7)$$

and decreases exponentially with the torus scale height  $H_T = 25 R_{Io} \approx 0.65 R_J$ . This scale height is in agreement with the findings of Phipps et al. (2018) and Dougherty et al. (2017) for the ribbon region next to the warm torus. The central torus number density of  $n_{T,0} = 1.8 \cdot 10^9 \text{ m}^{-3}$  results in a central torus Alfvén velocity of  $v_{A,0} = 181 \text{ km/s}$ . To account for the density increase near the Jovian ionosphere, where reflections occur, we implemented the third term

$$n_I(z) = n_{I,0} \exp \left[ -\frac{z_I - |z|}{H_I} \right] \quad (6.8)$$

in the number density model. The position  $z_I = 60 R_{Io}$  marks the beginning of Jupiter's ionosphere, where the density increases with the ionospheric scale height  $H_I = 0.4 R_{Io} \approx 730 \text{ km}$ . The base number density for the ionosphere was chosen to be  $n_{I,0} = 10^{11} \text{ m}^{-3}$ . The chosen density model ensures that the simulated travel times for the Alfvén wave, inside and outside the torus, are in agreement with the travel times determined by the

**Table 6.1.:** Properties of the reference simulation

Property	Symbol	Value
Io Radius	$R_{Io}$	1822 km
Background Magnetic Field	$\mathbf{B}_0$	-1720 nT $\mathbf{e}_z$
Inflow Plasma Bulk Velocity	$\mathbf{v}_0$	57 km s <sup>-1</sup> $\mathbf{e}_x$
Convection Time	$\tau$	$2R_{Io}/v_0 = 64$ s
Alfvén Travel Time	$t_0$	365 s
Central Torus Plasma Number Density	$n_{T,0}$	$1.8 \cdot 10^9$ m <sup>-3</sup>
Central Torus Alfvén Velocity	$v_{A,0}$	181 km s <sup>-1</sup>
Central Torus Alfvén Mach Number	$M_A$	0.31
Minimum Background Number Density	$n_0$	$0.1n_{T,0} = 1.8 \cdot 10^8$ m <sup>-3</sup>
Background Pressure	$p_0$	29 nPa
Ion Cyclotron Frequency <sup>a</sup>	$\omega$	10 s <sup>-1</sup>
Io Neutral Gas Scale Height	$H$	200 km
Central Io Neutral Gas Density	$n_n$	$3.3 \cdot 10^{12}$ m <sup>-3</sup>
Central Ion-Neutral Collision Frequency	$\nu_0$	1.14 s <sup>-1</sup>
Io's Pedersen Conductance	$\Sigma_P$	50 S
Central Torus Alfvén Conductance	$\Sigma_A$	4.3 S
Plasma Beta	$\beta$	0.01

<sup>a</sup> For an  $O^+$  ion

inversion in Section 5.3 and similar models (e.g. Hinton et al. (2019)). The total travel time for the Alfvén wave from the torus center to the Jovian ionosphere at  $z_I$  is  $t_0 = t(z_I) \approx 365$  s. The background plasma flow velocity is set to  $v_0 = 57$  km/s in positive x-direction, which is the relative velocity of the co-rotating plasma to Io's orbital motion. This yields an alfvénic Mach number of  $M_A = v_0/v_{A,0} = 0.31$  in the torus center. The background thermal pressure  $p_0$  of the plasma was set to 29 nPa, which translates to a plasma temperature of roughly 100 eV in the center of the Io plasma torus. This is in agreement with the observed ion temperatures (Delamere et al., 2005; Dougherty et al., 2017). The plasma around Io is not expected to have constant thermal pressure along the field lines. However, in the case with straightened field lines, the retracting forces, such as centrifugal forces, thermal pressure anisotropy, magnetic pressure gradients and ambipolar electric fields, to stabilize the torus are not included in the model. A change in pressure in our model would therefore smooth the density variations over time and the density gradients at the torus boundary and Jupiter's ionosphere would be unstable. Therefore a constant background pressure is applied in all simulations. The chosen thermal pressure leads to a low  $\beta = 0.01$  and the simulation is dominated by the magnetic pressure.

### 6.3. Io as Neutral Gas Cloud

In this work, Io is represented as a neutral gas cloud in the center of the coordinate system. As discussed in chapter 4, the far field interaction depends to the height integrated Pedersen and Hall conductance, which can be characterized by a spatially dependent collision frequency  $\nu$ . This parameterization of Io however does not reflect the near field

interactions accurately. Since this work aims at representing the far field interaction, especially the propagation and structure of the Alfvén wings, a characterization of Io as neutral gas is sufficient.

The neutral gas density  $n_n(\mathbf{r})$  is constant with a value of  $n_{n,0} = 5.710^{15} \text{m}^{-3}$  inside Io and decreases radially with a scale height  $H = 200 \text{ km}$  outside.

$$n_n(r) = n_{n,0} \begin{cases} 1 & r < R_{Io} \\ \exp\left[-\frac{r}{H}\right] & r > R_{Io} \end{cases} \quad (6.9)$$

The velocity cross section product of  $\sigma_C v = 2 \cdot 10^{-16} \text{m}^3 \text{s}^{-1}$ , as discussed in chapter 3.5, yields a collision frequency  $\nu = \sigma_C v n_n = 1.14 \text{s}^{-1}$  inside the moon. Neglecting the Hall term, this leads to a Pedersen conductivity inside Io of  $\sigma_P(r < R_{Io}) = 28 \mu\text{S}$ . Hence, the resulting Pedersen conductance, integrated over the magnetic field line through the center of Io, is  $\Sigma_P = 50 \text{ S}$ . With an Alfvén conductance of  $\Sigma_A = 4.3 \text{ S}$ , this results in an interaction strength of  $\bar{\alpha} = 0.85$  and the interaction can be classified as strong, where the non-linearity of the reflections play an important role. In our simulation Io is at rest and the neutral particles have no bulk movement, i.e.  $\mathbf{v}_n = \mathbf{0}$ . Furthermore, the pressure  $p_n$  of the neutral gas is neglected. This implies the plasma pressure loss to the neutral gas, as discussed in chapter 3.4.

## 6.4. Validation of the Simulation

With the basic model set up and all parameters defined, we need to validate the simulation going forward. We will first look into the generation of the Alfvén wing using a homogeneous background density model with a constant number density of  $n = 1.8 \cdot 10^9 \text{ m}^{-3}$  and compare the fields inside and outside the Alfvén wing to the semi-analytical solutions. Then, we will investigate the reflection behaviour of the Alfvén wing on a strong density gradient that acts as discontinuity. The simulations including reflection will be validated regarding analytical transmission and reflection coefficients and compared to the semi-analytical solutions. Afterwards, simulations with a smoother density gradient will be analyzed and compared to the simulations with the discontinuity. In a next step, we will conduct a scale analysis, where we compare different terms of the governing equations and close with a discussion, whether we can neglect any terms going forward and if the assumptions are justified for our simulations. In the simulation with a homogeneous background mass density the Alfvén wing does not get reflected or refracted. Figure 6.2 shows the velocity perturbation in the plane perpendicular to the background magnetic field  $\mathbf{B}_0$  with the velocity stream lines in the rest frame of Io and Jupiter. In the rest frame of Io, with a background velocity of  $\mathbf{v}_0 = 57000 \text{ m/s } \mathbf{e}_x$ , the plasma flows around the obstacle, getting accelerated at the flanks and decelerated at the center. In the rest frame of Jupiter, where the background velocity is zero, the stream lines show vortices at the flanks of the Alfvén wing. These vortices translate to vortices in the magnetic field that represent the currents  $\mathbf{j}_{\parallel}$  parallel to the Alfvén wing. These velocity fields and the magnetic counterpart resemble the fields produced by the semi-analytic simulations from chapter 4 well.

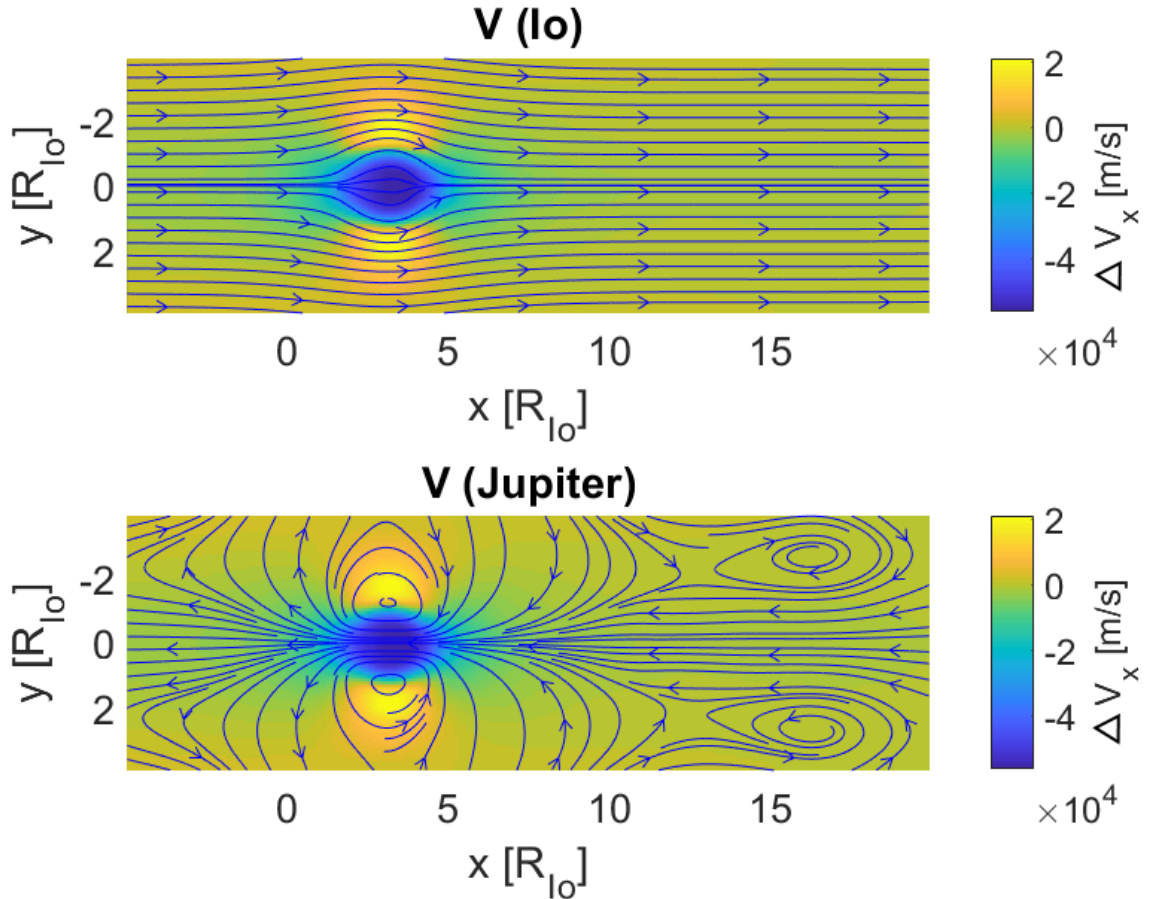


**Figure 6.2.:** Velocity perturbations in x-direction in the  $z = 20R_{Io}$  plane perpendicular to the background magnetic field. The streamlines are added for the velocity field in Io's rest frame (top) and Jupiter's rest frame (bottom), where the background velocity is zero.

#### 6.4.1. Reflection of Alfvén Waves

One very important part of the Io Alfvén wing is its reflection on Alfvén phase velocity gradients. It is necessary to validate the simulation and theory in that regard by comparing the simulation results to the analytical expectations. For that purpose, a simulation was set up with a simplified density profile and lowered interaction strength to avoid non-linear reflections. The mass density separates the domain in three regions. Inside the torus up to a distance of  $z = 15R_{Io}$  in  $z$ -direction from Io, the mass density is constant and has the value  $\rho(|z| < 15R_{Io}) = 24 \text{ amu} \cdot 1.8 \cdot 10^9 \text{ m}^{-3}$ . Then, over a small distance, it drops linearly to a tenth of the value outside the torus, i.e.  $\rho(|z| > 15R_{Io} + L) = 24 \text{ amu} \cdot 1.8 \cdot 10^8 \text{ m}^{-3}$ . The size of the transition region in between  $L$  can vary and should control, whether the density gradient can be regarded as a discontinuity for the incoming Alfvén wave. The maximum incident wavelength parallel to the background magnetic field expected can be calculated as

$$\lambda_{||,max} = \frac{2R_{Io}}{v_0} v_A = \frac{2R_{Io}}{M_A} \approx 6.5R_{Io}. \quad (6.10)$$

However, the incoming wave package consists of a spectrum of wavelengths. As stated in chapter 3.2, wavelengths smaller than the characteristic length scale of the Alfvén

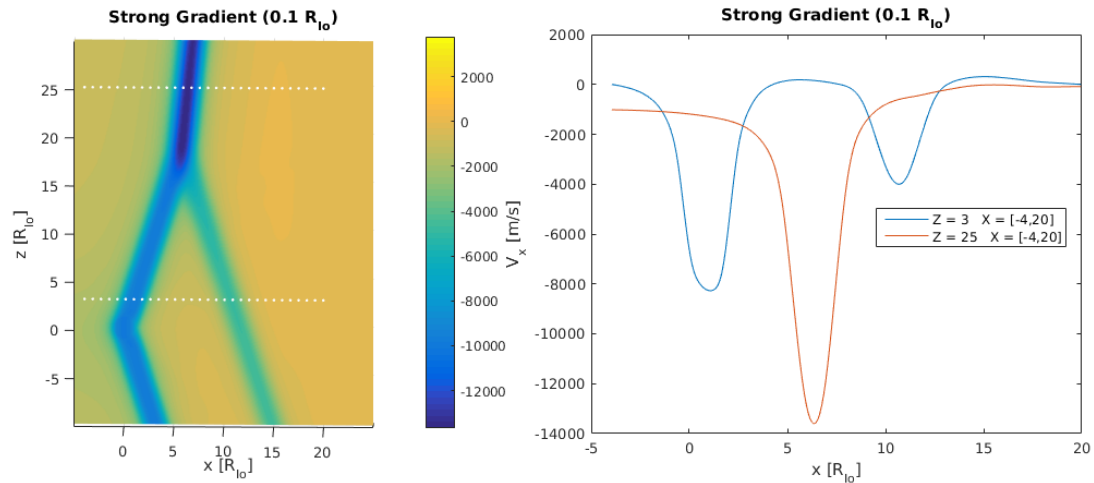


**Figure 6.3.:** Left: The velocity perturbation in x-direction of the simulation. Io is centered at (0,0), where the two Alfvén wings develop. When the northern Alfvén wing encounters the discontinuity at  $z = 15R_{Io}$ , it gets partially reflected and transmitted. Right: The velocity perturbation in x-direction along the two profiles marked by white dots in the left plot. The red line shows the profile at  $z = 25R_{Io}$ , where we only see the transmitted wing. The blue line shows the profile at  $z = 3R_{Io}$ , which is far enough from Io to neglect the effects of other wave modes than the Alfvén wave. This profile shows both, the incident wave at  $x \approx 1R_{Io}$  and the reflected wave at  $x \approx 10R_{Io}$ .

velocity gradient should get less reflected. Therefore, we should already see a weakening in reflection for  $L \approx \lambda_{||,max}$  while for a small transition region  $L \ll \lambda_{||,max}$ , the density gradient should be able to be regarded as a discontinuity. For our simulation, we used  $L = 1R_{Io}$  for the discontinuity and  $L = 4R_{Io}$  for the weakened reflection. First, we will confirm, whether the simulation with the discontinuity gives us the expected results for the most simple case of a reflection as described in chapter 3.2. The reflection and transmission coefficients of a discontinuity, where the mass density drops to one tenth, can be calculated as

$$R_{v,B} = \frac{\sqrt{10} - 1}{\sqrt{10} + 1} = 0.52 \quad (6.11)$$

$$T_v = \frac{2\sqrt{10}}{\sqrt{10} + 1} = 1.52 \quad (6.12)$$

$$T_B = \frac{1}{\sqrt{10} + 1} = 0.48 \quad (6.13)$$

In the simulation, the magnetic field and velocity perturbations for the incident, reflected and transmitted wave have been compared to each other as shown in Figures 6.3 and 6.4. To get a value for the perturbation of the fields for the three different wings, two profiles through the domain have been analyzed. The first profile located after the density transition region with the transmitted wing. The second profile position is chosen between Io and the transition region with enough distance to both of them. This ensures the avoidance of effects from other wave modes generated at Io and simplifies the distinction of the incident from the reflected wing. Along the profiles, the maximum perturbation has been used to characterize the perturbation strengths for the respective wing. The ratio between those values is shown in Table 6.2 and compared to the analytical values. The simulation matches the expected values very well.

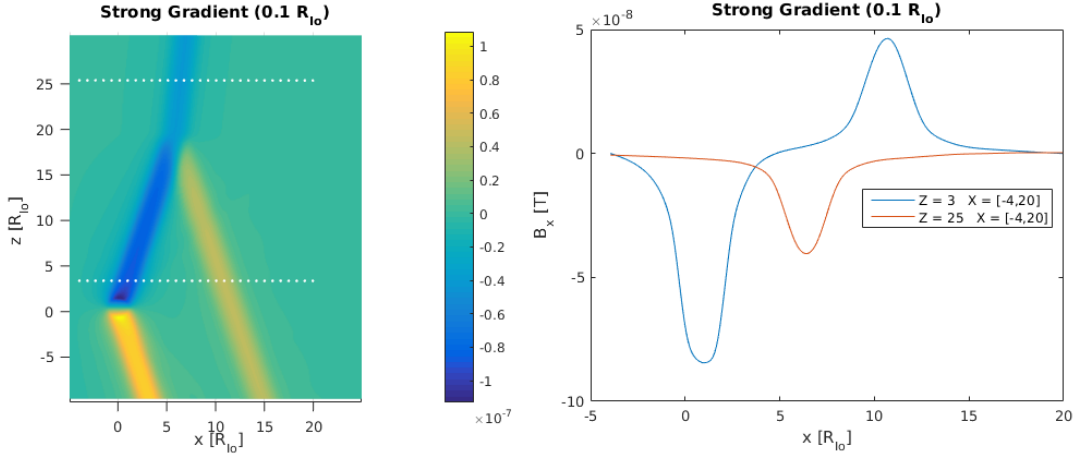


**Figure 6.4.:** Left: The magnetic field perturbation in x-direction of the simulation. Io is centered at (0,0), where the two Alfvén wings develop. When the northern Alfvén wing encounters the discontinuity at  $z = 15R_{Io}$ , it gets partially reflected and transmitted. Right: The magnetic field perturbation in x-direction along the two profiles marked by white dots in the left plot. The red line shows the profile at  $z = 25R_{Io}$ , where we only see the transmitted wing. The blue line shows the profile at  $z = 3R_{Io}$ , which is far enough from Io to neglect the effects of other wave modes than the Alfvén wave. This profile shows both, the incident wave at  $x \approx 1R_{Io}$  and the reflected wave at  $x \approx 10R_{Io}$ .

**Table 6.2.:** Analytical and Numerical Reflection and Transmission Coefficients

Coefficient	Analytical Value	Numerical Value
$R_v$	0.52	0.48
$T_v$	1.52	1.64
$R_B$	-0.52	-0.55
$T_B$	0.48	0.48

Next, we analyze how the reflection strength changes for a slow changing medium. For that, we now also run a simulation with the weaker density gradient  $L = 4R_{Io}$ . Simulations for both density models have been run once using a normal sized gas cloud representing Io, i.e.  $1R_{Io}$ , and once using a gas cloud with a radius of  $0.5R_{Io}$ . The velocity perturbation results for both simulations and the comparison between all 4 cases for reflected and transmitted waves are shown in Figures 6.5 and 6.6. For the simulations with the smaller gas cloud (Figure 6.5), the transmission of the velocity perturbation for both, the strong and the weak gradient, are very similar with the transmitted wave in the case of the weak gradient being slightly larger in perturbation. The perturbation of the reflected wave for the strong gradient is significantly larger than the one for the weak gradient. However, this is partly due to the incident and reflected wave overlapping partially in that region. The difference between the transmitted wave packages is much stronger in the case of a normal sized Io, as shown in Figure 6.6. For the reflected wave, the strong gradient shows a slightly stronger reflection coefficient.

As expected for an Alfvén velocity gradient that can not be regarded as discontinuity, the reflection is stronger for a larger ratio  $\lambda_{||,max}/L$ . Increasing the transition region size  $L$  or reducing the size of the gas cloud, thus decreasing  $\lambda_{||,max}$ , results in a larger amplitude in the transmitted wave while decreasing the reflected amplitude. Another

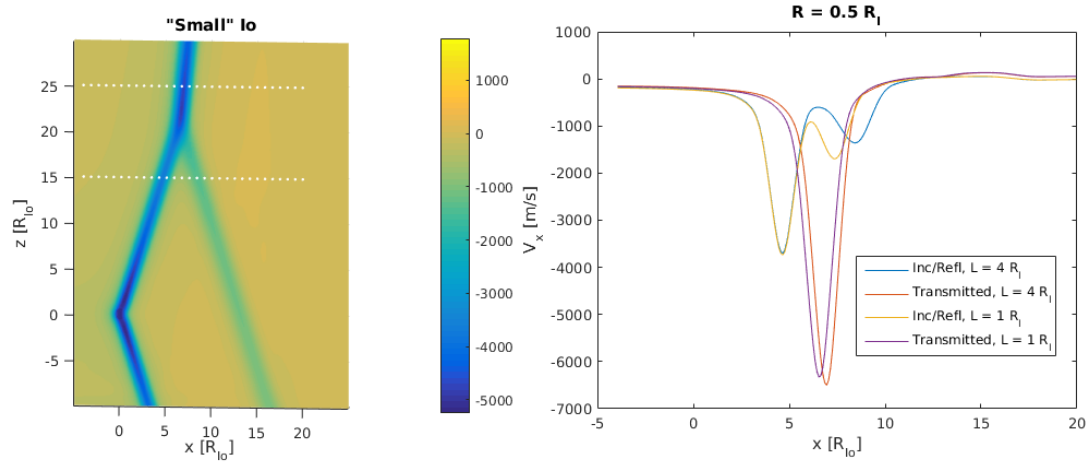


**Figure 6.5.:** Left: Velocity perturbation of the simulation with a smaller sized gas cloud with  $R = 0.5R_{I_0}$ . Right: The velocity perturbation along the dotted lines in the left plot. The simulation has been conducted using a strong density gradient with  $L = 1R_{I_0}$  and a weak density gradient using  $L = 4R_{I_0}$ . The transmitted perturbation for the weak gradient (red) is slightly larger than the transmitted perturbation for the strong gradient (purple). Similarly, the reflected perturbation for the weak gradient (blue) is lower than the reflected perturbation for the strong gradient (yellow).

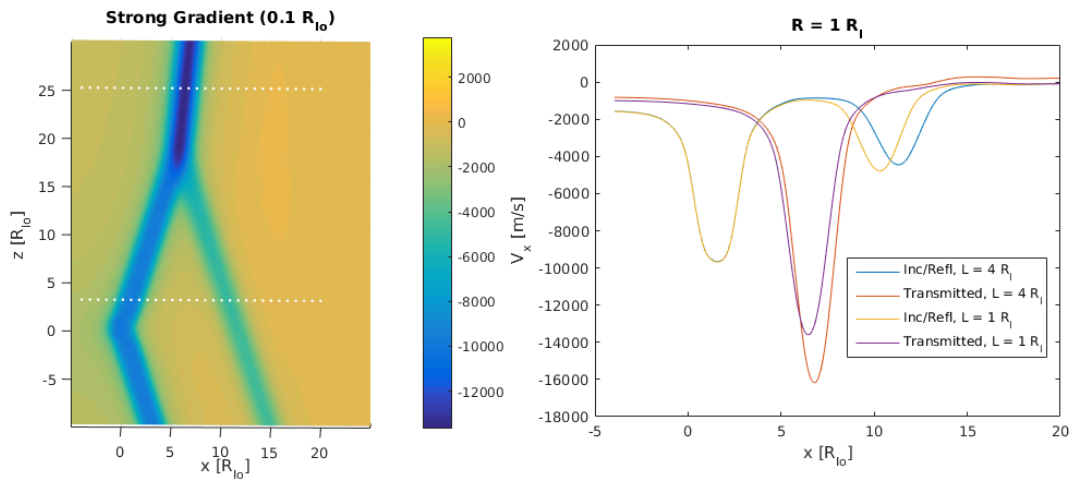


**Figure 6.6.:** Left: Velocity perturbation of the simulation with a normal sized gas cloud with  $R = 1R_{I_0}$ . Right: The velocity perturbation along the dotted lines in the left plot. The simulation has been conducted using a strong density gradient with  $L = 1R_{I_0}$  and a weak density gradient using  $L = 4R_{I_0}$ . The transmitted perturbation for the weak gradient (red) is significantly larger than the transmitted perturbation for the strong gradient (purple). Similarly, the reflected perturbation for the weak gradient (blue) is slightly lower than the reflected perturbation for the strong gradient (yellow).

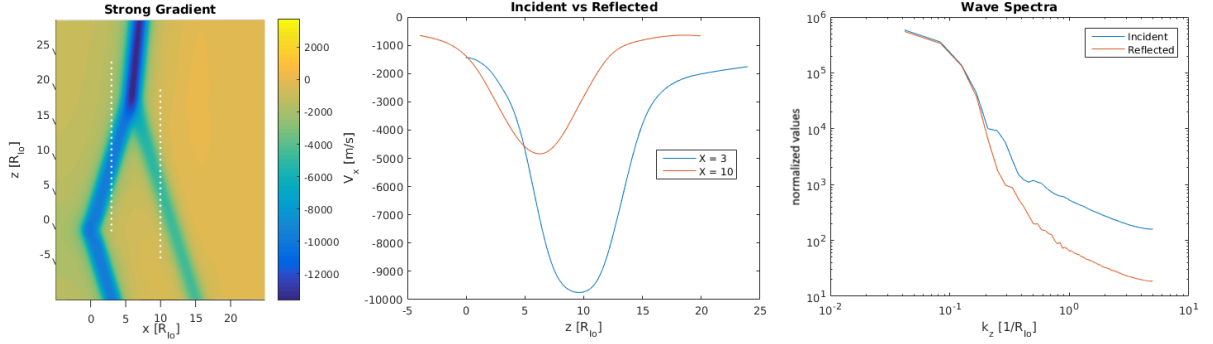


**Figure 6.7.:** Left: Velocity perturbation of the simulation with normal sized Io and strong density gradient ( $L = 1R_{Io}$ ). Center: The velocity perturbation along the profiles shown in the left plot. The blue curve shows the incident wave package while the red curve shows the reflected wave package. Right: Spectrum of the two velocity perturbation curves shown in the center. The spectrum of the reflected wave package is scaled by the expected reflection coefficient resulting in them almost overlapping for large parallel wave length, i.e. small parallel wave numbers  $k_z$ .

way of verifying this result is looking into the spectrum of transmitted and incident wave and compare them, identifying which wavelengths get reflected. For that purpose we look at profiles along the magnetic field lines as shown in Figure 6.7 that cut through the incident and reflected Alfvén wing. In a next step, we Fourier transform the obtained velocity perturbation distributions and get a spectrum for the parallel wave number  $k_z$ . To compare the two spectra for incident and reflected wave, the spectrum of the reflected wave is scaled by  $1/R_v$ . If the density gradient was a perfect discontinuity for all wave lengths in the wave package, the two curves should theoretically overlap. However, we see that the spectrum of the reflected wave package has less energy in the high parallel wave number, i.e. low parallel wave length range. In particular, the curves separate around  $k_z \approx 0.2/R_{Io}$ , which translates to a wavelength of about  $\lambda_{\parallel} \approx 0.8R_{Io}$ . That is roughly the size of the transition region  $L = 1R_{Io}$ , which ones more confirms that the reflection coefficient depends on the wave length and is only close to theoretically expected values for wavelength larger than the characteristic length scale of the Alfvén velocity gradient and drops off for lower wavelengths.

In a final step, we will look how the morphology of the transmitted and reflected Alfvén wings change compared to the incident Alfvén wing in the case of a strong interaction. For that purpose, a simulation was run with a strong density gradient ( $L = 1R_{Io}$ ) and a high interaction strength of  $\bar{\alpha} = 0.85$ . The Poynting flux in z-direction through a plane located before the reflection and after the reflection is shown in Figure 6.8. We now compare the results to Figure 4.11 that show the slides of the purely alfvénic simulation. In both, the MHD simulation and the semi-analytical Alfvén wing simulation, the reflected Alfvén wing is stretched and narrowed while the transmitted Alfvén wing resembles the aforementioned horseshoe shape. This indicates that the explanation for the development of the morphology of reflected and transmitted Alfvén wing, given in Chapter 4, is plausible.

### 6.4.2. Force Balance and Conductivities

In this part, we first want to look into the assumptions made regarding the derivation of Pedersen and Hall conductivity in chapter 3.5. There, we claimed that the currents perpendicular to the magnetic field are associated with a force balance between the Lorentz

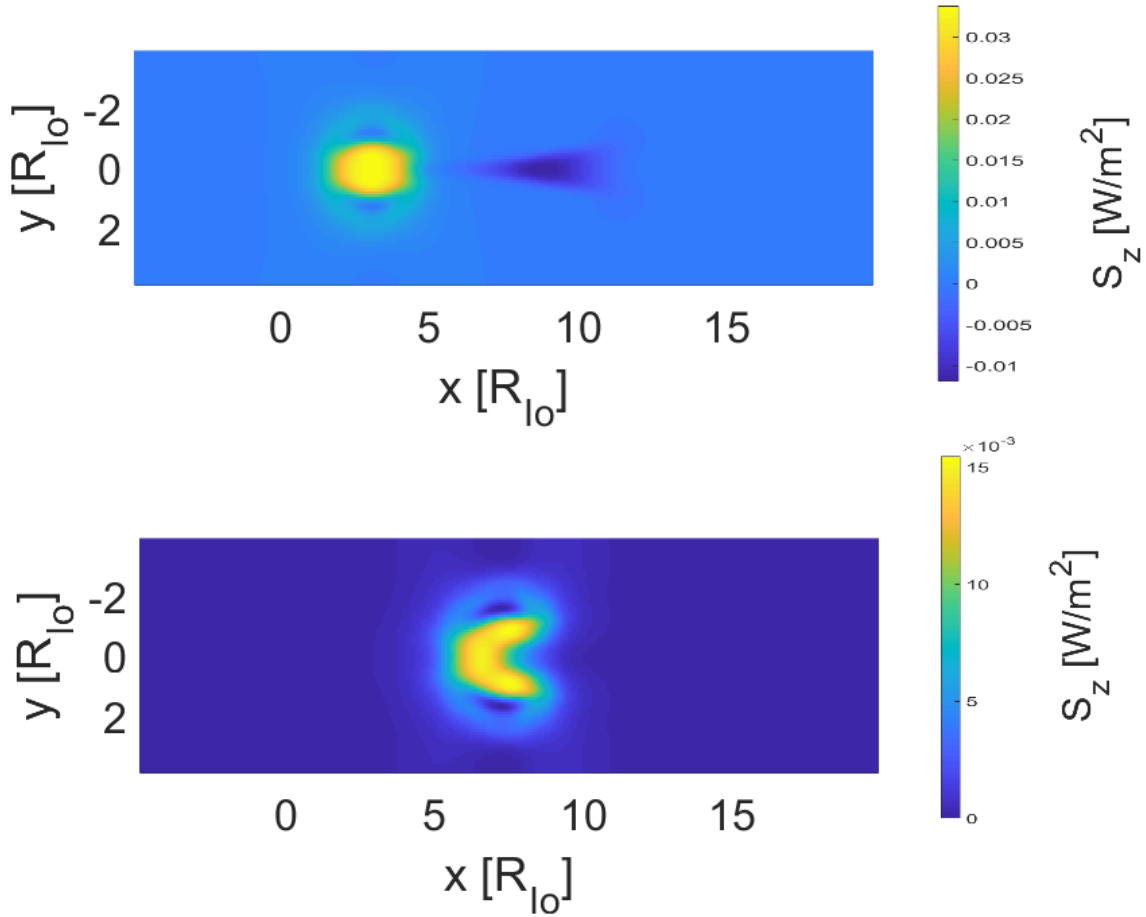


**Figure 6.8.:** Poynting flux in positive z-direction for a simulation with high interaction strength below (top) and above (bottom) the density gradient. The top plot shows the incident Alfvén wing on the left side at  $x \approx 3 - 5R_{Io}$  and the reflected Alfvén wing with negative Poynting fluxes on the right side at  $x \approx 6 - 11R_{Io}$ . The bottom plot shows the transmitted Alfvén wing with its changed morphology. All Poynting fluxes are calculated in the rest frame of the unperturbed plasma flow.

force and the collision term in the momentum equation. To validate this assertion, the advection term and the three forces, i.e. pressure gradient, Lorentz force and the collision term, in the momentum equation have been analyzed. For that we use a simplified simulation without a constant background density and thus without reflections. We wait until the simulation appears to be stationary and we can neglect derivatives with respect to time, in particular  $\partial \mathbf{v} / \partial t = 0$ . To confirm the steady state, we can calculate the sum of all terms in the velocity equation and see if they are negligible compared to each term. The resulting accumulated force is shown in Figure 6.9 and is proportional to  $\partial \mathbf{v} / \partial t$ . Its maximum values are on the order of  $10^{-14} \text{ N/m}^3$  and therefore more than two orders of magnitude below the Lorentz force and the collision term, both at the order of  $10^{-12} \text{ N/m}^3$ . This is a good indication that the fields will not change significantly any more and the simulation can be regarded as steady state.

A slice through Io in the x-y-plane for the four terms in the velocity evolution equation in x direction is shown in Figure 6.10. The compression of the plasma increases the pressure inside the neutral gas cloud ( $r < 1R_{Io}$ ). This results in positive pressure gradient in x direction in the front part of the gas cloud and negative pressure gradient in x direction

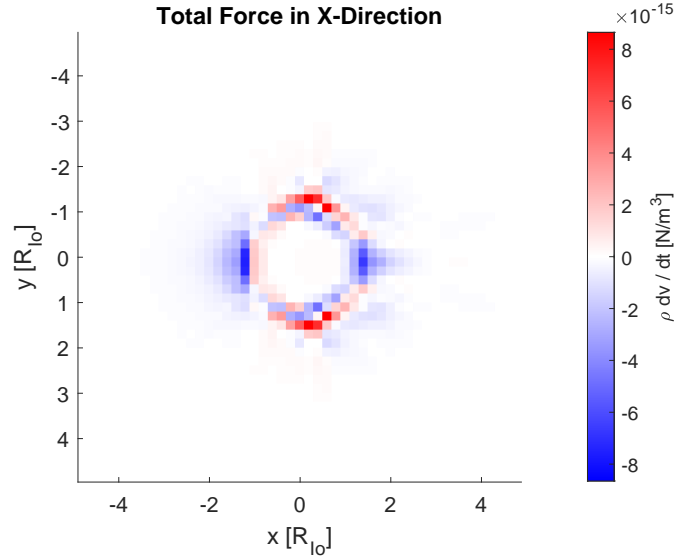


**Figure 6.9.:** The x-component of the temporal change in mass density weighted velocity, i.e.  $\rho \partial v_x / \partial t$ . The values are below the order of  $10^{-14}$  N/m<sup>3</sup>.

in the back part of the gas cloud. The deceleration of the plasma inside the gas cloud and the acceleration around it results in the star light pattern, seen in the plot of the advection term. The two lower plots in Figure 6.10 show the aforementioned force balance between the Lorentz force and the collision term. The two forces inside the gas cloud are opposite and similar in strength. Therefore, the assumptions made to derive the Pedersen and Hall currents for a neutral gas cloud appear justified.

However, there are not only currents perpendicular to the background magnetic field inside the gas cloud. Figure 6.11 shows the  $\mathbf{J} \times \mathbf{B}$  force and the advection term on the same color bar scale. As it can be seen, outside of the gas cloud those two terms balance each other out. The associated current is needed for the plasma to return to co-rotational velocities. While the transient currents due to collisions are locally limited to the neutral gas cloud, the current in the wake of the obstacle decreases exponentially with distance to Io (Vasyliūnas, 2016). Figure 6.12 also shows the advection term and Lorentz force in x-direction, but at a distance of  $z = 20R_{Io}$ . As it can be seen, these currents continue along the Alfvén characteristic. The physical reason behind these currents can be understood as follows: The perturbation of the velocity around the obstacle propagates to the ionosphere, where the differential velocity between the neutral unperturbed particles and the perturbed plasma creates Pedersen currents, that close around Io and Io’s Alfvén wing. The closing currents, as seen in Figures 6.11 and 6.12, accelerates or decelerates the plasma proportional to the difference to co-rotational velocities. Even though we do not represent Jupiter’s ionosphere in our simulations, the boundary conditions of magnetic field and flow velocity serve a similar function.

In a final step of the validation we turn the Hall effect in our simulation on. Here, we are interested in the force balance in both, x- and y-direction. For that purpose, we look at a profile along the x-axis for the collision term and the Lorentz force. Figure 6.13 shows both forces along the x-axis in the vicinity of Io for both, the x-component and the y-component. The force balance can well be seen inside the gas cloud ( $|x| < 1$ ). Outside the gas cloud the Lorentz force is stronger and again counteracts the advection term.

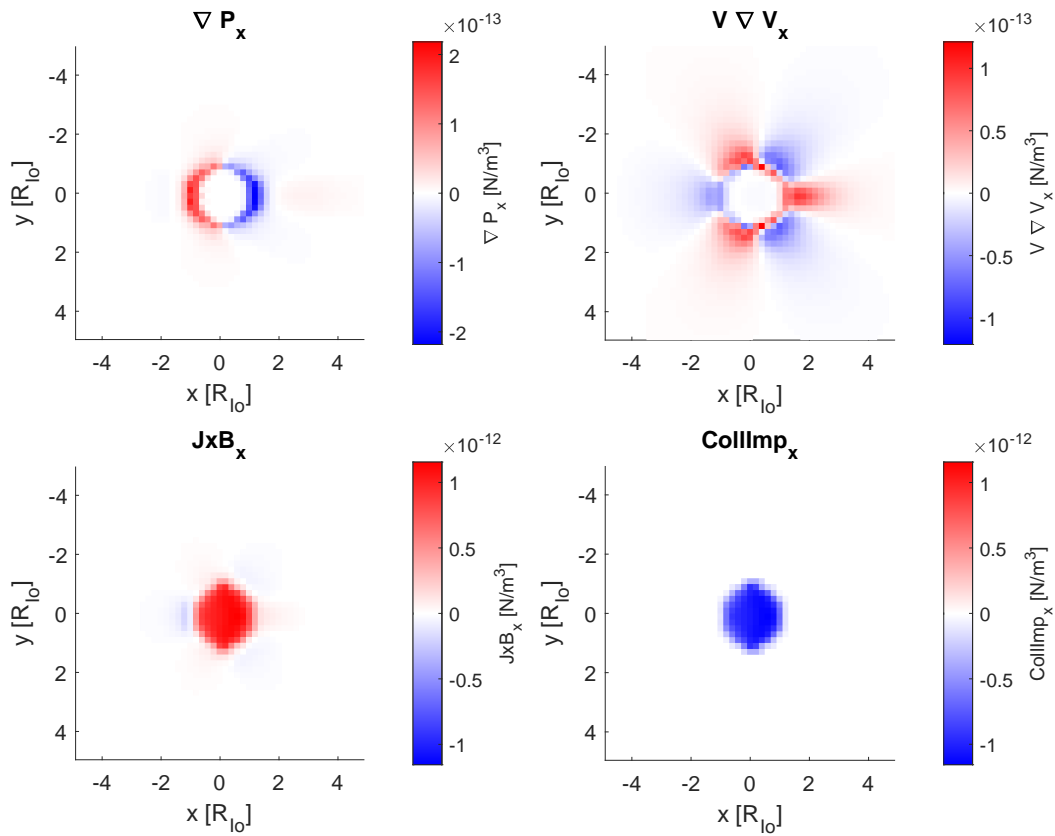


**Figure 6.10.:** The x-component of each of the four terms of the velocity equation in the  $z = 0$  plane. Io is located at  $(0,0)$  and has a radius of  $1R_{Io}$ . Top left: The pressure gradient in x-direction. The decelerated plasma results in higher densities and pressure inside the neutral gas cloud. Top right: The advection term in x-direction. The plasma returns to co-rotational speeds outside of the neutral gas cloud. Bottom left: The Lorentz force in x-direction counteracts the plasma deceleration due to collisions inside the neutral gas cloud in the steady state. Bottom right: The collision term in x-direction is nearly constant inside the neutral gas cloud and vanishes rapidly outside.

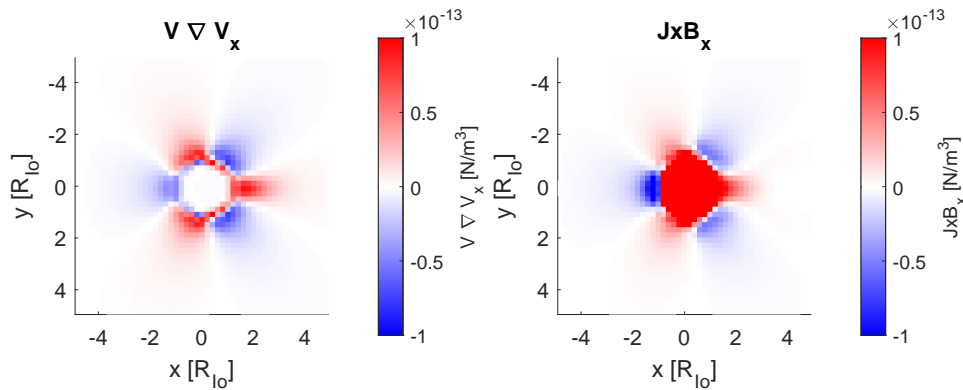


**Figure 6.11.:** The x-component of the advection term and the Lorentz force in the  $z = 0$  plane. Here, the colorbars are adjusted to show highlight the star like structures outside the neutral gas cloud, which are similar in shape and value for both terms.

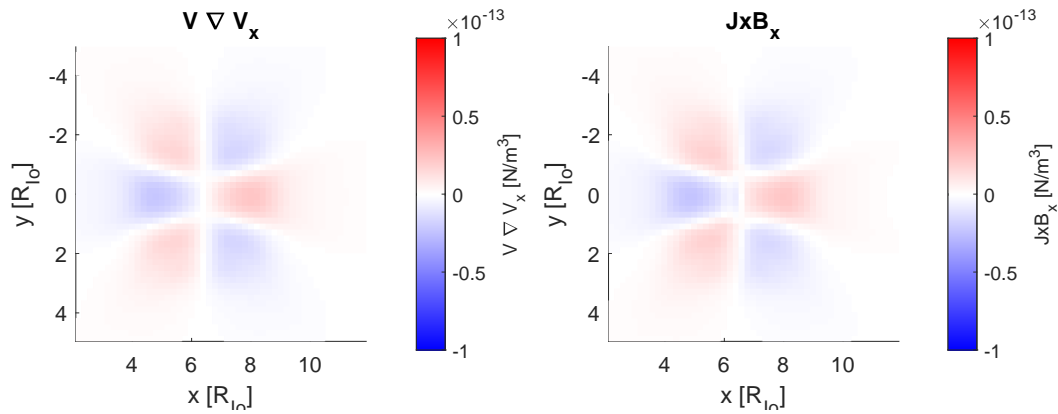


**Figure 6.12.:** The x-component of the advection term and the Lorentz force in the  $z = 20$  plane. The terms balance each other.

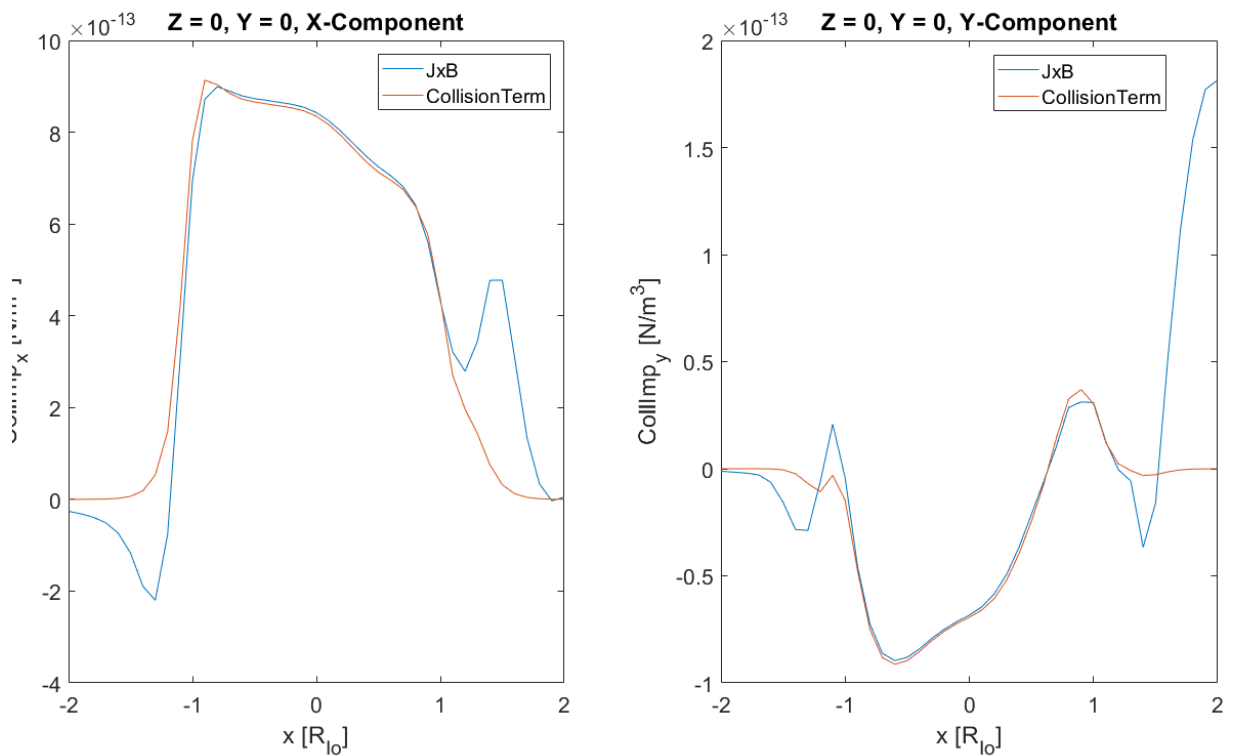


**Figure 6.13.:** The x-components (left) and the y-components (right) of the collision term in red and the Lorentz force in blue on the x-axis. Inside the neutral gas cloud ( $-1 < x < 1$ ) the terms balance each other.

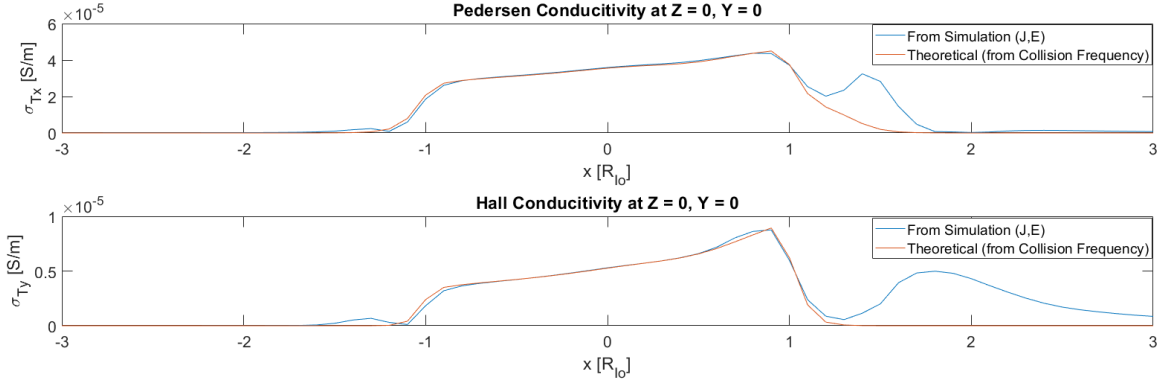


**Figure 6.14.:** Pedersen (top) and Hall conductivity (bottom) along the x-axis. The values derived from collision frequency (red) are compared to the values computed from the simulation results (blue). The values match each other inside the neutral gas cloud for both conductivities.

We can also look at our expected values for the Pedersen and Hall conductances derived from the collision frequency as in equations (3.73) and (3.74) and compare them to values from the simulation. The currents and electric fields derived from the magnetic field and velocity can be computed into conductivities by:

$$\sigma_P = \frac{j_x E_x + j_y E_y}{E_x^2 + E_y^2} \quad (6.14)$$

$$\sigma_H = \frac{j_x E_y - j_y E_x}{E_x^2 + E_y^2} \quad (6.15)$$

We now look at the same profile as in Figure 6.13, but now comparing the two differently derived Pedersen and Hall conductivities. The results are shown in Figure 6.14. As expected, the values match each other almost perfectly for both conductivities, Pedersen and Hall, inside the neutral gas cloud, where the collisions occur. However, the simulation shows conductivities in the wake that are not associated with collisions. As mentioned, the currents in the wake are required to accelerate the plasma back to corotational speeds.

## 6.5. The Reference Simulation

To investigate how different mechanisms will change the simulation results, we compare the simulations with the mechanisms to the *reference simulation*, without any mechanism turned on. When not indicated otherwise, the model used in all forthcoming simulations is described in chapter 6.2. The velocity field perturbation is shown in Figure 6.15. The main Alfvén wing starts at Io at the origin and propagates towards the Jovian ionosphere. The Alfvén wave follows the characteristic that is curved due to the inhomogeneous background mass density. Along its way it gets reflected. The gradual reflection inside the torus between  $-20R_{Io} < z < 20R_{Io}$  shows no sign change in the velocity perturbation, since the alfvénic phase velocity increases. At the Jovian ionosphere  $z = \pm 60R_{Io}$  however, the reflection results in a sign change in the velocity perturbation. This produces areas of accelerated and decelerated plasma and a complex reflection pattern is formed.

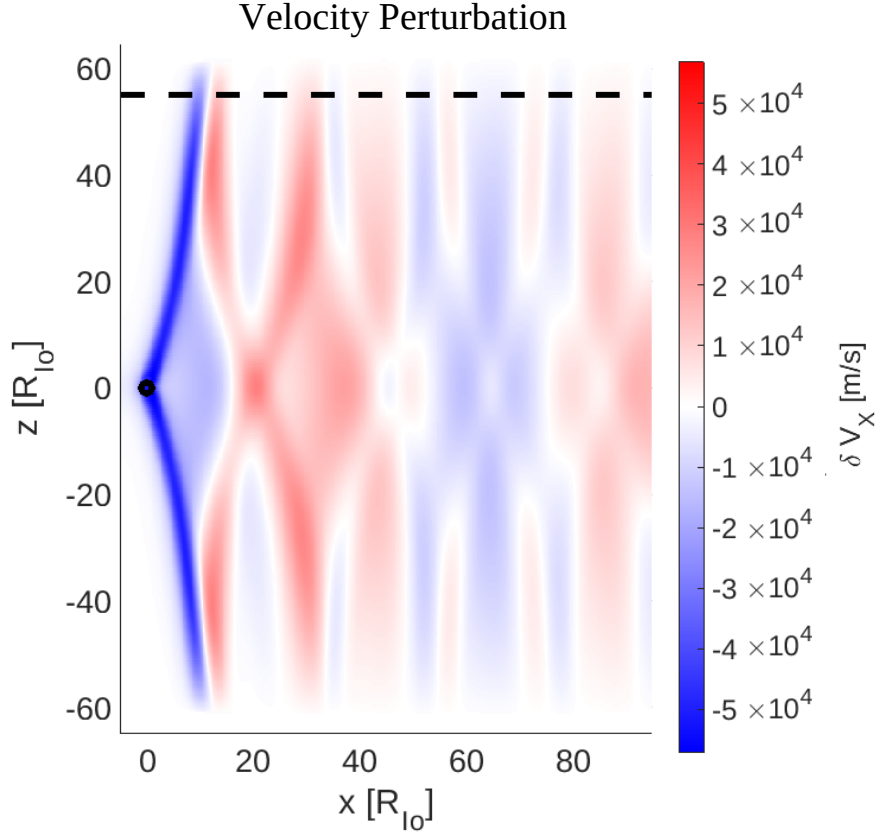


**Figure 6.15.:** The perturbations of the velocity field in x-direction in the  $y = 0$  plane. Blue colors show decelerated plasma and red colors show accelerated plasma. The strongest perturbation is in the main Alfvén wing that starts at Io at the origin and propagates towards the Jovian ionosphere at  $z = \pm 60R_{Io}$ . It gets reflected at different density gradients generating a complex reflection pattern. The black dashed line indicates the position of the analysis plane that is used to analyze the Poynting flux in the acceleration region.

The maximum deceleration of the plasma is  $\delta v_{max} \approx 5 \cdot 10^4$  m/s, which is about 88% of the flow velocity of the incoming plasma flow. This matches our expected value with a theoretical interaction strength of  $\bar{\alpha} = 0.85$ .

### 6.5.1. Reference Poynting Flux

The Alfvén wave carries its energy in the form of Poynting flux. As discussed, the Poynting flux at the acceleration region, indicated as dashed line in Figure 6.15, is used as a proxy for the energy available for wave particle interaction. Even though the direction of the Poynting flux is not associated with particle acceleration in a preferred direction, we will display the signed Poynting flux in this region to improve the distinction of certain features in the Poynting flux. The Poynting flux of the reference simulation is shown in Figure 6.16.

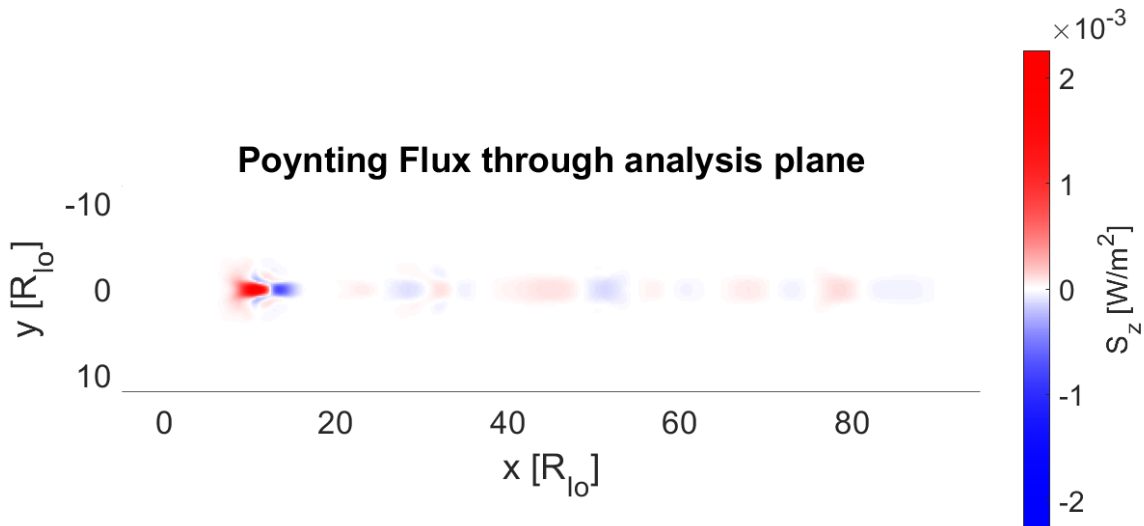


**Figure 6.16.:** Poynting flux in positive  $z$ -direction through the analysis plane at  $z = 60R_{Io}$ . Red colors show Poynting flux towards Jupiter’s northern ionosphere while blue colors show Poynting flux away from it. The symmetry between equatorward ( $y > 0$ ) and poleward ( $y < 0$ ) side is not broken in the reference simulation.

The reference Poynting flux has a peak value of  $2 \text{ mW/m}^2$ , which is about one magnitude larger than the observed emissions by Mura et al. (2018). Furthermore, we did not include the bend magnetic field lines that would converge towards Jupiter’s ionosphere, reducing the area of the footprint and increasing the power density. Not accounting for any conversion factor between Poynting flux and particle acceleration and also particle velocity and emission brightness, the available power density is sufficient to produce the observed emissions. However, the particle acceleration and subsequent emission generation is not in the scope of the simulations and the absolute values of the Poynting flux will therefore not be discussed in detail. The aim of this simulation is to investigate possible causes for the alternating structure in the observed footprint emissions. Therefore, we are mostly interested in the position and shape of the Poynting flux. In the Poynting flux of the reference simulation, we can see that we have a multitude of incoming (red) and outgoing (blue) structures of different size and intensity. However, the Poynting flux is perfectly symmetric towards the  $y = 0$  axis, since there is no symmetry breaking mechanism included yet. In the forthcoming simulation we will compare the Poynting fluxes through the same analysis plane to the one of the reference simulation.



---

Influence of the Hall Effect

---

In this part, we will discuss the influence of the Hall effect on the simulation, in particular on the Poynting flux through the analysis plane. As discussed in Chapter 4, the Hall effect is a good candidate to break the symmetry of the Alfvén wing along the x-axis. Parts of this chapter is published in Schlegel and Saur (2022).

## 7.1. Implementation of the Hall Effect

The Hall effect is implemented as a source term for the induction equation. The Hall term is the only term in the set of equations used here that depends on the number density and not on the mass density. In other words, it depends on the mass  $m$  of one particle. It can be written as:

$$\frac{\partial \mathbf{B}_{Hall}}{\partial t} = -\frac{m}{e\mu_0} \nabla \times \left( \left( \frac{\nabla \times \mathbf{B}}{\rho} \right) \times \mathbf{B} \right) \quad (7.1)$$

As it can be seen, it scales linearly with the mass. To perform a parameter study for simulations with different Hall conductances in order to investigate its effect on the simulation results, we can therefore use the particle mass  $m$  to regulate the ratio between Hall and Pedersen conductance. While the particle mass changes, the mass density  $\rho$  remains unchanged in our simulations. However, as mentioned in Section 3.5, the Pedersen conductivity is also affected on the particle mass due to its dependence on the gyrofrequency  $\Omega = eB/m$ . The Pedersen and Hall conductivities in terms of mass  $m$ , mass density  $\rho$ , magnetic field strength  $B$  and collision frequency  $\nu$  can be written as:

$$\sigma_P = \rho e^2 \frac{\nu}{m^2 \nu^2 + e^2 B^2} \quad (7.2)$$

$$\sigma_H = m \frac{\rho e}{B} \frac{\nu^2}{m^2 \nu^2 + e^2 B^2} \quad (7.3)$$

The ratio  $r_\Sigma$  between the two conductivities is always proportional to the particle mass  $m$ .

$$r_\Sigma = \frac{\Sigma_H}{\Sigma_P} = \frac{\nu}{\Omega} = m \frac{\nu}{eB} \quad (7.4)$$

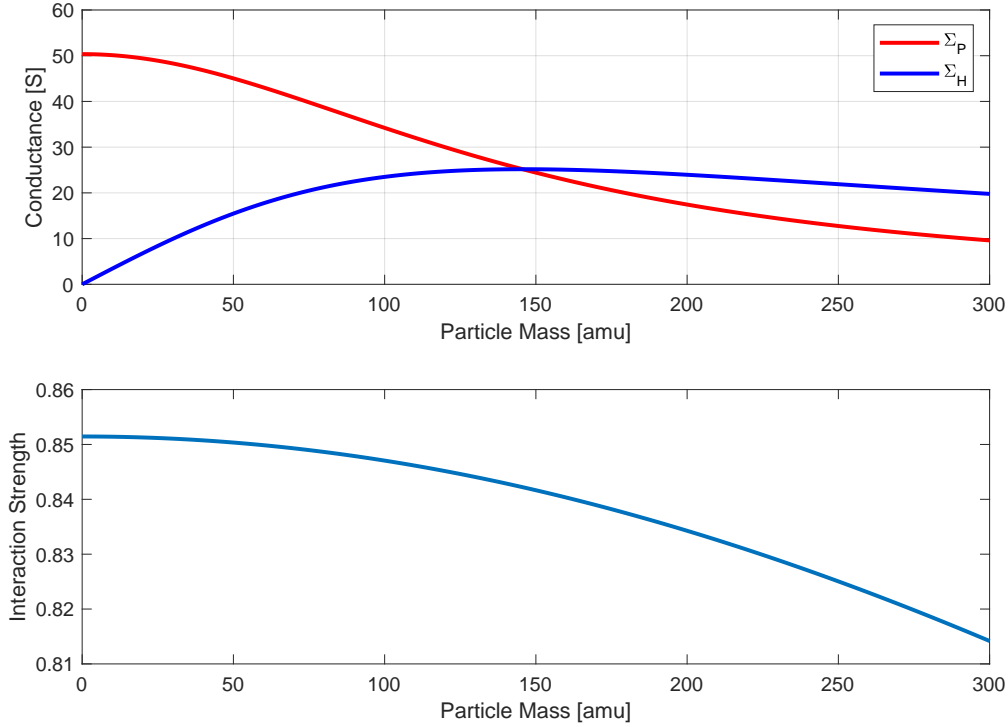


**Figure 7.1.:** The effect of particle mass. Top: The Hall (blue) and Pedersen (red) conductance for the reference simulation for different particle masses  $m$  used in the induction equation. Bottom: Calculated from the Hall and Pedersen conductance, the interaction strength does not change significantly for different particle masses.

We can see that either by increasing the collision frequency  $\nu$  or the particle mass  $m$ , we can enhance the Hall to Pedersen conductance ratio  $r_\Sigma$ . Since simulations with higher collision frequencies were numerically unstable we chose to perform simulations with different particle masses. The change in Hall and Pedersen conductance due to the change in particle mass is shown in the top plot in Figure 7.1. For plausible particle masses, i.e.  $m = 16$  amu for oxygen and  $m = 32$  amu for sulfur, the Pedersen conductance remains close to a value of  $\Sigma_P = 50$  S and with a low Hall conductance of  $\Sigma_H \leq 10$  S, the Hall to Pedersen conductance ratio is merely in the range of  $r_\Sigma \approx 0.2$ . However, the Hall conductance at Io can be expected to be similar to or even exceed the Pedersen conductance (Saur et al., 1999; Kivelson et al., 2004). To still perform simulations with  $r_\Sigma = 1$ , we used particle masses of up to  $m_{max} = 145$  amu, which does not represent any specific particle. However, this study is aimed to represent the MHD physics of the interaction for specific values of interaction strength and Hall to Pedersen conductance ratios. We can calculate interaction strength from the ratio of electric field perturbation  $\delta E$  as computed from equation (4.10) to the background electric field  $E_0$ . In the lower plot of Figure 7.1, we see that even for higher particle masses  $m$ , the interaction strength only decreases slightly. Therefore, the use of particle mass as a variable to control the ratio  $r_\Sigma$  is justified and useful.

## 7.2. Non-linear Reflection with High Hall Conductance

The non-linear reflections at different density gradients produce a complex pattern of incident, reflected and transmitted and refracted wave packages. To understand the influence of the Hall effect better, it is beneficial to not only analyze the Poynting flux through the analysis plane, but also the other corresponding fields. In this part the plasma flow velocity and magnetic field in the analysis plane as well as the current density through the plane is depicted. In the following plots, we will compare the results of the simulation without Hall effect, that is with a particle mass of  $m = 0$ , to a simulation with a Hall to Pedersen conductance ratio of  $r_{\Sigma} = 0.5$ , which corresponds to a particle mass of  $m = 72$  amu. In Figure 7.2, we see the plasma flow velocity in x-direction for both simulations. The most prominent difference is that the regions accelerated and decelerated plasma are not only longitudinally displaced, i.e. along the x-axis, but also laterally, i.e. along the y-axis. The reflections at Jupiter's ionosphere change the sign in the velocity perturbation, however not in the magnetic field perturbation since the density gradient is positive and therefore the Alfvén velocity gradient is negative. This means we often can regard regions with accelerated and decelerated plasma that are close to each other as incident and reflected Alfvén wing. In the case of a strong Hall effect, the reflected wing propagates back into the the incident Alfvén wing. Since it follows the opposite characteristics and the incoming wing changed the velocity field and magnetic field in y-direction considerably. However, without Hall effect, the y-component of the magnetic field (Figure 7.4) and the flow velocity (Figure 7.3) at the symmetry plane always vanishes. Therefore, wave packages that travel towards Jupiter on the Jupiter facing side of Io will always stay on that side and can not cross the x-z-plane. This changes with the Hall effect. As it can be seen in the two figures depicting the y-component of the two fields with activated Hall effect (bottom panels) there exist regions with non-zero values that cross the x-z-plane. The reflected Alfvén wing uses these "Alfvén bridges" and the incoming and reflected Alfvén wing are not only longitudinally displaced, but laterally as well. There are specific positions, where those crossings happen, best visible in the  $B_Y$  component (Figure 7.4, bottom) and to a lesser extend in the  $V_Y$  component (Figure 7.3, bottom). Their locations are roughly at  $x \approx 35R_{Io}$ ,  $x \approx 50R_{Io}$ ,  $x \approx 60R_{Io}$  and  $x \approx 80R_{Io}$ . We therefore expect the reflected Alfvén wing to cross the x-z-plane at those locations. This results in the velocity perturbations of a specific sign, i.e. accelerated or decelerated plasma, to be confined to one side of the x-z-plane between those locations, but can switch signs at those locations. Looking at the bottom plot of Figure 7.2, which depicts the velocity perturbation in x-direction we can confirm this hypothesis. We have continuous structures of one sign (red or blue) at each side of the x-z-plane with breaks at  $x \approx 35R_{Io}$ ,  $x \approx 60R_{Io}$  and  $x \approx 80R_{Io}$ . This symmetry plane crossing is a strong candidate to produce alternating footprints that are laterally displaced.

The magnetic field component changes sign at negative density or positive Alfvén velocity gradients. Therefore, to get a positive magnetic field perturbation in x-direction at the northern hemisphere, either the initial southern wing that already has a positive magnetic field perturbation or the Alfvén wing reflected at the torus boundary needs to be reflected at the southern Jovian ionosphere. Since the travel times to the southern ionosphere and back to northern Jovian ionosphere are at the order of  $2t_0 \approx 730$  s longer than the direct travel time to the northern ionosphere, the  $B_X$  component changes signs about every  $2t_0v_0 \approx 25R_{Io}$ . This corresponds roughly to the length of regions with one sign in the

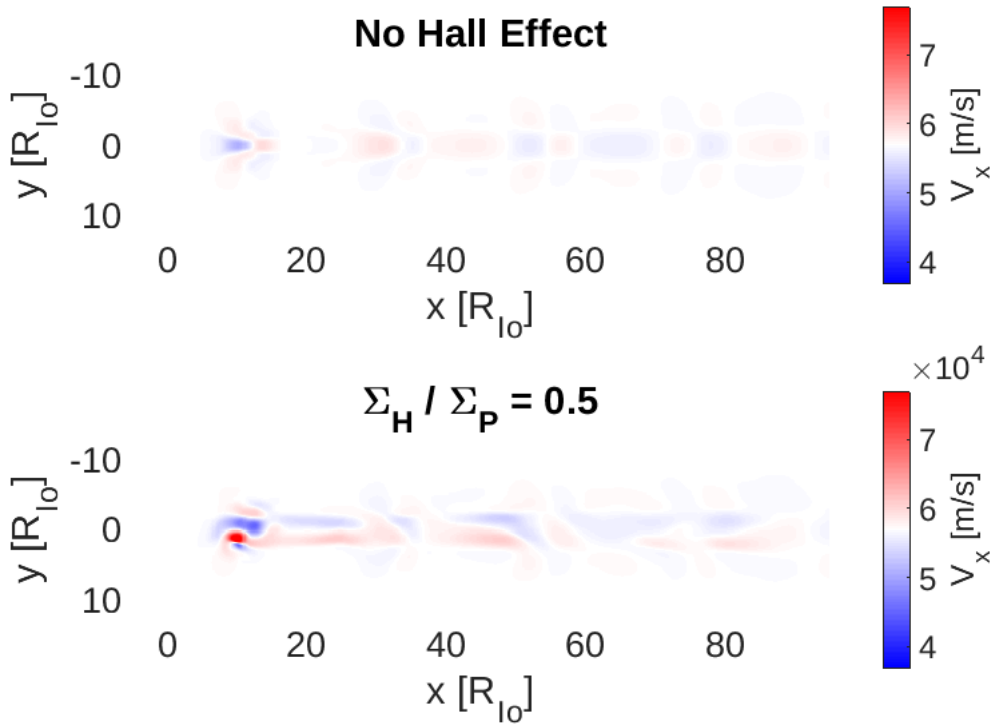


**Figure 7.2.:** Velocity perturbation in x-direction for the simulations without Hall effect (top) and with a Hall to Pedersen conductance ratio of  $r_\Sigma = 0.5$ . The blue regions show decelerated plasma, while the red regions correspond to accelerated plasma. The Hall effect creates laterally displaced regions.

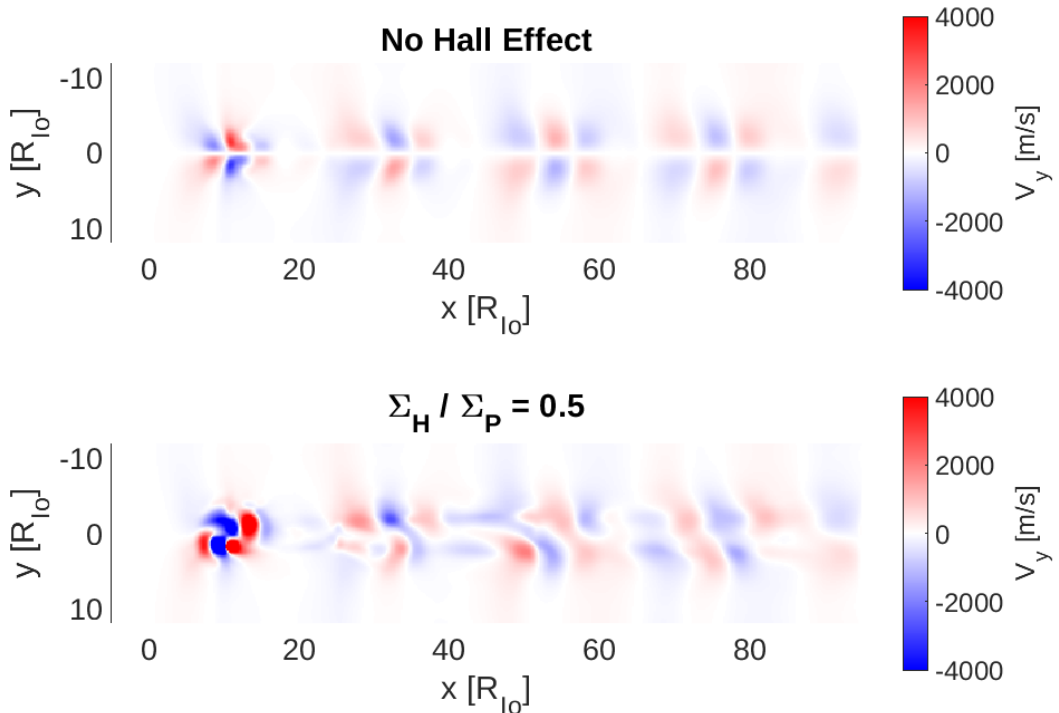


**Figure 7.3.:** Velocity perturbation in y-direction for the simulations without Hall effect (top) and with a Hall to Pedersen conductance ratio of  $r_\Sigma = 0.5$ . The Hall effect breaks the symmetry between Jupiter facing / equatorward side and anti-Jovian / poleward side.

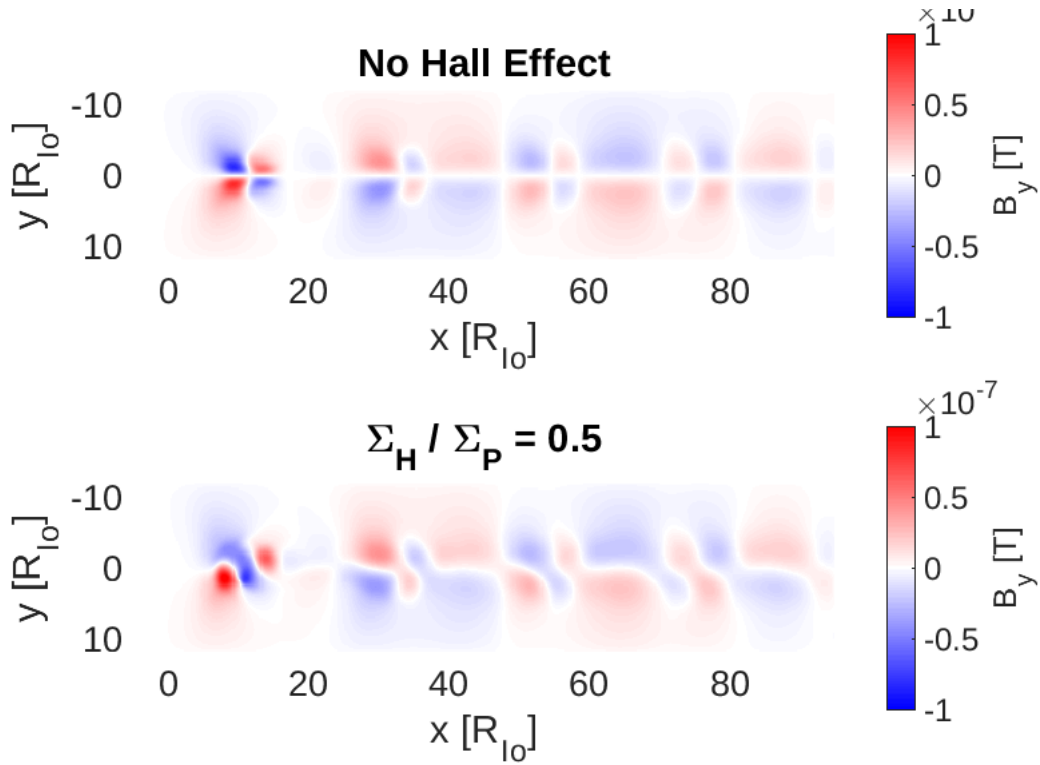


**Figure 7.4.:** Magnetic field perturbation in  $y$ -direction for the simulations without Hall effect (top) and with a Hall to Pedersen conductance ratio of  $r_{\Sigma} = 0.5$ . The Hall effect creates regions of  $B_Y \neq 0$  at the  $x$ - $z$ -plane.

$B_X$  perturbation shown in Figure 7.5. Since contrary to the velocity component, we have larger homogeneous areas due to its different reflection behaviour, the Hall effect does not change the  $\mathbf{B}$  components significantly in the analysis plane.

This is also represented in the current density perpendicular to the analysis plane. Similar to the magnetic field, the current direction changes sign at the reflections at the torus boundary. For the initial Alfvén wing the current is always directed towards Io at the Jupiter-facing side, that is  $j_z(y > 0) < 0$  at the northern wing and  $j_z(y > 0) > 0$  at the southern wing. The current density in the analysis plane is shown in Figure 7.6. We can see the lateral separation of currents towards Jupiter (red) and away from Jupiter (blue) already in the simulation without Hall effect. The position and effective size does not change with activated Hall effect significantly.

We have seen that the Hall effect builds Alfvén bridges in the  $V_Y$  and especially the  $B_Y$  component that is used by the reflected Alfvén wing to cross the  $x$ - $z$ -plane. Since the velocity field and therefore the Poynting flux changes sign at the reflection at the Jovian ionosphere, this creates laterally displaced regions that are separated in the velocity field. In the next section we will see how this translates to the Poynting flux.

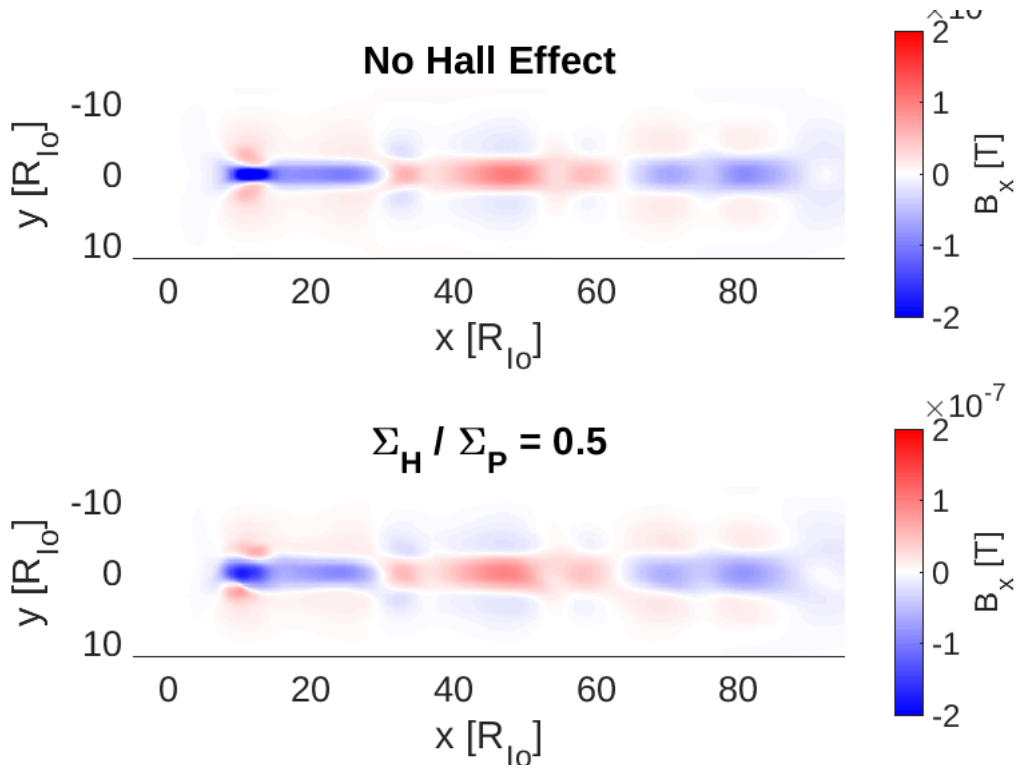


**Figure 7.5.:** Magnetic field perturbation in x-direction for the simulations without Hall effect (top) and with a Hall to Pedersen conductance ratio of  $r_{\Sigma} = 0.5$ . The different reflection behaviour of the magnetic field results in large regions with positive or negative  $B_x$  perturbations.

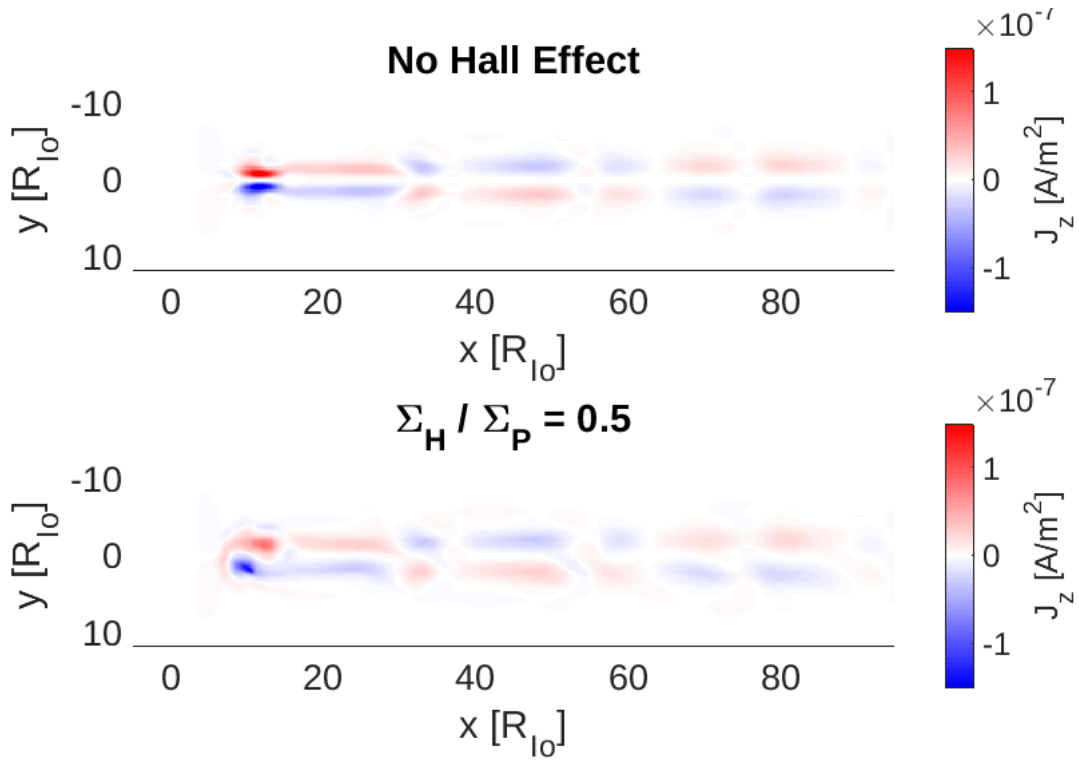


**Figure 7.6.:** Current density in z-direction for the simulations without Hall effect (top) and with a Hall to Pedersen conductance ratio of  $r_{\Sigma} = 0.5$ . The currents are only slightly changed by the Hall effect.

### 7.3. Poynting Flux with Hall Conductance

To investigate the Hall effect in more detail, we chose three different Hall to Pedersen conductance ratios  $r_\Sigma = 0, 0.15, 1$ , corresponding to a particle mass of  $m = 0, 22, 145$  amu, respectively. The resulting Poynting fluxes through the analysis plane are shown in Figure 7.7. The Poynting flux contains structures similar to the ones seen in the velocity perturbation in x-direction. This can be understood if we look how the Poynting flux is calculated. We will neglect the Hall term for the electric field for this derivation, therefore  $\mathbf{E} = -\mathbf{v} \times \mathbf{B}$ . Furthermore, the perturbation of the velocity in z-direction can be neglected. For a more thorough derivation of the Poynting flux, see appendix B.4. In the rest frame of the plasma, where the background values for  $B_{X,0} = B_{Y,0} = v_{X,0} = v_{Y,0} = 0$ , the Poynting flux in z-direction can be approximated by

$$S_Z \approx -\frac{B_0}{\mu_0} (v_X B_X + v_Y B_Y). \quad (7.5)$$

Comparing Figures 7.2 and 7.3, the velocity perturbation in x-direction is about one order of magnitude larger than the ones in y-direction. Similarly, the magnetic field perturbation in x-direction are about twice as large as those in y-direction as seen when comparing Figures 7.5 and 7.4. This means, that the first term in equation 7.5 is much larger than the second. Since  $B_X$  is much more homogeneous than  $v_X$ , the substructures in the Poynting flux in z-direction are mainly due to the variability of  $v_X$ .

Therefore, also in the Poynting flux we see the lateral displacement of the structures, similar to the velocity field. One interesting thing to note is the increased intensity of the secondary structures down the tail for higher ratios  $r_\Sigma$ . Higher Hall conductances increase the field strength in y-direction for both, velocity field and magnetic field. This increases the separation of incident and reflected Alfvén wing and the diminishing effect due to negative interference is reduced. This also results in the structures begin more separated and generally larger in latitudinal (y-) direction. This produces patterns that resemble latitudinal displaced maxima. Depending on the strength of the Hall effect, the displacement varies from purely longitudinally displaced ( $r_\Sigma = 0$ ) to almost perfectly latitudinal displacement ( $r_\Sigma = 1$ ). Therefore, the alternating displacement in the alternating Alfvén spot street as seen in the observations by Mura et al. (2018) and Moirano et al. (2021) can be produced by high Hall conductances, comparable to the Pedersen conductance. In a next step, we will look into the position of the maxima. For that purpose, the positions of the 4 most distinct pairs of maxima besides the MAW for the simulations with  $r_\Sigma = 0.15, 1$  have been investigated regarding their separation distance. The four pairs and their separation are shown in Figure 7.8. A separation of  $1R_{Io}$  along the x-axis corresponds to roughly  $0.25^\circ$  in longitude in the Jovian ionosphere, while a separation of  $1R_{Io}$  along the y-axis corresponds to about  $0.13^\circ$  in latitude in the Jovian ionosphere. The difference is due to the elongation of the footprints due to the converging magnetic field lines, which is not implemented in the model. The longitudinal and latitudinal separations are shown in Table 7.1. While the longitudinal separation decreases for all pairs of footprint by about  $0.7^\circ$  when increasing the Hall to Pedersen conductance ratio from  $r_\Sigma = 0.15$  to  $r_\Sigma = 1$ , the latitudinal separation increases by about  $0.1^\circ$ . However, due to the simplified geometry of the system especially the magnetic field, the values obtained in this study are not easily comparable to the observations. Mura et al. (2018) reported a separation of the features of  $\approx 350$  km, which translates to an longitudinal separation of

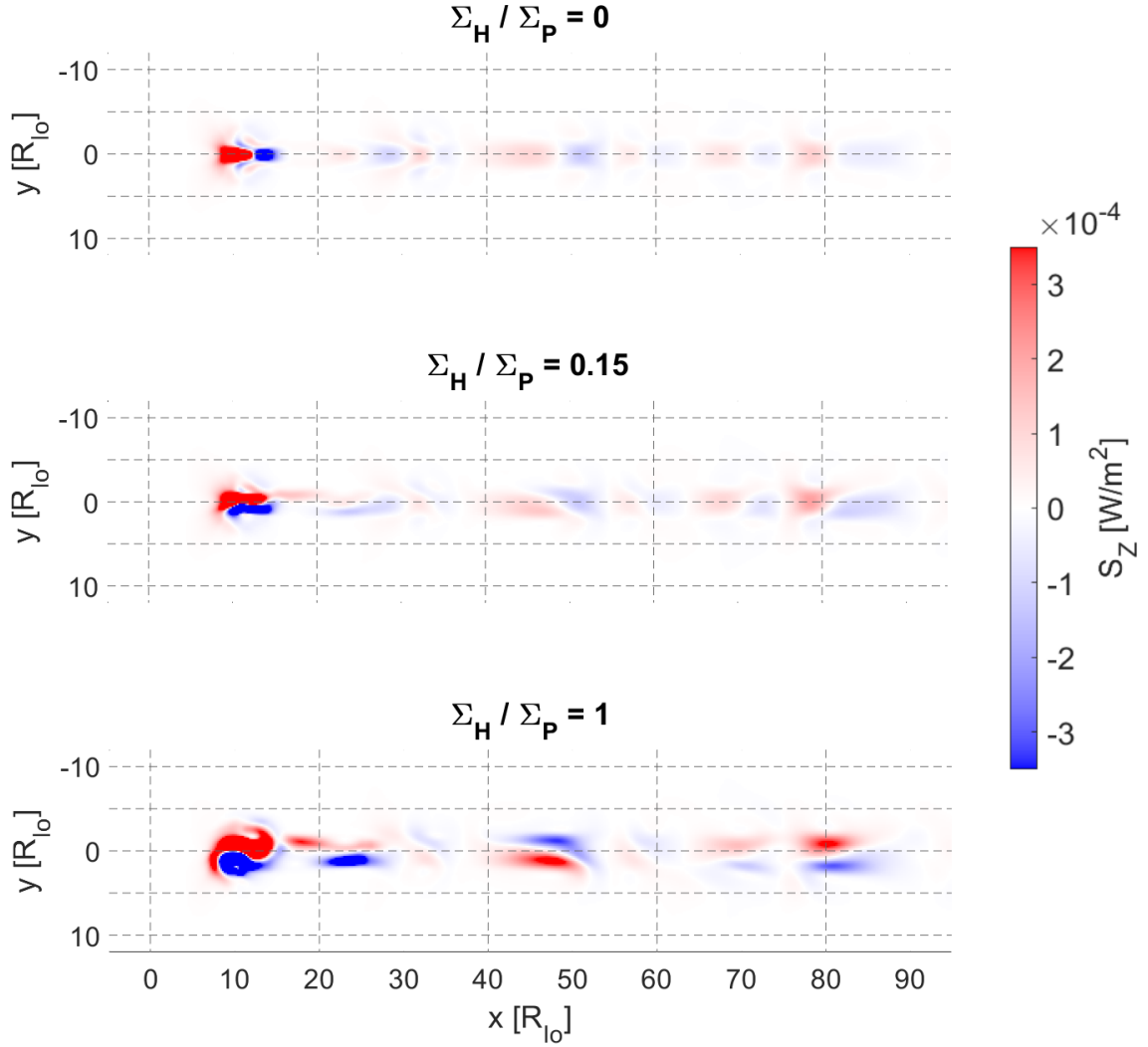


**Figure 7.7.:** Poynting flux through the analysis plane for Hall to Pedersen conductance ratios of  $r_\Sigma = 0$  (top), 0.15 (center) and 1 (bottom). The color bar has been adjusted to highlight features in the tail region. The maxima of the Poynting flux are laterally displaced and incoming and reflected Poynting fluxes are alternatingly displaced in positive (equatorward) and negative (poleward)  $y$  direction.

$\approx 0.7^\circ$ . They also reported an average latitudinal displacement of the spots of  $\approx 200$  km. This corresponds to a latitudinal separation of  $\approx 0.33^\circ$ . Both of these values would be in line with some of the longitudinal separations in the simulation with the higher Hall conductance.

The Hall effect is a promising mechanism to create alternatingly laterally displaced Poynting flux maxima in the acceleration region, that would translate to a pattern similar to the observed alternating Alfvén spot street. Crucial for the displacement is not only a strong Hall effect with a high Hall to Pedersen conductance ratio  $r_\Sigma$ , but also non-linear reflections at Jupiter’s ionosphere. This means that the interaction strength  $\bar{\alpha}$  needs to be high enough for the reflection to be considered non-linear. Furthermore, even though the gradual reflections at the torus boundary add complexity to the pattern and allow closer distances between the Poynting flux maxima in the tail, they are not essential for the development of alternating spots. Therefore, the torus is no necessary condition for the alternating Alfvén spot street and the footprint of other moons can theoretically also

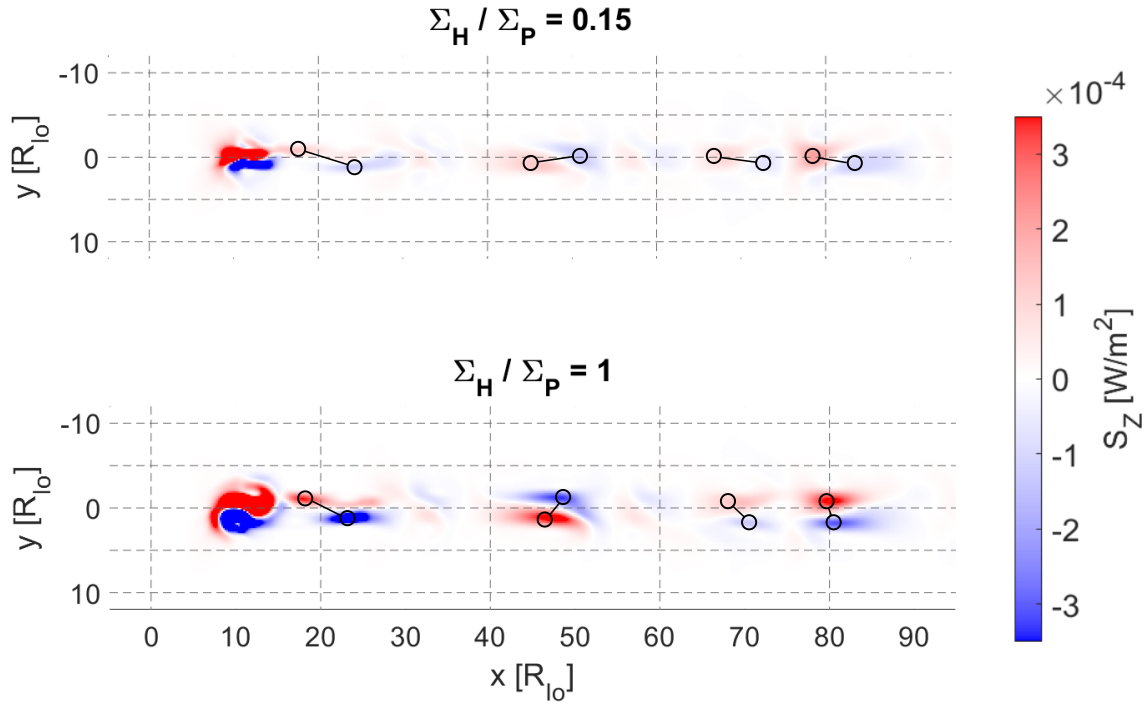


**Figure 7.8.:** Poynting flux through the analysis plane for a Hall to Pedersen conductance ratio of  $r_\Sigma = 0.15$  (top) and  $r_\Sigma = 1$  (bottom). The circles indicate the four largest maxima and minima outside the Poynting flux of the main Alfvén wing. The maxima of the incoming Alfvén waves are connected to the corresponding minima of the reflected Alfvén wave. With higher Hall to Pedersen conductance ratios, separations between maxima and minima shift from almost entirely longitudinal (x-direction) to more and more latitudinal (y-direction).

**Table 7.1.:** Lateral and Longitudinal Separation of Maxima

X-Position of First Maximum	Longitudinal Separation	Latitudinal Separation
$x = 17R_{Io} (r_\Sigma = 0.15)$	$8.1R_{Io} / 2.04^\circ$	$2.8R_{Io} / 0.38^\circ$
$x = 46R_{Io} (r_\Sigma = 0.15)$	$4.9R_{Io} / 1.24^\circ$	$1.7R_{Io} / 0.23^\circ$
$x = 66R_{Io} (r_\Sigma = 0.15)$	$5.2R_{Io} / 1.31^\circ$	$1.4R_{Io} / 0.19^\circ$
$x = 78R_{Io} (r_\Sigma = 0.15)$	$4.3R_{Io} / 1.09^\circ$	$1.3R_{Io} / 0.17^\circ$
$x = 17R_{Io} (r_\Sigma = 1)$	$6.2R_{Io} / 1.57^\circ$	$3.5R_{Io} / 0.47^\circ$
$x = 46R_{Io} (r_\Sigma = 1)$	$2.1R_{Io} / 0.53^\circ$	$2.7R_{Io} / 0.37^\circ$
$x = 66R_{Io} (r_\Sigma = 1)$	$2.5R_{Io} / 0.63^\circ$	$2.6R_{Io} / 0.35^\circ$
$x = 78R_{Io} (r_\Sigma = 1)$	$0.8R_{Io} / 0.20^\circ$	$2.9R_{Io} / 0.39^\circ$

develop alternating spots. For Europa, modelling suggests a Pedersen conductance of  $\Sigma_{P,E} = 30$  S and a Hall conductance of  $\Sigma_{H,E} = 10$  S Saur et al. (1998) and the interaction could still be strong enough to allow non-linear reflections at the Jovian ionosphere. Even though Paranicas et al. (1998) suggest lower conductance numbers, the footprint of Europa could also be a candidate for alternating tail spots due to the Hall effect, even though to a lesser extent than observed at the Io footprint. For Ganymede, the interaction is different and the main obstacle for the plasma is not the conducting ionosphere, but Ganymede's magnetosphere. The integrated Hall and Pedersen conductances along the magnetic field lines are small and not considered the driver of the interaction. Therefore, we can rule out symmetry breaking of the Ganymede footprint due to the Hall effect.

---

## Further Mechanisms

---

Even though the Hall effect seems to be a promising mechanism to break the symmetry in the footprint tail and generate the alternating patterns observed, other mechanisms are investigated that could produce similar results. In the first section, we are interested in the influence of the magnetic field, that is, how the real magnetic field would change the resulting Poynting flux pattern. The change from a homogeneous background field to the complex Jovian magnetic field can affect the morphology and location of the footprints in two ways. First, the magnetic field lines are not homogeneously shaped and the characteristics of the Alfvén wing are therefore more complex. This on the one hand changes the position on the footprints as already discussed in Chapter 5, stretching and compressing the distance of secondary spots. On the other hand the shape of the footprints is affected. The dipole field alone already stretches the footprint by almost a factor of 2, since the magnetic field lines converge faster latitudinally than longitudinally. Second, the different path lengths of the field lines and magnetic field strength along them change the travel time along those field lines. Differences in travel time of Alfvén wave packages change the relative position of Io and the corresponding footprint emissions. Implementing the real multi-pole magnetic field of Jupiter and switching to a spherical or dipole coordinate system with Jupiter in the center is beyond the scope of this work. Therefore, we are interested in the effect of travel time difference on the location and shape of the secondary spots. In the second section of this chapter, we will analyze the influence of an asymmetric atmosphere. Due to solar insolation, leading/trailing side asymmetries and patchy volcanic out-gassing, the ionosphere of Io and therefore its conductance is asymmetric. Parts of this chapter have been submitted to JGR-Space Physics and have been accepted for publication.

### 8.1. Travel Time Difference

The waves that are generated at Io propagate along the magnetic field lines towards Jupiter's ionosphere. Depending on the specific field line the wave's travel path has a specific total length and the wave velocity along this path varies. Waves starting from

the anti-Jovian side generally have a longer travel path than waves starting from the sub-Jovian side of Io as sketched in Figure 8.1. In particular, the longer travel path of these waves result in the wave propagating through the dense torus region longer, where the Alfvén velocity  $v_A$  is much higher. Especially, the time the wave is inside this region determines the overall travel time  $t$  of the wave towards the Jovian ionosphere

$$t = \int_{Io}^{Jupiter} \frac{1}{v_A(\rho, B)} ds \quad (8.1)$$

along the travel path segments  $ds$ . Since the travel path depends on the magnetic field strength  $B$  and the Alfvén velocity depends on the density  $\rho$  and the magnetic field strength  $B$ , the travel time is determined by the chosen magnetic field model and the density model. For this purpose we used the JRM09 magnetic field model by Connerney et al. (2018) and the torus density model by Dougherty et al. (2017). The mapping along the field lines has been done as described in Chapter 5. The magnetic field model strongly varies azimuthally, because on the one hand, the dipole is tilted against the ecliptic and on the other hand, higher moments play an important role especially close to the Jovian ionosphere. The torus model, though here not on itself azimuthally dependent, also varies with longitude since the torus is in the centrifugal equatorial plane and therefore tilted with respect to the ecliptic. Therefore, the position of Io varies within the torus and the density model and hence also the Alfvén velocity along the field is different for each longitudinal position of Io. Thus, the travel time difference strongly depends on Io's position, the used magnetic field model and the density model. For the used models, Figure 8.2 shows the total travel times to the northern Jovian ionosphere for each position of Io and the calculated travel time difference between waves starting from the anti-Jovian and sub-Jovian side. The study yields similar results as the travel times calculated by Hinton et al. (2019). As expected, the travel time difference is at maximum, when the total travel time is maximal. This is when Io is closest to the southern edge of the torus. Since the dipole is tilted towards  $196.6^\circ$  western longitude Connerney et al. (2018) or  $163.4^\circ$  eastern longitude, the maximum is roughly at the opposing side, i.e.  $343.4^\circ$  eastern longitude. The corresponding maximum travel time difference from our model is  $t_{max} = 3.7$  s.

### 8.1.1. Implementation and Simulation

In Jupiter's magnetosphere, the travel time difference is a result of curved magnetic field lines and inhomogeneous density. To comply with the simplified geometry in our model with the homogeneous background magnetic field, we have two options to vary the travel time. First, we can change the travel path distance by tilting the analysis plane and the position of the ionosphere depending on the  $y$ -coordinate. Second, we can vary the Alfvén velocity via altering the mass density. In this work, the second method was used, since it proved to be numerically more stable. To change the travel times according to the modelling results, a gradient  $\lambda_y$  in density along the  $y$ -direction is implemented. The density model is altered according to

$$\rho(y, z) = \rho(z)(1 + \lambda_y y) \quad (8.2)$$

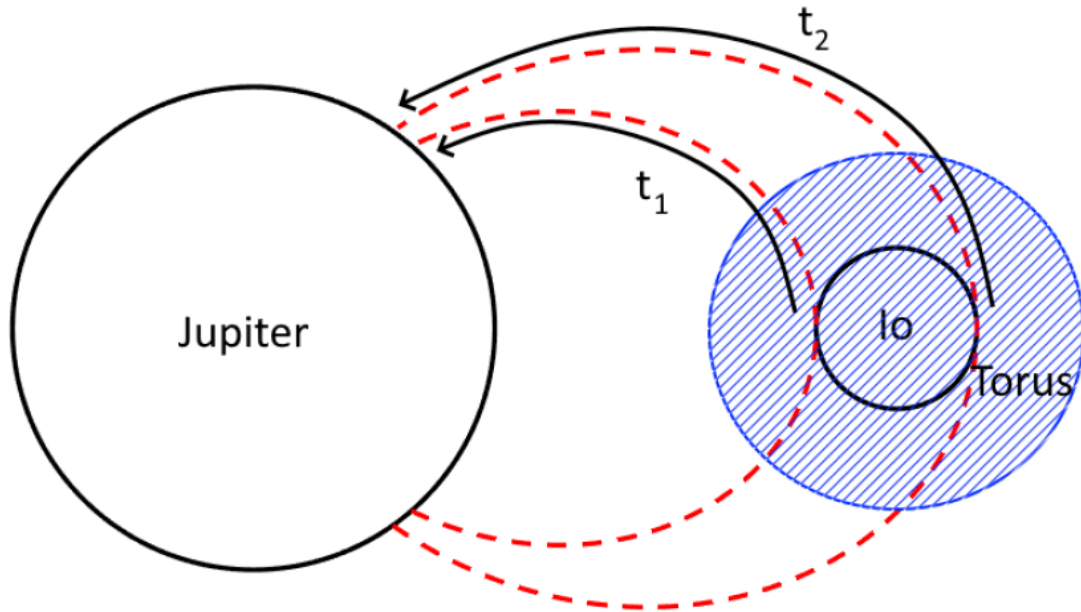


**Figure 8.1.:** Sketch of the travel path for the Alfvén waves starting from the anti-Jovian and sub-Jovian side of Io. Jupiter’s dipole field lines (red dashed) connect to both sides of Io with different path lengths. The waves starting from the anti-Jovian side generally have a longer path length, especially inside the torus (blue shaded area) resulting in a larger travel time  $t_2 > t_1$ . Distances and sizes are not to scale in this sketch.

To acquire a travel time difference of  $\delta t = 3.7$  s, we chose a mass density gradient of  $\lambda_y = 0.01/R_{Io}$ . The resulting travel times for different positions on the y-coordinate are thus

$$t(y) = t_0 \sqrt{1 + \lambda_y y} \approx t_0 \left( 1 + \frac{\lambda_y}{2} y \right). \quad (8.3)$$

For the Jovian side of Io at  $y = -1R_{Io}$  and its opposite side at  $y = 1R_{Io}$ , this results in a travel time difference of  $\delta t = 3.65$  s. The results of the simulation with and without travel time difference are shown in Figure 8.3. It is to be noted, that even though the maximum travel time difference occurs, when Io is at the edge of the torus, all simulations were run with Io at the center. We do not aim to recreate the observations but to isolate the effects that different mechanisms have on the structure, morphology and location of the Poynting flux and therefore on the emission pattern. Therefore, implementing the maximum travel time difference for a simulation with Io at the torus center is sufficient. Comparing the two simulations, we can directly see that the Poynting flux corresponding to the MAW footprint at  $x \approx 10R_{Io}$  is strongly tilted since the part of the Alfvén wing starting from the anti-Jovian side arrive later at the analysis plane. If we look at the structures at  $y = \pm 1R_{Io}$  and compare them to the simulations with no travel time difference implemented, we see a longitudinal displacement of roughly  $\delta x = 0.1R_{Io}$ , which is close to the expected value of  $\delta x = 3.7 \text{ s} \cdot 57000 \text{ km/s} = 0.12R_{Io}$ . Since the Alfvén wing itself is larger than the obstacle, the travel time difference has an even stronger effect to the structures that are laterally more displaced. At the MAW, the effect however is minor, tilting the structure only slightly. With multiple reflections down the tail, the travel time difference adds up. Generally speaking the longitudinal offset between equatorward and poleward side is about  $\lambda_y$  of the total travel distance down the tail. Therefore, at

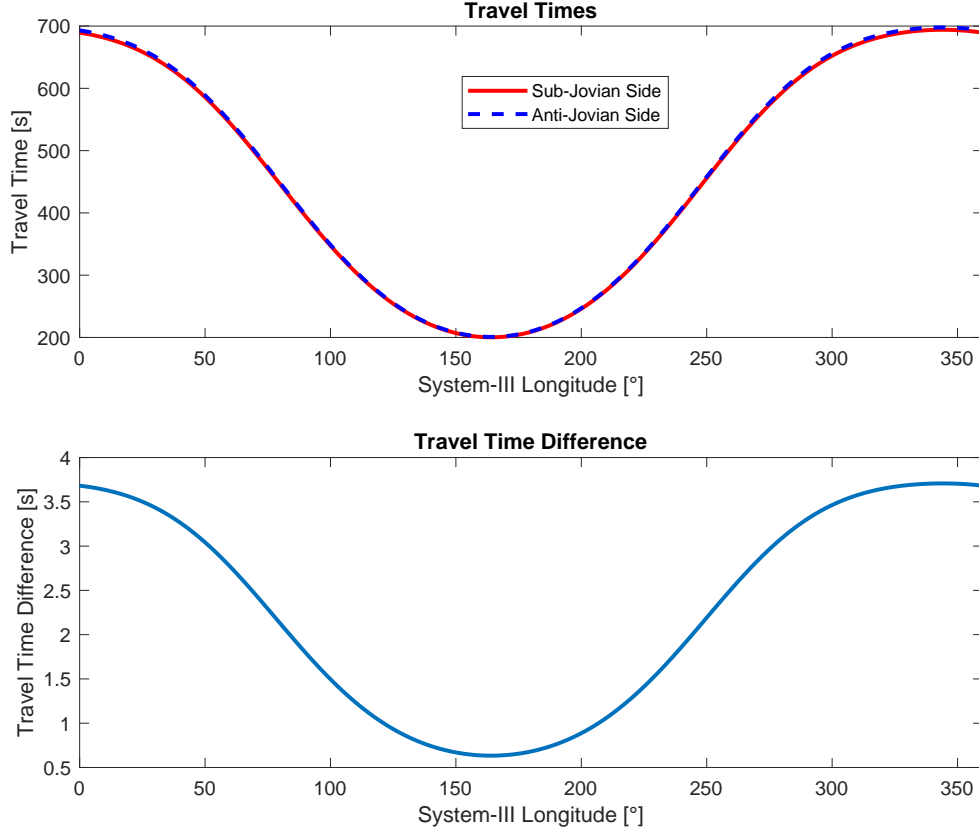


**Figure 8.2.:** Top: Calculated travel times from the JRM09 and used density model for the sub-Jovian side (red) and the opposite side (blue). Bottom: Even though the travel times are similar to each other, the travel time difference depends on Io’s position, with a maximum travel time difference of  $\delta t = 3.7$  s, when Io is close to the southern edge of the torus.

higher distances from the MAW, the Poynting flux gets more and more distorted due to this effect and asymmetries are more apparent. The observations of Mura et al. (2018) and Moirano et al. (2021) however show alternating structures directly downstream the MAW emission, which can not be seen in the simulations. Furthermore, even though the simulations show strong symmetry breaking effects, the pattern is more chaotic and does not directly show alternating structures. Therefore, we rule out the travel time difference as main mechanism to create the observed structures. However, it can be a contributing effect that increases the asymmetry down the tail.

To verify this hypothesis, we conducted a study with activated Hall effect and travel time difference for the two Hall to Pedersen conductance ratios of  $r_{\Sigma} = 0.15$  and  $r_{\Sigma} = 1$ . The simulation results are shown in Figure 8.4. We can compare them now to the simulations without travel time difference as shown in the previous chapter in Figure 7.7. Like for the simulations without the Hall effect, the differences are not significant at or near the MAW. Yet, for both Hall to Pedersen conductance ratios  $r_{\Sigma}$ , the simulation near the MAW already shows strongly laterally displaced maxima. Further downstream, the difference due to the travel time difference become more apparent. In the case of the intermediate Hall conductance with  $r_{\Sigma} = 0.15$ , both the Hall effect and the travel time difference attribute to the asymmetries in the Poynting flux in the tail and enhance the development of alternating maxima. Whereas the latitudinal separation in the simulation

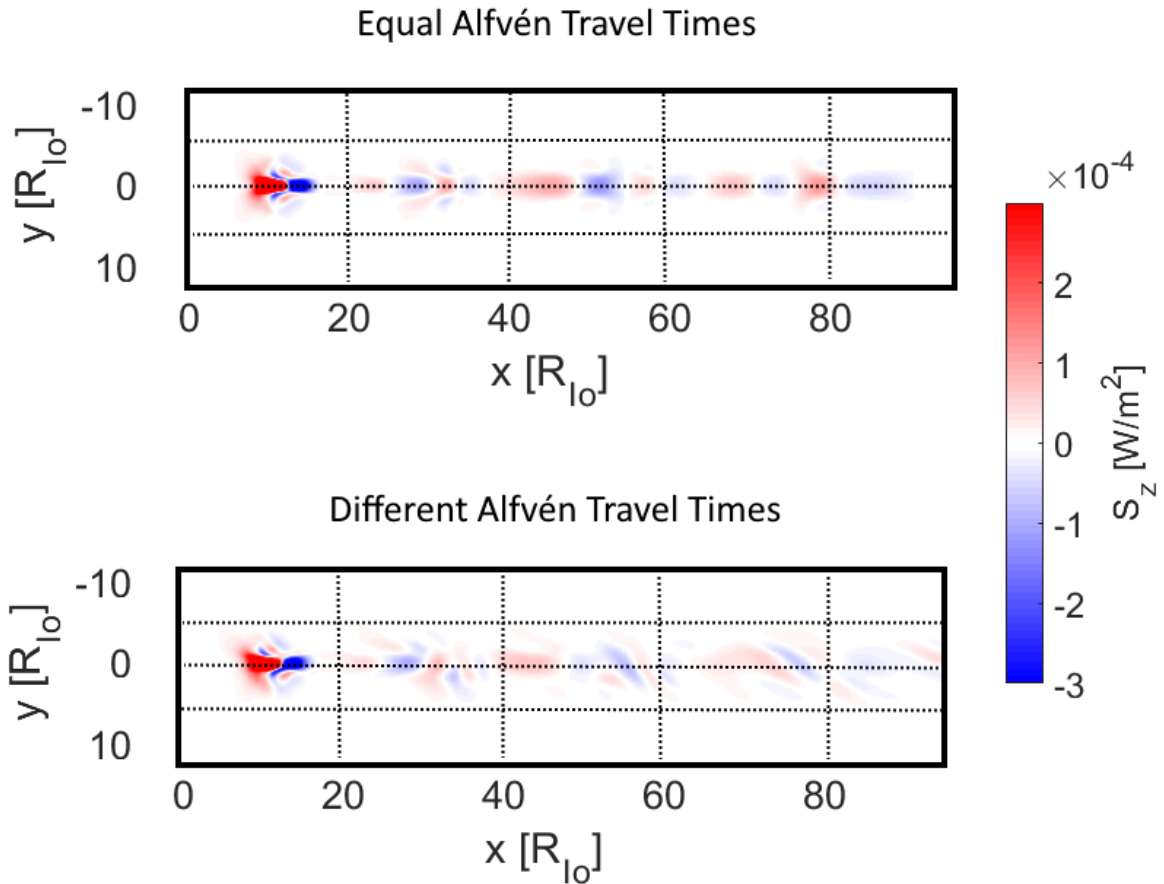


**Figure 8.3.:** Poynting flux through the analysis plane of simulations without (top) and with (bottom) travel time difference. The Poynting flux at the MAW is longitudinally displaced at the flanks according to the travel time difference between Jupiter facing and opposite side. The travel time difference accumulates down the tail, increasing the asymmetry.

with only the Hall effect is very small, e.g. at  $x = 40R_{Io}$ , it increases when the travel time difference is implemented. Furthermore the number of distinct extrema increases and generally the pattern gets more chaotic in the tail. In the case with a high Hall conductance with  $r_{\Sigma} = 1$ , the lateral displacement of the Poynting flux maxima is already well developed. The travel time difference here has only a minor effect and is not needed for the development of the alternating Alfvén spot street.

The main driver of the travel time difference is the slow propagation of Alfvén waves inside the plasma torus. At Europa, where the mass density is about a factor of 10 lower Bagenal and Dols (2020), the travel time difference does not reach the same value as for Io and therefore has a reduced effect on developing asymmetries in the tail. As for Ganymede, which is larger in cross section but even further outside, we do not expect the travel time difference to have a major effect on the morphology of the footprints.

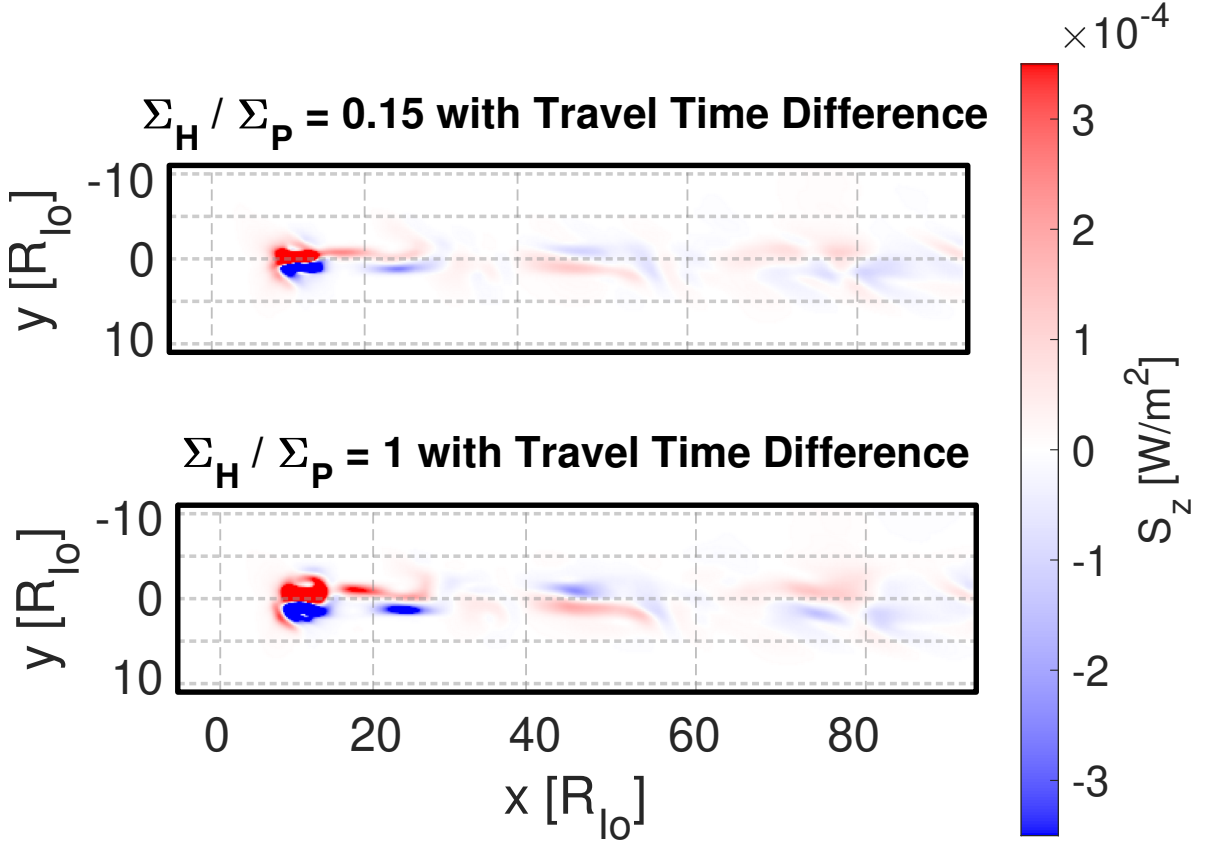


**Figure 8.4.:** Poynting flux through the analysis plane for simulations with a travel time difference of  $\delta t = 3.7$  s and with activated Hall effect for a Hall to Pedersen conductance ratio of  $r_\Sigma = 0.15$  (top) and  $r_\Sigma = 1$  (bottom). Compared to the Hall-simulations without travel time difference (Figure 7.7), the asymmetries down the tail increases.

## 8.2. Asymmetric Atmosphere

Until now, Io has been implemented as a neutral gas cloud with homogeneous density in the inside and an exponential radial decrease in density outside. Since we want to match the Pedersen and Hall conductances of the obstacle, this representation is generally not ideal. On the one hand are the conductances increased at the border of Io, since the integration length through the conducting ionosphere is larger. On the other hand is Io's ionosphere not radially symmetric but is increased at the day side due to higher sublimation rates and decreased at the poles. Furthermore, the anti-Jovian side of the atmosphere is denser and more extended than the sub-Jovian side Feaga et al. (2009). Lastly, the volcanic out-gassing can create transient local atmospheric enhancements. The new neutral gas cloud model representing Io is shown in Figure 8.5 in terms of ratio between Pedersen and Alfvén conductance. Since the interaction strength  $\bar{\alpha}$  is a global value representing the whole interaction, it can not be used to represent local inhomogeneities. However, with the ratio between Pedersen and Hall conductance, we can estimate the relative deceleration of the plasma for different areas of the Alfvén wing. We will estimate this value as

$$\frac{\delta v}{v}(x, y) = \frac{\Sigma_P(x, y)/\Sigma_A}{2 + \Sigma_P(x, y)/\Sigma_A}. \quad (8.4)$$

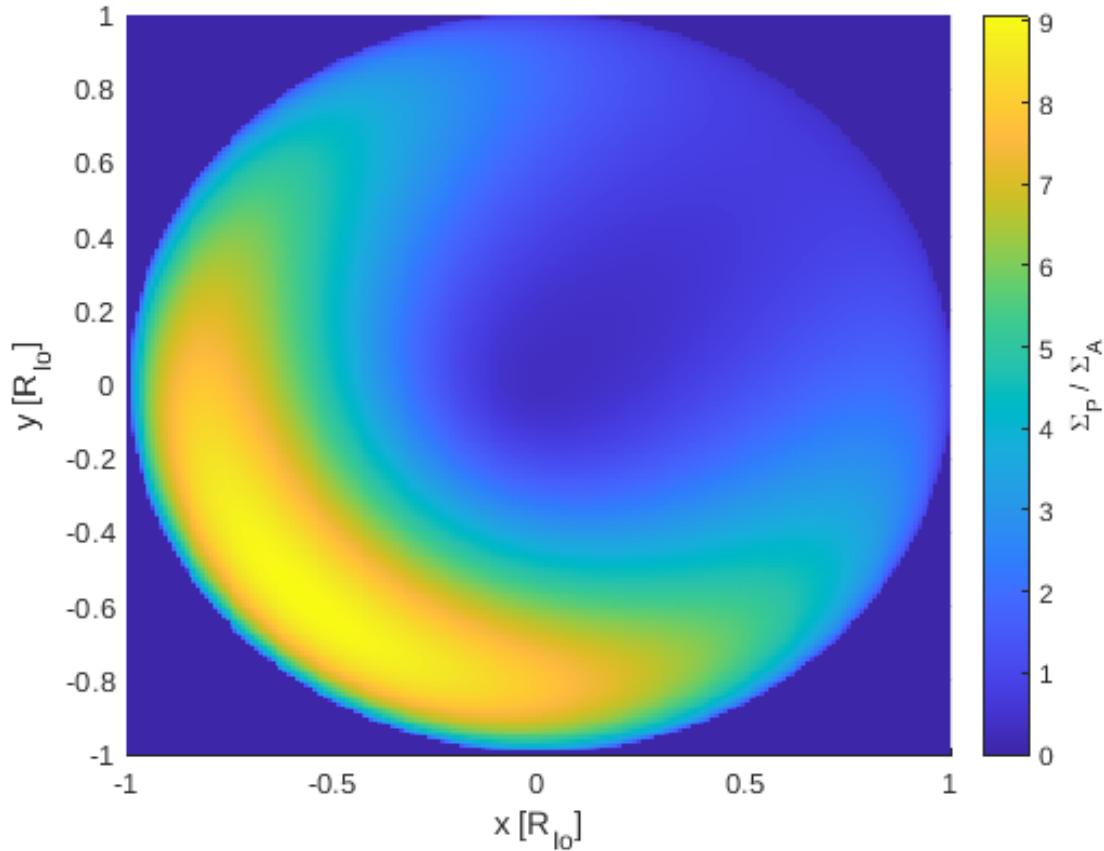


**Figure 8.5.:** The ratio of Pedersen to Alfvén conductance ( $\Sigma_A = 4.3$  S) of the asymmetric atmosphere model. The neutral gas density and therefore the Pedersen conductance  $\Sigma_P$  is enhanced at the sub-solar point at  $(-0.5, -0.5)$  and decreased at the opposite side. Due to the lowest density and the shortest integration path, the Pedersen conductance is lowest at the poles.

This results in a high interaction strength at the sub-solar point of  $\delta v/v \approx 0.8$ , which would be high enough to allow non-linear reflections. At the locations with the lowest Pedersen conductance, which is at the night side and at the poles of Io, the relative deceleration is expected only to be about  $\delta v/v \approx 0.2$ . This value is fairly low and the reflections at the sub-Jovian side ( $y > 0$ ) can be treated as linear in this model. The non-linearity of the reflections play an important role in creating the reflection pattern and the corresponding Poynting flux morphology. We therefore would expect an asymmetry between Jupiter-facing and the opposite side of Io, which should translate to asymmetries in the Poynting flux through the analysis plane.

### 8.2.1. Simulation with an Asymmetric Atmosphere

In Figure 8.6, we see the comparison between the simulation with a radially symmetric atmosphere and the one with an asymmetric atmosphere in the Poynting flux through the analysis plane. The main difference here seems to be a shift of the entirety of the Poynting flux in upstream direction and towards the anti-Jovian side. This shift is expected since the maximum of the Pedersen conductance is not centered anymore, but similarly shifted to the upstream anti-Jovian side. Furthermore the structures are decreased in size and intensity which results from the overall smaller size of the region with high Pedersen

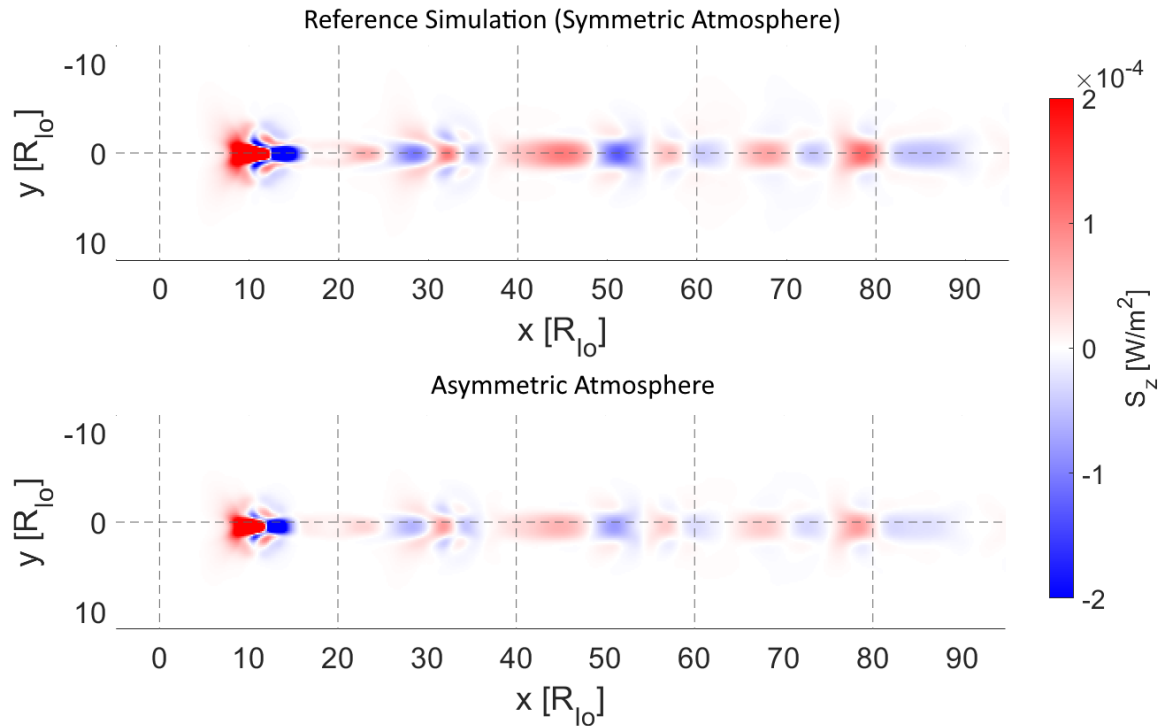


**Figure 8.6.:** Poynting flux through the analysis plane for the simulation with a radially symmetric atmosphere (top) and an asymmetric atmosphere as described in Figure 8.5 (bottom).

conductance. However, the morphology of the structures are generally unchanged and only small asymmetries in the Poynting flux are visible. Even with this very strong contrast in Pedersen to Alfvén conductance ratio in the atmospheric model, the atmospheric structure fails to alter the Poynting flux significantly. A general higher Pedersen conductance will not change this result, since the interaction strength gets saturated and the contrast diminishes.

We can therefore rule out the asymmetries in Io’s atmosphere as a mechanism to create the alternating patterns that were observed. Since even with one of the strongest contrasts possible, the effect seems minor, we also do not expect this mechanism to be of importance for the other Galilean moons.

The recent observations of the Io footprint of Mura et al. (2018) and Moirano et al. (2021) posed some questions on the generation of the structures in the foot print tail. The AASS break the symmetry between the equatorwards and polewards side of the tail. The structure of the footprints can give us insight about the moon-planet interaction and can be used as a diagnostic to infer characteristics of the moon, the magnetospheric magnetic field and density.

In this work, we showed that the position of the footprints can be used to deduce a density model along the magnetic field lines, giving insights about the temperature and Io torus density. The resulting values for peak density, ion temperature and torus scale height are in agreement with the ones given in the literature (e.g. Bagenal and Delamere (2011), Dougherty et al. (2017) and Phipps et al. (2020)).

Furthermore, the position of secondary spots in the Io footprint tail in the observations by Mura et al. (2018) can be explained by the reflection of Alfvén waves at the Alfvén phase velocity gradients at the torus boundary and Jupiter’s ionosphere. Even though not every feature in the tail can be directly connected to a specific reflection pattern, the separation distance of the tail spots of  $\delta \approx 350$  km is well in agreement with the findings of this study. Therefore, it is possible that the AASS is produced by multiple reflections of Alfvén waves, triggering wave particle interactions close to Jupiter’s ionosphere.

To investigate, which mechanisms could create the alternating structures in the Io footprint tail and break the symmetry between the equatorward and poleward side, we first conducted a purely alfvénic study using the equations given by Neubauer (1980) and Saur et al. (1998). In this study, we investigated the effects of non-linear reflections and the Hall effect on the Poynting flux, which was used as a Proxy for the morphology and position of the footprint emissions. It could be shown that strong density gradients, as they are present at the Jovian ionosphere, strongly deform the Alfvén wing and change the morphology and propagation of transmitted as well as reflected Alfvén wing similar to the results by Jacobsen et al. (2007). In the same study, the influence of the Hall conductance onto the shape of the Alfvén wing was analyzed. The Hall effect changes the fields inside the Alfvén wing significantly, breaking the symmetry that was present only considering Pedersen conductance. Combined with non-linear reflections this effect

showed a strong alteration of the Poynting flux morphology.

To confirm this hypothesis and to investigate further possibly symmetry breaking effects, simulations were conducted with the single fluid MHD code PLUTO. The aim of this study was not a detailed reproduction of all features of Io's footprint and associated tail features including the substructures reported in Moirano et al. (2021) or the bifurcations in Mura et al. (2018) or Szalay et al. (2018), but a basic investigation of the cause of the alternating structures, which are fixed in Io's rest frame. In a first step a reference simulation was set up. In this simulation no symmetry breaking mechanisms were included. The simulation was realized in a simplified geometry with a homogeneous background field. This allowed to examine the simulation results more easily and symmetry breaking effects can be separated from geometric effects. However, the simulation domain was set up to agree with actual Alfvén wave travel times and allow realistic reflection patterns. The reference simulation already showed a complex Poynting flux morphology near the Jovian ionosphere. In a next step, symmetry breaking mechanisms were added to the simulation. The results were compared to the reference simulation.

The first mechanism was the Hall effect. It could be shown that the Hall effect together with strong non-linear reflections at the Jovian ionosphere can create Alfvén bridges, that are used by the reflected Alfvén wing to cross the plane between equatorward and poleward part of the Io footprint tail. This can create alternating spots as seen in the AASS. Therefore, the Hall effect is a promising mechanism to produce the observed structures. If that is the case, we could expect similar however weaker asymmetries in the tail of Europa that is also expected to have a non-negligible Hall conductance.

As a second mechanism the travel time difference between Alfvén wave packages originating from the Jupiter facing side and those originating from the opposite side of Io was investigated. This was realized by implementing a density gradient along the Jupiter-Io axis in the simulation. The Poynting flux in the analysis plane showed only a slight deformation of the features near the main footprint. Down the tail however, the travel time difference of multiple reflections accumulate and the asymmetry increases. This alone can not explain the AASS, whose alternating character begins directly at the main emission. Yet, it could be shown that in the case of smaller Hall conductances relative to the Pedersen conductance, the travel time difference can enhance the asymmetry and can be a contributing factor to create the AASS. This effect was assumed to be minor in the case of the other Galilean moons.

As a third mechanism the asymmetry in Io's ionosphere was investigated. Until now, Io has been represented as a perfectly radially symmetric neutral gas cloud, resulting in a rotationally symmetric Pedersen and Hall conductance. However, Io's atmosphere and the resulting conductances are highly asymmetric with a minimum at the poles and a maximum at the sun facing side. The corresponding neutral gas cloud that satisfies the expected distribution of Hall and Pedersen conductances has been implemented. The simulation resulted in negligible differences to the reference simulation, only slightly shifting the Poynting flux respectively to the location of the maximum conductances. Therefore, we ruled out the asymmetries in the atmosphere as the reason for the AASS.

Therefore, we conclude that the Hall effect is the most promising candidate to produce the AASS. With further observations of the Io footprint at other orbital positions as well as the other Galilean moons, we could test this hypothesis. If we see similar, though weaker AASS in Europa's tail this would support the Hall effect as a primary reason behind the observed structures.

---

## Bibliography

---

- Acuna, M., Neubauer, F., Ness, N., 1981. Standing alfvén wave current system at io: Voyager 1 observations. *Journal of Geophysical Research: Space Physics* 86, 8513–8521.
- Bagenal, F., 1983. Alfvén wave propagation in the io plasma torus. *Journal of Geophysical Research: Space Physics* 88, 3013–3025.
- Bagenal, F., 1994. Empirical model of the io plasma torus: Voyager measurements. *Journal of Geophysical Research: Space Physics* 99, 11043–11062.
- Bagenal, F., Adriani, A., Allegrini, F., Bolton, S., Bonfond, B., Bunce, E., Connerney, J., Cowley, S., Ebert, R., Gladstone, G., et al., 2017. Magnetospheric science objectives of the juno mission. *Space Science Reviews* 213, 219–287.
- Bagenal, F., Delamere, P.A., 2011. Flow of mass and energy in the magnetospheres of jupiter and saturn. *Journal of Geophysical Research: Space Physics* 116.
- Bagenal, F., Dols, V., 2020. The space environment of io and europa. *Journal of Geophysical Research: Space Physics* 125, e2019JA027485.
- Bagenal, F., Sullivan, J.D., 1981. Direct plasma measurements in the io torus and inner magnetosphere of jupiter. *Journal of Geophysical Research: Space Physics* 86, 8447–8466.
- Baumjohann, W., Treumann, R.A., 2012. *Basic space plasma physics* (revised edition). World Scientific Publishing Company.
- Bhattacharyya, D., Clarke, J.T., Montgomery, J., Bonfond, B., Gérard, J.C., Grodent, D., 2018. Evidence for auroral emissions from callisto’s footprint in hst uv images. *Journal of Geophysical Research: Space Physics* 123, 364–373.
- Bigg, E., 1964. Influence of the satellite io on jupiter’s decametric emission. *Nature* 203, 1008–1010.

- Blöcker, A., Saur, J., Roth, L., 2016. Europa's plasma interaction with an inhomogeneous atmosphere: Development of alfvén winglets within the alfvén wings. *Journal of Geophysical Research: Space Physics* 121, 9794–9828.
- Blöcker, A., Saur, J., Roth, L., Strobel, D.F., 2018. Mhd modeling of the plasma interaction with io's asymmetric atmosphere. *Journal of Geophysical Research: Space Physics* 123, 9286–9311.
- Bolton, S.J., Bagenal, F., Blanc, M., Cassidy, T., Chané, E., Jackman, C., Jia, X., Kotova, A., Krupp, N., Milillo, A., et al., 2015. Jupiter's magnetosphere: plasma sources and transport. *Space Science Reviews* 192, 209–236.
- Bonfond, B., Grodent, D., Gérard, J.C., Radioti, A., Saur, J., Jacobsen, S., 2008. Uv io footprint leading spot: A key feature for understanding the uv io footprint multiplicity? *Geophysical Research Letters* 35.
- Bonfond, B., Saur, J., Grodent, D., Badman, S., Bisikalo, D., Shematovich, V., Gérard, J.C., Radioti, A., 2017. The tails of the satellite auroral footprints at jupiter. *Journal of Geophysical Research: Space Physics* 122, 7985–7996.
- Bridge, H., Belcher, J., Lazarus, A., Sullivan, J., McNutt, R., Bagenal, F., Scudder, J., Sittler, E., Siscoe, G., Vasyliunas, V., et al., 1979. Plasma observations near jupiter: Initial results from voyager 1. *Science* 204, 987–991.
- Broadfoot, A., Belton, M., Takacs, P., Sandel, B., Shemansky, D., Holberg, J., Ajello, J., Atreya, S., Donahue, T., Moos, H., et al., 1979. Extreme ultraviolet observations from voyager 1 encounter with jupiter. *Science* 204, 979–982.
- Brown, R.A., Chaffee Jr, F.H., 1974. High-resolution spectra of sodium emission from io. *The Astrophysical Journal* 187, L125.
- Burke, B.F., Franklin, K.L., 1955. Observations of a variable radio source associated with the planet jupiter. *Journal of Geophysical Research* 60, 213–217.
- Chané, E., Saur, J., Poedts, S., 2013. Modeling jupiter's magnetosphere: Influence of the internal sources. *Journal of Geophysical Research: Space Physics* 118, 2157–2172.
- Chapman, S., Bartels, J., 1940. *Geomagnetism, vol. ii: Analysis of the data, and physical theories.* Geomagnetism .
- Chen, F.F., et al., 1984. *Introduction to plasma physics and controlled fusion. volume 1.* Springer.
- Clarke, J., Ajello, J., Ballester, G., Ben Jaffel, L., Connerney, J., Gérard, J.C., Gladstone, G., Grodent, D., Pryor, W., Trauger, J., et al., 2002. Ultraviolet emissions from the magnetic footprints of io, ganymede and europa on jupiter. *Nature* 415, 997–1000.
- Clarke, J.T., Ballester, G.E., Trauger, J., Evans, R., Connerney, J.E., Stapelfeldt, K., Crisp, D., Feldman, P.D., Burrows, C.J., Casertano, S., et al., 1996. Far-ultraviolet imaging of jupiter's aurora and the io "footprint". *Science* 274, 404–409.

- Connerney, J., 1981. The magnetic field of jupiter: A generalized inverse approach. *Journal of Geophysical Research: Space Physics* 86, 7679–7693.
- Connerney, J., Baron, R., Satoh, T., Owen, T., 1993. Images of excited h3+ at the foot of the io flux tube in jupiter’s atmosphere. *Science* 262, 1035–1038.
- Connerney, J., Kotsiaros, S., Oliverson, R., Espley, J., Joergensen, J.L., Joergensen, P., Merayo, J.M., Herceg, M., Bloxham, J., Moore, K., et al., 2018. A new model of jupiter’s magnetic field from juno’s first nine orbits. *Geophysical Research Letters* 45, 2590–2596.
- Connerney, J., Satoh, T., 2000. The h3+ ion: A remote diagnostic of the jovian magnetosphere. *Philosophical Transactions of the Royal Society of London. Series A: Mathematical, Physical and Engineering Sciences* 358, 2471–2483.
- Connerney, J., Timmins, S., Herceg, M., Joergensen, J., 2020. A jovian magnetodisc model for the juno era. *Journal of Geophysical Research: Space Physics* 125, e2020JA028138.
- Connerney, J., Timmins, S., Oliverson, R., Espley, J., Joergensen, J., Kotsiaros, S., Joergensen, P., Merayo, J., Herceg, M., Bloxham, J., et al., 2021. A new model of jupiter’s magnetic field at the completion of juno’s prime mission. *Journal of Geophysical Research: Planets* , e2021JE007055.
- Connerney, J.E., Acuña, M.H., Ness, N.F., Satoh, T., 1998. New models of jupiter’s magnetic field constrained by the io flux tube footprint. *Journal of Geophysical Research: Space Physics* 103, 11929–11939.
- Crary, F., 1997. On the generation of an electron beam by io. *Journal of Geophysical Research: Space Physics* 102, 37–49.
- Damiano, P., Delamere, P., Stauffer, B., Ng, C.S., Johnson, J., 2019. Kinetic simulations of electron acceleration by dispersive scale alfvén waves in jupiter’s magnetosphere. *Geophysical Research Letters* 46, 3043–3051.
- Deift, P., Goertz, C., 1973. The propagation of alfvén waves along io’s flux tube. *Planetary and Space Science* 21, 1417–1429.
- Delamere, P., Bagenal, F., Steffl, A., 2005. Radial variations in the io plasma torus during the cassini era. *Journal of Geophysical Research: Space Physics* 110.
- Dougherty, L., Bodisch, K., Bagenal, F., 2017. Survey of voyager plasma science ions at jupiter: 2. heavy ions. *Journal of Geophysical Research: Space Physics* 122, 8257–8276.
- Drell, S., Foley, H., Ruderman, M., 1965. Drag and propulsion of large satellites in the ionosphere: An alfvén propulsion engine in space. *Journal of Geophysical Research* 70, 3131–3145.
- Falle, S., 2002. Rarefaction shocks, shock errors and low order of accuracy in zeus. *arXiv preprint astro-ph/0207419* .
- Feaga, L.M., McGrath, M., Feldman, P.D., 2009. Io’s dayside so2 atmosphere. *Icarus* 201, 570–584.

- Frank, L., Paterson, W., 2001. Survey of thermal ions in the io plasma torus with the galileo spacecraft. *Journal of Geophysical Research: Space Physics* 106, 6131–6149.
- Franklin, K.L., Burke, B.F., 1958. Radio observations of the planet jupiter. *Journal of Geophysical Research* 63, 807–824.
- Gérard, J.C., Saglam, A., Grodent, D., Clarke, J.T., 2006. Morphology of the ultraviolet io footprint emission and its control by io’s location. *Journal of Geophysical Research: Space Physics* 111.
- Goertz, C., 1980. Io’s interaction with the plasma torus. *Journal of Geophysical Research: Space Physics* 85, 2949–2956.
- Goldreich, P., Lynden-Bell, D., 1969. Io, a jovian unipolar inductor. *The Astrophysical Journal* 156, 59–78.
- Gurnett, D.A., Goertz, C., 1983. Ion cyclotron waves in the io plasma torus: Polarization reversal of whistler mode noise. *Geophysical research letters* 10, 587–590.
- Hess, S.L., Delamere, P., Dols, V., Bonfond, B., Swift, D., 2010. Power transmission and particle acceleration along the io flux tube. *Journal of Geophysical Research: Space Physics* 115.
- Hinton, P., Bagenal, F., Bonfond, B., 2019. Alfvén wave propagation in the io plasma torus. *Geophysical Research Letters* 46, 1242–1249.
- Jacobsen, S., Neubauer, F., Saur, J., Schilling, N., 2007. Io’s nonlinear mhd-wave field in the heterogeneous jovian magnetosphere. *Geophysical research letters* 34.
- Jacobsen, S., Saur, J., Neubauer, F., Bonfond, B., Gérard, J.C., Grodent, D., 2010. Location and spatial shape of electron beams in io’s wake. *Journal of Geophysical Research: Space Physics* 115.
- Kivelson, M.G., Bagenal, F., Kurth, W.S., Neubauer, F.M., Paranicas, C., Saur, J., 2004. Magnetospheric interactions with satellites. *Jupiter: The planet, satellites and magnetosphere* , 513–536.
- Kliore, A., Cain, D.L., Fjeldbo, G., Seidel, B.L., Rasool, S., 1974. Preliminary results on the atmospheres of io and jupiter from the pioneer 10 s-band occultation experiment. *Science* 183, 323–324.
- Kliore, A., Fjeldbo, G., Seidel, B., Sweetnam, D., Sesplaukis, T., Woiceshyn, P., Rasool, S., 1975. The atmosphere of io from pioneer 10 radio occultation measurements. *Icarus* 24, 407–410.
- Kupo, I., Mekler, Y., Mekler, Y., Eviatar, A., 1976. Detection of ionized sulfur in the jovian magnetosphere. *The Astrophysical Journal* 205, L51–L53.
- Lellouch, E., Ali-Dib, M., Jessup, K.L., Smette, A., Käufl, H.U., Marchis, F., 2015. Detection and characterization of io’s atmosphere from high-resolution 4- $\mu$ m spectroscopy. *Icarus* 253, 99–114.

- Lellouch, E., McGrath, M.A., Jessup, K.L., 2007. Io's atmosphere, in: *Io After Galileo*. Springer, pp. 231–264.
- Mendillo, M., Laurent, S., Wilson, J., Baumgardner, J., Konrad, J., Karl, W.C., 2007. The sources of sodium escaping from io revealed by spectral high definition imaging. *Nature* 448, 330–332.
- Mignone, A., Bodo, G., Massaglia, S., Matsakos, T., Tesileanu, O.e., Zanni, C., Ferrari, A., 2007. Pluto: a numerical code for computational astrophysics. *The Astrophysical Journal Supplement Series* 170, 228.
- Moirano, A., Mura, A., Adriani, A., Dols, V., Bonfond, B., Waite, J.H., Hue, V., Szalay, J.R., Sulaiman, A.H., Dinelli, B.M., et al., 2021. Morphology of the auroral tail of io, europa, and ganymede from jiram l-band imager. *Journal of Geophysical Research: Space Physics* 126, e2021JA029450.
- Morris, D., Berge, G., 1962. Measurements of the polarization and angular extent of the decimetric radiation of jupiter. *The Astrophysical Journal* 136, 276–282.
- Moses, J.I., Zolotov, M.Y., Fegley Jr, B., 2002. Photochemistry of a volcanically driven atmosphere on io: Sulfur and oxygen species from a pele-type eruption. *Icarus* 156, 76–106.
- Mura, A., Adriani, A., Connerney, J., Bolton, S., Altieri, F., Bagenal, F., Bonfond, B., Dinelli, B., Gérard, J.C., Greathouse, T., et al., 2018. Juno observations of spot structures and a split tail in io-induced aurorae on jupiter. *Science* 361, 774–777.
- Neubauer, F., 1980. Nonlinear standing alfvén wave current system at io: Theory. *Journal of Geophysical Research: Space Physics* 85, 1171–1178.
- Neubauer, F.M., 1998. The sub-alfvénic interaction of the galilean satellites with the jovian magnetosphere. *Journal of Geophysical Research: Planets* 103, 19843–19866.
- Neubauer, F.M., 1999. Alfvén wings and electromagnetic induction in the interiors: Europa and callisto. *Journal of Geophysical Research: Space Physics* 104, 28671–28684.
- Paranicas, C., Cheng, A., Williams, D., 1998. Inference of europa's conductance from the galileo energetic particles detector. *Journal of Geophysical Research: Space Physics* 103, 15001–15007.
- Peale, S.J., Cassen, P., Reynolds, R.T., 1979. Melting of io by tidal dissipation. *Science* 203, 892–894.
- Phipps, P.H., Withers, P., 2017. Radio occultations of the io plasma torus by juno are feasible. *Journal of Geophysical Research: Space Physics* 122, 1731–1750.
- Phipps, P.H., Withers, P., Buccino, D.R., Yang, Y.M., 2018. Distribution of plasma in the io plasma torus as seen by radio occultation during juno perijove 1. *Journal of Geophysical Research: Space Physics* 123, 6207–6222.

- Phipps, P.H., Withers, P., Buccino, D.R., Yang, Y.M., Parisi, M., 2019. Variations in the density distribution of the io plasma torus as seen by radio occultations on juno perijoves 3, 6, and 8. *Journal of Geophysical Research: Space Physics* 124, 5200–5221.
- Phipps, P.H., Withers, P., Buccino, D.R., Yang, Y.M., Parisi, M., 2021. Two years of observations of the io plasma torus by juno radio occultations: Results from perijoves 1 to 15. *Journal of Geophysical Research: Space Physics* 126, e2020JA028710.
- Phipps, P.H., Withers, P., Vogt, M.F., Buccino, D.R., Yang, Y.M., Parisi, M., Ranquist, D., Kollmann, P., Bolton, S., 2020. Where is the io plasma torus? a comparison of observations by juno radio occultations to predictions from jovian magnetic field models. *Journal of Geophysical Research: Space Physics* 125, e2019JA027633.
- Richardson, J.D., Siscoe, G.L., Bagenal, F., Sullivan, J.D., 1980. Time dependent plasma injection by io. *Geophysical Research Letters* 7, 37–40.
- Saur, J., Grambusch, T., Duling, S., Neubauer, F., Simon, S., 2013. Magnetic energy fluxes in sub-alfvénic planet star and moon planet interactions. *Astronomy & Astrophysics* 552, A119.
- Saur, J., Janser, S., Schreiner, A., Clark, G., Mauk, B.H., Kollmann, P., Ebert, R.W., Allegrini, F., Szalay, J.R., Kotsiaros, S., 2018. Wave-particle interaction of alfvén waves in jupiter’s magnetosphere: Auroral and magnetospheric particle acceleration. *Journal of Geophysical Research: Space Physics* 123, 9560–9573.
- Saur, J., Neubauer, F.M., Strobel, D.F., Summers, M.E., 1999. Three-dimensional plasma simulation of io’s interaction with the io plasma torus: Asymmetric plasma flow. *Journal of Geophysical Research: Space Physics* 104, 25105–25126.
- Saur, J., Strobel, D., Neubauer, F., 1998. Interaction of the jovian magnetosphere with europa: Constraints on the neutral atmosphere. *Journal of Geophysical Research: Planets* 103, 19947–19962.
- Schlegel, S., Saur, J., 2022. Alternating emission features in io’s footprint tail: Magneto-hydrodynamical simulations of possible causes. *Journal of Geophysical Research: Space Physics* 127, e2021JA030243.
- Schunk, R., 1975. Transport equations for aeronomy. *Planetary and Space Science* 23, 437–485.
- Simon, S., Liuzzo, L., Addison, P., 2021. Role of the ionospheric conductance profile in sub-alfvénic moon-magnetosphere interactions: An analytical model. *Journal of Geophysical Research: Space Physics* 126, e2021JA029191.
- Southwood, D.J., Kivelson, M.G., Walker, R.J., Slavin, J.A., 1980. Io and its plasma environment. *Journal of Geophysical Research: Space Physics* 85, 5959–5968.
- Spencer, J.R., Jessup, K.L., McGrath, M.A., Ballester, G.E., Yelle, R., 2000. Discovery of gaseous s<sub>2</sub> in io’s pele plume. *Science* 288, 1208–1210.

- Strobel, D.F., Wolven, B.C., 2001. The atmosphere of io: Abundances and sources of sulfur dioxide and atomic hydrogen, in: *Physics of Space: Growth Points and Problems*. Springer, pp. 271–287.
- Szalay, J., Allegrini, F., Bagenal, F., Bolton, S., Bonfond, B., Clark, G., Connerney, J., Ebert, R., Hue, V., McComas, D., et al., 2020. A new framework to explain changes in io's footprint tail electron fluxes. *Geophysical Research Letters* 47, e2020GL089267.
- Szalay, J., Bonfond, B., Allegrini, F., Bagenal, F., Bolton, S., Clark, G., Connerney, J., Ebert, R., Ergun, R., Gladstone, G., et al., 2018. In situ observations connected to the io footprint tail aurora. *Journal of Geophysical Research: Planets* 123, 3061–3077.
- Thomas, N., Bagenal, F., Hill, T., Wilson, J., 2004. The io neutral clouds and plasma torus. *Jupiter. The planet, satellites and magnetosphere* 1, 561–591.
- Trauger, J.T., 1984. The jovian nebula: A post-voyager perspective. *Science* 226, 337–341.
- Tsang, C.C., Spencer, J.R., Jessup, K.L., 2013. Synergistic observations of io's atmosphere in 2010 from hst-cos in the mid-ultraviolet and irtf-texes in the mid-infrared. *Icarus* 226, 604–616.
- Tsang, C.C., Spencer, J.R., Lellouch, E., Lopez-Valverde, M.A., Richter, M.J., 2016. The collapse of io's primary atmosphere in jupiter eclipse. *Journal of Geophysical Research: Planets* 121, 1400–1410.
- Vasavada, A.R., Bouchez, A.H., Ingersoll, A.P., Little, B., Anger, C.D., 1999. Jupiter's visible aurora and io footprint. *Journal of Geophysical Research: Planets* 104, 27133–27142.
- Vasyliūnas, V.M., 2016. Physical origin of pickup currents, in: *Annales Geophysicae, Copernicus GmbH*. pp. 153–156.
- Warwick, J.W., 1963. The position and sign of jupiter's magnetic moment. *The Astrophysical Journal* 137, 1317.
- Williams, D., Mauk, B., McEntire, R., Roelof, E., Armstrong, T., Wilken, B., Roederer, J., Krimigis, S., Fritz, T., Lanzerotti, L., 1996. Electron beams and ion composition measured at io and in its torus. *Science* 274, 401–403.
- Williams, D., Thorne, R., Mauk, B., 1999. Energetic electron beams and trapped electrons at io. *Journal of Geophysical Research: Space Physics* 104, 14739–14753.
- Wright, A.N., 1987. The interaction of io's alfvén waves with the jovian magnetosphere. *Journal of Geophysical Research: Space Physics* 92, 9963–9970.



## A. Vlasov Equation

### A.1. Collision Term

As discussed in chapter 3.4, the Boltzmann collision can be approximated by

$$\left(\frac{\partial f}{\partial t}\right)_{col} = \frac{\nu}{n_n}(nf_n - n_n f) = \nu \left(\frac{n}{n_n}f_n - f\right) \quad (\text{A.1})$$

Here,  $n_n$  is the density of collision partner and therefore the zero-th velocity moment of the neutral particle distribution function  $f_n$ , while  $n$  is the zero-th velocity moment of the plasma phase space distribution function  $f$ . The prefactor  $\nu/n_n$  is the collision frequency  $\nu$  normalized to the density of the collision partner. From this we can calculate the velocity moments of the collision term:

$$\left(\frac{\partial \rho}{\partial t}\right)_{col} = \int \left(\frac{\partial f}{\partial t}\right)_{col} d^3\mathbf{v} = \nu \left(\frac{n}{n_n}n_n - n\right) = 0 \quad (\text{A.2})$$

For the momentum equation, the source term does not vanish:

$$\begin{aligned} \left(\frac{\partial \rho \mathbf{v}}{\partial t}\right)_{col} &= m \int \mathbf{v} \left(\frac{\partial f}{\partial t}\right)_{col} d^3\mathbf{v} = \nu m \left(\frac{n}{n_n}n_n \langle \mathbf{v}_n \rangle - n \langle \mathbf{v} \rangle\right) \\ &= \nu \rho (\mathbf{v}_n - \mathbf{v}) \end{aligned} \quad (\text{A.3})$$

Now, for the Energy equation, we get the following:

$$\begin{aligned} \left(\frac{\partial W}{\partial t}\right)_{col} &= \frac{m}{2} \int v^2 \left(\frac{\partial f}{\partial t}\right)_{col} d^3\mathbf{v} = \frac{\nu m}{2} \left(\frac{n}{n_n}n_n \langle v_n^2 \rangle - n \langle v^2 \rangle\right) \\ &= \frac{\nu \rho}{2} [(v_n^2 + 2e_n) - (v^2 + 2e)] \\ &= \frac{\nu \rho}{2} [(v_n^2 - v^2) + 2(e_n - e)] \\ &= \frac{\nu \rho}{2} [(\mathbf{v}_n - \mathbf{v})^2 - 2v^2 + 2\mathbf{v}_n \cdot \mathbf{v}] + \nu \rho (e_n - e) \\ &= \frac{\nu \rho}{2} [(\mathbf{v}_n - \mathbf{v})^2 + 2(\mathbf{v}_n - \mathbf{v}) \cdot \mathbf{v}] + \nu \rho (e_n - e) \end{aligned} \quad (\text{A.4})$$

For the evolution equation of the pressure this leads to :

$$\begin{aligned}
\left(\frac{\partial p}{\partial t}\right)_{col} &= \left(\frac{\partial W}{\partial t}\right)_{col} - \mathbf{v} \cdot \left(\frac{\partial \rho \mathbf{v}}{\partial t}\right)_{col} \\
&= \frac{\nu \rho}{2} [(\mathbf{v}_n - \mathbf{v})^2 + \cancel{2(\mathbf{v}_n - \mathbf{v}) \cdot \mathbf{v}}] + \nu \rho (e_n - e) - \cancel{\nu \rho \mathbf{v} \cdot (\mathbf{v}_n - \mathbf{v})} \\
&= \frac{\nu \rho}{2} (\mathbf{v}_n - \mathbf{v})^2 + \nu \rho (\epsilon_n - \epsilon)
\end{aligned} \tag{A.5}$$

## A.2. Production and Loss Term

The production and loss terms in the MHD equations, in particular in the continuity, momentum (velocity) and energy (pressure) equations should actually be calculated as velocity moments from a phase space density production and loss term  $f_{P,L} = f_P + f_L$ . This term consists of a production part

$$\frac{\partial f_P}{\partial t} = P(\mathbf{r}) \delta(\mathbf{v} - \mathbf{v}_0) \tag{A.6}$$

and a loss part

$$\frac{\partial f_L}{\partial t} = -L f(\mathbf{r}, \mathbf{v}). \tag{A.7}$$

Here,  $P(\mathbf{r})$  is a production rate, that is inhomogeneous in space (e.g. dependent on neutral gas density) and has the unit  $[P] = \text{m}^{-3} \text{s}^{-1}$ . The  $\delta(\mathbf{v} - \mathbf{v}_0)$  is the dirac delta distribution which ensures that only particles with velocity  $\mathbf{v}_0$  are produced. Furthermore, the loss term is proportional to the phase space density  $f$  since there is no preferred particle velocity for the loss term and it is also proportional to the density  $n(\mathbf{r}) = \int f d^3 \mathbf{v}$ . The loss rate  $L$  is constant and has the unit  $[L] = \text{s}^{-1}$ .

## Production and Loss in the Continuity Equation

For the continuity equation, we integrate the Vlasov equation over the velocity space. The left hand side of Equation (3.1) is the known continuity equation divided by the particle mass

$$\frac{\partial n}{\partial t} + \nabla \cdot (n \mathbf{v}) = \int \frac{\partial f_{P,L}}{\partial t} d^3 \mathbf{v} \tag{A.8}$$

For the integration of the production and loss term on the right hand side, we look at both terms separately:

$$\begin{aligned}
\int \frac{\partial f_P}{\partial t} d^3 \mathbf{v} &= P \int \delta(\mathbf{v} - \mathbf{v}_0) d^3 \mathbf{v} \\
&= P
\end{aligned} \tag{A.9}$$

and

$$\begin{aligned}
\int \frac{\partial f_L}{\partial t} d^3 \mathbf{v} &= -L \int f d^3 \mathbf{v} \\
&= -L n
\end{aligned} \tag{A.10}$$

It follows that the continuity equation for mass density, i.e.  $\rho = mn$  with production and loss term is

$$\frac{\partial \rho}{\partial t} + \nabla \cdot (\rho \mathbf{v}_b) = m(P - Ln) \tag{A.11}$$

Here,  $\mathbf{v}_b$  represents the mean velocity of the phase space distribution function at a certain location and is also called the bulk velocity of the plasma.

### Production and Loss in the Momentum Equation

The momentum equation is the first velocity moment and therefore is received when the Vlasov equation is multiplied by the velocity  $\mathbf{v}$  and integrated over the velocity space. The right hand side for the production and loss terms are

$$\begin{aligned} \int \mathbf{v} \frac{\partial f_P}{\partial t} d^3\mathbf{v} &= P \int \mathbf{v} \delta(\mathbf{v} - \mathbf{v}_0) d^3\mathbf{v} \\ &= P\mathbf{v}_0 \end{aligned} \quad (\text{A.12})$$

and

$$\begin{aligned} \int \mathbf{v} \frac{\partial f_L}{\partial t} d^3\mathbf{v} &= -L \int \mathbf{v} f d^3\mathbf{v} \\ &= -L n \mathbf{v}_b, \end{aligned} \quad (\text{A.13})$$

respectively. Therefore, the **momentum equation** has the extra source (and sink) term

$$Pm\mathbf{v}_0 - L\rho\mathbf{v}_b \quad (\text{A.14})$$

with  $\mathbf{v}$  here representing the bulk velocity of the plasma. However, the **velocity equation** has a different term for the production and loss rate:

$$\begin{aligned} \left( \rho \frac{\partial(\mathbf{v}_b)}{\partial t} + \rho \mathbf{v}_b \cdot \nabla \mathbf{v} \right)_{P,L} &= \left( \frac{\partial(\rho \mathbf{v}_b)}{\partial t} + \nabla \cdot (\rho \mathbf{v}_b \mathbf{v}_b) \right)_{P,L} - \mathbf{v}_b \left( \frac{\partial \rho}{\partial t} + \nabla \cdot (\rho \mathbf{v}_b) \right) \\ &= Pm\mathbf{v}_0 - L\rho\mathbf{v}_b - \mathbf{v}_b(Pm - L\rho) \\ &= Pm(\mathbf{v}_0 - \mathbf{v}_b) \end{aligned} \quad (\text{A.15})$$

As it can be seen, the velocity changes due to the difference in velocity between the new produced particles and the current bulk velocity  $\mathbf{v}$ , while the loss term does not change the velocity, but only the momentum. This is can be understood as follows. New particles, produced by the production term with velocity  $\mathbf{v}_0$  carry momentum in the form of  $m\mathbf{v}_0$ , therefore changing the overall momentum, except for the special case where  $\mathbf{v}_0 = \mathbf{0}$ , where no momentum is generated. The mean velocity is changed relative to current bulk velocity, so the bulk velocity can be slowed down even though maybe momentum is generated. If particles are lost, generally momentum is lost, since each particles carries momentum of  $m\mathbf{v}$ . However, since each particle, on average, has the bulk velocity, the overall velocity of the plasma is not changed, no matter how many particles are lost due to the loss term.

### Production and Loss in the Energy Equation

For the energy equation we use the second velocity moment multiplying equation (3.1) with  $v^2$ . This leads for the right hand side to

$$\begin{aligned} \int v^2 \frac{\partial f_P}{\partial t} d^3\mathbf{v} &= P \int v^2 \delta(\mathbf{v} - \mathbf{v}_0) d^3\mathbf{v} \\ &= P v_0^2 \end{aligned} \quad (\text{A.16})$$

and

$$\begin{aligned}
\int v^2 \frac{\partial f_L}{\partial t} d^3 \mathbf{v} &= -L \int v^2 f d^3 \mathbf{v} \\
&= -L \int (\mathbf{v}_b + \mathbf{v}^*)^2 f d^3 \mathbf{v} \\
&= -L \left( \int v_b^2 f d^3 \mathbf{v} + \int v^{*2} f d^3 \mathbf{v} \right) \\
&= -L \left( n v_b^2 + \frac{3p}{m} \right)
\end{aligned} \tag{A.17}$$

for the production and loss respectively. Here  $p = m/3 \int v^{*2} d^3 \mathbf{v}$  is the pressure, which is calculated by the variance in velocity, i.e. mean of squared velocity perturbation  $\mathbf{v}^*$ . The energy equation can have different forms, but it is sometimes defined as

$$\frac{\partial \epsilon}{\partial t} + \nabla \cdot (\mathbf{v}_b \epsilon) + p \nabla \cdot \mathbf{v}_b = \frac{m}{2} \left( \int v^2 \frac{Df}{Dt} d^3 \mathbf{v} - \mathbf{v}_b \cdot \left( 2 \int \mathbf{v} \frac{Df}{Dt} d^3 \mathbf{v} - \mathbf{v}_b \cdot \int \frac{Df}{Dt} d^3 \mathbf{v} \right) \right) = 0 \tag{A.18}$$

without any production terms. Here, we use the internal energy  $\epsilon = 3/2p$ . To see, how this equation changes with production and loss, we need to insert terms calculated for the first and second velocity moment of the right hand side.

$$\begin{aligned}
\left( \frac{\partial \epsilon}{\partial t} \right)_{P,L} &= \frac{m}{2} \left( \int v^2 \frac{\partial f_P}{\partial t} d^3 \mathbf{v} + \int v^2 \frac{\partial f_L}{\partial t} d^3 \mathbf{v} - 2 \mathbf{v}_b \cdot \int \mathbf{v} \frac{\partial f_P}{\partial t} d^3 \mathbf{v} - 2 \mathbf{v}_b \cdot \int \mathbf{v} \frac{\partial f_L}{\partial t} d^3 \mathbf{v} \right. \\
&\quad \left. + v_b^2 \int \frac{\partial f_P}{\partial t} d^3 \mathbf{v} + v_b^2 \int \frac{\partial f_L}{\partial t} d^3 \mathbf{v} \right) \\
&= \frac{m}{2} \left( P v_0^2 - L \left( n v_b^2 + \frac{3p}{m} \right) - P \mathbf{v}_b \cdot (2 \mathbf{v}_0 - \mathbf{v}_b) + 2 L n v_b^2 - L n v_b^2 \right) \\
&= \frac{m}{2} P (v_0^2 - 2 \mathbf{v}_b \cdot \mathbf{v}_0 + v_b^2) - L \epsilon \\
&= \frac{m}{2} P (\mathbf{v}_b - \mathbf{v}_0)^2 - L \epsilon
\end{aligned} \tag{A.19}$$

We look at the physical meaning of this result for the loss term and production term separately. The loss term is proportional to the internal energy just multiplied with the loss constant  $L$ . This comes from the fact that on average each particle contributes the same amount of internal energy to the overall budget, which results in the internal energy to be proportional to the number of particles. Removing random particles from the plasma leads to a reduction of internal energy proportional to the product of particles removed  $L$  and internal energy  $\epsilon$ . The production of particles with velocity  $\mathbf{v}_0$  results in an increase in pressure proportional to the kinetic energy density in the reference frame of the moving plasma. This is due to an increase in variance in velocity, when the newly created particles are moving relative to the bulk velocity.

Sometimes the energy equation is given in terms of internal energy per particle. This would result in the left hand side being

$$\begin{aligned}
\frac{\partial}{\partial t} \left( \frac{\epsilon}{n} \right) + (\mathbf{v}_b \cdot \nabla) \left( \frac{\epsilon}{n} \right) &= \left( \frac{1}{n} \frac{\partial \epsilon}{\partial t} - \frac{\epsilon}{n^2} \frac{\partial n}{\partial t} \right) + \mathbf{v}_b \cdot \left( \frac{1}{n} \nabla \epsilon - \frac{\epsilon}{n^2} \nabla n \right) \\
&= \frac{1}{n} \left( \frac{\partial \epsilon}{\partial t} + \nabla \cdot (\mathbf{v}_b \epsilon) \right) - \frac{\epsilon}{n} \nabla \cdot \mathbf{v}_b - \frac{\epsilon}{n^2} \left( \frac{\partial n}{\partial t} + \mathbf{v}_b \cdot \nabla n \right) \quad (\text{A.20}) \\
&= \frac{1}{n} \left( \frac{\partial \epsilon}{\partial t} + \nabla \cdot (\mathbf{v}_b \epsilon) \right) - \frac{\epsilon}{n^2} \left( \frac{\partial n}{\partial t} + \mathbf{v}_b \cdot \nabla n + n \nabla \cdot \mathbf{v}_b \right)
\end{aligned}$$

The first term is just the left hand side for the evolution equation of the internal energy divided by the number density  $n$ . The second term is the left hand side of the continuity equation multiplied by  $\epsilon/n^2$ . If we combine them, divide it by the mass  $m$  and use the calculated values for the production and loss terms in the evolution equation of internal energy and continuity equation we get

$$\begin{aligned}
\frac{\partial}{\partial t} \left( \frac{\epsilon}{\rho} \right) + (\mathbf{v}_b \cdot \nabla) \left( \frac{\epsilon}{\rho} \right) &= -\frac{1}{\rho} p \nabla \cdot \mathbf{v}_b + \frac{1}{\rho} \left( \frac{m}{2} P (\mathbf{v}_b - \mathbf{v}_0)^2 - L \epsilon \right) - \frac{\epsilon}{\rho^2} (P m - L \rho) \\
&= -\frac{1}{\rho} p \nabla \cdot \mathbf{v}_b + \frac{P m}{\rho^2} \left( \frac{1}{2} \rho (\mathbf{v}_b - \mathbf{v}_0)^2 - \epsilon \right) \quad (\text{A.21})
\end{aligned}$$

The absent of the Loss term in this equation can be understood as the internal energy per particle does not change if we remove a random particle. However, adding particles with a certain speed can add to the mean energy per particle if the variance per particle is increasing, meaning if

$$n(\mathbf{v}_b - \mathbf{v}_0)^2 > \int v^2 f d^3 \mathbf{v} \quad (\text{A.22})$$

## B. Analytical Derivations in the Alfvén Wing

### B.1. Perpendicular Magnetic Field

The magnetic field perpendicular to the Alfvén characteristic can be calculated using the definition of the characteristic  $\mathbf{z}^+ = \mathbf{v} + \mathbf{B}/\sqrt{\mu_0 \rho}$ .

$$\begin{aligned}
\mathbf{z}^+ \times \mathbf{B}_\perp &= \mathbf{z}^+ \times \mathbf{B} \\
&= \left( \mathbf{v} \pm \frac{\mathbf{B}}{\sqrt{\mu_0 \rho}} \right) \times \mathbf{B} \quad (\text{B.1}) \\
&= \mathbf{v} \times \mathbf{B} \\
&= -\mathbf{E}
\end{aligned}$$

$$\begin{aligned}
\mathbf{e}_\parallel \times \mathbf{E} &= -\frac{\mathbf{z}^+}{|\mathbf{z}^+|} \times (\mathbf{z}^+ \times \mathbf{B}_\perp) \\
&= \frac{-\cancel{(\mathbf{z}^+ \cdot \mathbf{B}_\perp)} \mathbf{z}^+ + |\mathbf{z}^+|^2 \mathbf{B}_\perp}{|\mathbf{z}^+|} \quad (\text{B.2}) \\
&= |\mathbf{z}^+| \mathbf{B}_\perp
\end{aligned}$$

Here perpendicular ( $\perp$ ) and parallel ( $\parallel$ ) are meant with respect to the Alfvén characteristic, which is tilted against the background magnetic field. Together with the definition of the Alfvén conductance in Equation (4.4), this concludes to

$$\mathbf{B}_\perp = \mu_0 \Sigma_A \mathbf{e}_\parallel \times \mathbf{E} \quad (\text{B.3})$$

## B.2. Numerical Alfvén Wing Model

Saur et al. (1999) have shown, that the Potential  $\Phi$  of the electric field  $\mathbf{E}$  can be calculated under the assumption that the obstacle in the plasma flow can be characterized with the Pedersen conductance  $\Sigma_P$ , the Hall conductance  $\Sigma_H$  and the Alfvén conductance  $\Sigma_A$ . In this case we want to assume that  $\Sigma_A$  is constant in the complete domain and  $\Sigma_H$  and  $\Sigma_P$  only depend on the radial distance  $r$ . The partial differential equation to be solved is

$$\frac{\Sigma_A + \Sigma_P}{r} \frac{\partial^2 \Phi}{\partial \varphi^2} + \frac{\partial}{\partial r} \left[ r(\Sigma_A + \Sigma_P) \frac{\partial \Phi}{\partial r} \right] + \frac{\partial \Sigma_H}{\partial r} \frac{\partial \Phi}{\partial \varphi} = 0 \quad (\text{B.4})$$

### Fourier Transform

Since this differential equation is linear in  $\Phi$ , we use Fourier Transform in the  $\varphi$ -direction and write  $\Phi$  as

$$\Phi_k(r, \varphi) = \Omega_k(\varphi) \Gamma_k(r) \quad (\text{B.5})$$

and

$$\Phi = \sum_{k=0}^{\infty} \Phi_k \quad (\text{B.6})$$

with the wavenumber  $k$  in  $\varphi$  direction. Since  $\Phi_k$  (and therefore  $\Omega_k$ ) needs to be  $2\pi$  periodic,  $k$  is an integer and we can write

$$\Omega_k(\varphi) = e^{ik\varphi}. \quad (\text{B.7})$$

Here, the initial phase of the potential ( $\varphi_0$ ) is in the phase of the complex factor  $\Gamma_k$ . This leads to a set of new ordinary differential equations:

$$\frac{\partial}{\partial r} \left[ r(\Sigma_A + \Sigma_P) \frac{\partial \Gamma_k}{\partial r} \right] + \left[ ik \frac{\partial \Sigma_H}{\partial r} - k^2 \frac{\Sigma_A + \Sigma_P}{r} \right] \Gamma_k = 0 \quad (\text{B.8})$$

### Piecewise Constant Conductances

If we assume  $\Sigma_P$  and  $\Sigma_H$  to be constant on a circular disk  $R_i < r < R_j$ , we can solve the set of differential equations using

$$\frac{\partial \Sigma_P}{\partial r} = \frac{\partial \Sigma_H}{\partial r} = 0 \quad (\text{B.9})$$

which leads to the simple ODE

$$r^2 \Gamma_k'' + r \Gamma_k' - k^2 \Gamma_k = 0 \quad (\text{B.10})$$

and has the simple solution

$$\Gamma_k = A_k r^{-k} + B_k r^k \quad (\text{B.11})$$

$A_k$  and  $B_k$  being integration constants. It can be shown, that if the boundary condition  $\lim_{r \rightarrow \infty} \Phi$  only consists of certain wavenumbers  $k$ , only  $\Phi_k \neq 0$ . This will in detail be shown in Section B.2. As in this case, where the boundary condition  $\lim_{r \rightarrow \infty} E_y = E_0$  is

$$\lim_{r \rightarrow \infty} \Phi = -E_0 r \sin(\varphi) \quad (\text{B.12})$$

only  $k = 1$  has to be considered and therefore

$$\Phi = \left[ \frac{A}{r} + Br \right] e^{i\varphi} \quad (\text{B.13})$$

### Iterative Method

As long as  $\Sigma_P$  and  $\Sigma_H$  are piecewise constant along  $r$  and do not depend on  $\varphi$ , the differential equation can be solved iteratively. We denote  $\Sigma_{P,n}$  and  $\Sigma_{H,n}$  as the Conductances in the  $n$ -th shell with the outer radius of it being  $R_n$  ( $R_N = \infty$ ). Using the fact, that in each shell the solution of the differential equation can be written as

$$\Phi_n = \left[ \frac{A_n}{r} + B_n r \right] e^{i\varphi} \quad (\text{B.14})$$

we can use boundary conditions, jump conditions and continuity to solve differential equation. First we have the boundary condition:

$$\lim_{r \rightarrow \infty} \Phi = -E_0 r \sin(\varphi) \quad (\text{B.15})$$

which can be written as  $B_N = iE_0$ . Furthermore no singularities are allowed, which means, that  $A_1 = 0$ . Now at each shell boundary at  $R_n$  the continuity  $\Phi_n = \Phi_{n+1}$  has to be fulfilled, which can be written as

$$(A_n - A_{n+1}) + R_n^2 (B_n - B_{n+1}) = 0 \quad (\text{B.16})$$

and a jump condition (equation (A2) in Saur et al. 1999):

$$\alpha_n A_n + \beta_n B_n + \gamma_n A_{n+1} + \delta_n B_{n+1} = 0 \quad (\text{B.17})$$

with

$$\alpha_n = (\Sigma_{P,n} + \Sigma_A) - i\Sigma_{H,n} \quad (\text{B.18})$$

$$\beta_n = [-(\Sigma_{P,n} + \Sigma_A) - i\Sigma_{H,n}] R_n^2 \quad (\text{B.19})$$

$$\gamma_n = -(\Sigma_{P,n+1} + \Sigma_A) + i\Sigma_{H,n+1} \quad (\text{B.20})$$

$$\delta_n = [(\Sigma_{P,n+1} + \Sigma_A) + i\Sigma_{H,n+1}] R_n^2 \quad (\text{B.21})$$

This is now a linear system of  $2N - 2$  equations with  $2N - 2$  unknowns since  $A_1$  and  $B_N$  are already known. Written in Matrix form it is

$$\begin{pmatrix} \beta_1 & \gamma_1 & \delta_1 & 0 & 0 & \dots & 0 \\ R_1^2 & -1 & -R_1^2 & 0 & 0 & \dots & 0 \\ 0 & \alpha_2 & \beta_2 & \gamma_2 & \delta_2 & \dots & 0 \\ 0 & 1 & R_2^2 & -1 & -R_2^2 & \dots & 0 \\ \vdots & \ddots & \ddots & \ddots & \ddots & \ddots & \vdots \\ 0 & \dots & \alpha_{N-2} & \beta_{N-2} & \gamma_{N-2} & \delta_{N-2} & 0 \\ 0 & \dots & 1 & R_{N-2}^2 & -1 & -R_{N-2}^2 & 0 \\ 0 & \dots & 0 & 0 & \alpha_{N-1} & \beta_{N-1} & \gamma_{N-1} \\ 0 & \dots & 0 & 0 & 1 & R_{N-1}^2 & -1 \end{pmatrix} \begin{pmatrix} B_1 \\ A_2 \\ B_2 \\ A_3 \\ \vdots \\ B_{N-2} \\ A_{N-1} \\ B_{N-1} \\ A_N \end{pmatrix} = \begin{pmatrix} 0 \\ 0 \\ 0 \\ 0 \\ \vdots \\ 0 \\ 0 \\ -i\delta_{N-1}E_0 \\ iR_{N-1}^2E_0 \end{pmatrix} \quad (\text{B.22})$$

For stability reasons, it is suggested to use  $R_n^2 B_n$  as a variable. This leads to more similar values in the matrix for the calculation of the inverse.

### Special case Saur et al. 1999

The special case of Saur et al. (1999) assumed  $\Sigma_P$  and  $\Sigma_H$  to be constant inside the Alfvén wing  $r < R$  and 0 outside:

$$\Sigma_{P,1} = \Sigma_P \quad (\text{B.23})$$

$$\Sigma_{H,1} = \Sigma_H \quad (\text{B.24})$$

$$\Sigma_{P,2} = 0 \quad (\text{B.25})$$

$$\Sigma_{H,2} = 0 \quad (\text{B.26})$$

$$R_1 = R \quad (\text{B.27})$$

The linear equation system (B.22) is here

$$\begin{pmatrix} \beta & \gamma \\ R^2 & -1 \end{pmatrix} \begin{pmatrix} B_1 \\ A_2 \end{pmatrix} = \begin{pmatrix} i\delta E_0 \\ -iR^2 E_0 \end{pmatrix} \quad (\text{B.28})$$

or

$$\begin{pmatrix} B_1 \\ A_2 \end{pmatrix} = \frac{1}{\beta + \gamma R^2} \begin{pmatrix} 1 & \gamma \\ R^2 & -\beta \end{pmatrix} \begin{pmatrix} i\delta E_0 \\ -iR^2 E_0 \end{pmatrix} \quad (\text{B.29})$$

with

$$\beta = [-\Sigma_P - \Sigma_A - i\Sigma_H]R^2 \quad (\text{B.30})$$

$$\gamma = -\Sigma_A \quad (\text{B.31})$$

$$\delta = \Sigma_A R^2 \quad (\text{B.32})$$

which leads to

$$B_1 = E_0 \frac{-2\Sigma_A \Sigma_H - 2i\Sigma_A(\Sigma_P + 2\Sigma_A)}{(\Sigma_P + 2\Sigma_A)^2 + \Sigma_H^2} \quad (\text{B.33})$$

$$A_2 = E_0 R^2 \frac{2\Sigma_A \Sigma_H - i(\Sigma_P(\Sigma_P + 2\Sigma_A) + \Sigma_H^2)}{(\Sigma_P + 2\Sigma_A)^2 + \Sigma_H^2} \quad (\text{B.34})$$

This can also be written in terms of

$$E_p = \left| \frac{A_2}{R^2} \right| = \sqrt{\frac{\Sigma_P^2 + \Sigma_H^2}{(\Sigma_P + 2\Sigma_A)^2 + \Sigma_H^2}} \quad (\text{B.35})$$

$$\tan(\Theta_P) = \frac{\Im(A_2)}{\Re(A_2)} = -\frac{\Sigma_H^2 + \Sigma_P(\Sigma_P + 2\Sigma_A)}{2\Sigma_A\Sigma_H} \quad (\text{B.36})$$

as  $A_2 = R^2 E_p e^{i\Theta_P}$ , which is the exact solution from Saur et al. (1999).

### Electric Field

We have now the Potential  $\Phi(r, \varphi)$  as complex potential over the whole domain. At each disk  $R_{n-1} < r < R_n$  with  $R_0 = 0$  and  $R_N = \infty$ , the Potential is calculated according to equation (B.14). Since  $e^{i\varphi} = \cos(\varphi) + i\sin(\varphi)$  as well as  $x = r \cos(\varphi)$  and  $y = r \sin(\varphi)$ , we can write

$$\Re(\Phi_n) = \Re\left(\frac{A_n}{r^2} + B_n\right)x - \Im\left(\frac{A_n}{r^2} + B_n\right)y \quad (\text{B.37})$$

The electric field is the gradient of the potential  $\mathbf{E} = -\nabla\Phi$ . Taking the derivative with respect to  $x$  and  $y$ , we receive  $E_x$  and  $E_y$  respectively, giving us

$$E_x = -\frac{\Re(A_n)}{r^2} \left(1 - \frac{2x^2}{r^2}\right) - \Re(B_n) - \Im(A_n) \frac{2xy}{r^4} \quad (\text{B.38})$$

$$E_y = \Re(A_n) \frac{2xy}{r^4} + \Im(B_n) + \frac{\Im(A_n)}{r^2} \left(1 - \frac{2y^2}{r^2}\right) \quad (\text{B.39})$$

### Higher Orders in $k$

For higher orders of  $k$ , the iterative method can be used the same way since  $\Omega_i$  and  $\Omega_j$  are orthogonal for  $i \neq j$ . Therefore the differential equation (B.10) can be solved giving us the solution for the  $n$ -th disk.

$$\Phi_k = \left[ \frac{A_{k,n}}{r^k} + B_{k,n} r^k \right] e^{ik\varphi} \quad (\text{B.40})$$

The solution  $\Phi_k$  also may not have any singularities, therefore  $A_{k,1} = 0$ . The continuity equation can be written as

$$(A_{k,n} - A_{k,n+1}) + R_n^{2k}(B_{k,n} - B_{k,n+1}) = 0 \quad (\text{B.41})$$

and the jump condition is therefore

$$\alpha_{k,n} A_{k,n} + \beta_{k,n} B_{k,n} + \gamma_{k,n} A_{k,n+1} + \delta_{k,n} B_{k,n+1} = 0 \quad (\text{B.42})$$

with

$$\alpha_{k,n} = (\Sigma_{P,n} + \Sigma_A) - i\Sigma_{H,n} \quad (\text{B.43})$$

$$\beta_{k,n} = [-(\Sigma_{P,n} + \Sigma_A) - i\Sigma_{H,n}]R_n^{2k} \quad (\text{B.44})$$

$$\gamma_{k,n} = -(\Sigma_{P,n+1} + \Sigma_A) + i\Sigma_{H,n+1} \quad (\text{B.45})$$

$$\delta_{k,n} = [(\Sigma_{P,n+1} + \Sigma_A) + i\Sigma_{H,n+1}]R_n^{2k} \quad (\text{B.46})$$

Similar to the previous linear equation system (B.22), the right hand side is defined by the boundary condition for the E-Field with the corresponding wavenumber in  $\varphi$  direction. If  $\lim_{r \rightarrow \infty} \Phi_k = 0$ , the right hand side is zero. Therefore only the trivial solution  $A_{k,n} = B_{k,n} = 0$  for all  $n$  exists leading to  $\Phi_k = 0$ . It can be shown, that the determinant of the corresponding matrix in equation (B.22) is non-zero, thus no non-trivial solution exist in this case.

### Derivation of Jump Condition

To derive the jump condition (B.17) following Saur et al. (1999), we take equation (B.8) and integrate it along a small interval at a boundary  $[R - \varepsilon, R + \varepsilon]$  and

$$\lim_{\varepsilon \rightarrow 0} \int_{R_n - \varepsilon}^{R_n + \varepsilon} \frac{\partial}{\partial r} \left[ r(\Sigma_A + \Sigma_P) \frac{\partial \Gamma_k}{\partial r} \right] + \left[ ik \frac{\partial \Sigma_H}{\partial r} - k^2 \frac{\Sigma_A + \Sigma_P}{r} \right] \Gamma_k dr = 0 \quad (\text{B.47})$$

Now since the integrated interval tends to zero, all parts of the integral vanish where the integrated function is finite. Since  $\Gamma_k$  needs to be continuous  $\Gamma_k$  and  $\frac{\partial \Gamma_k}{\partial r}$  are finite. We can rearrange above function as

$$\lim_{\varepsilon \rightarrow 0} \left[ r(\Sigma_A + \Sigma_P) \frac{\partial \Gamma_k}{\partial r} \right]_{R_n - \varepsilon}^{R_n + \varepsilon} + ik \int_{R_n - \varepsilon}^{R_n + \varepsilon} \frac{\partial}{\partial r} (\Sigma_H \Gamma_k) dr - \int_{R_n - \varepsilon}^{R_n + \varepsilon} ik \frac{\partial \Gamma_k}{\partial r} \Sigma_H + k^2 \frac{\Sigma_A + \Sigma_P}{r} \Gamma_k dr = 0 \quad (\text{B.48})$$

As stated above, the last integral vanishes for  $\lim_{\varepsilon \rightarrow 0}$ , so the jump condition can be written as

$$\lim_{\varepsilon \rightarrow 0} \left[ r(\Sigma_A + \Sigma_P) \frac{\partial \Gamma_k}{\partial r} + ik \Sigma_H \Gamma_k \right]_{R_n - \varepsilon}^{R_n + \varepsilon} = 0. \quad (\text{B.49})$$

Using (B.11) and multiplying the equation by  $R_n^k$ , this can be rewritten as:

$$\begin{aligned} & [k(\Sigma_A + \Sigma_{P,n+1})(-A_{k,n+1} + B_{k,n+1}R_n^{2k}) + ik\Sigma_{H,n+1}(A_{k,n+1} + B_{k,n+1}R_n^{2k})] \\ & - [k(\Sigma_A + \Sigma_{P,n})(-A_{k,n} + B_{k,n}R_n^{2k}) + ik\Sigma_{H,n}(A_{k,n} + B_{k,n}R_n^{2k})] = 0 \end{aligned} \quad (\text{B.50})$$

which can be rewritten as equations (B.17) and (B.42).

### B.3. Validation of the Code in the Case of Constant Conductances

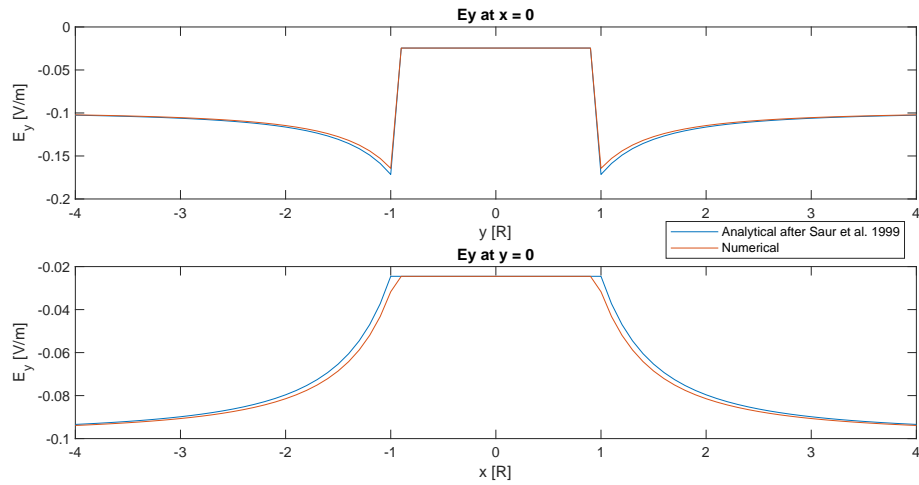


**Figure B.1.:** The electric field  $\mathbf{E}_y$  in y-direction along the y-axis (top) and x-axis (bottom) in the case of constant Pedersen conductance  $\Sigma_P$  inside a radius of  $r < 1$  and no conductance outside. The semi-analytical simulation results (red) are compared to the analytical solution by Saur et al. (1999) (blue).

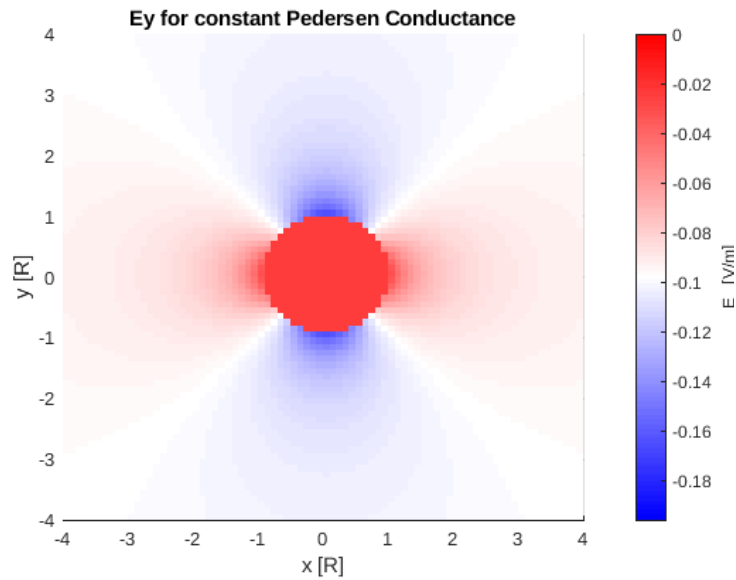


**Figure B.2.:** The electric field  $\mathbf{E}_y$  in y-direction as calculated by the semi-analytical simulation for a constant Pedersen conductance inside a radius of  $r < 1$  and no conductance outside. The resulting values and shape of the electric field are similar to the analytical results by Saur et al. (1999).

### B.4. Poynting Flux

The Poynting Flux  $\mathbf{S}$  is defined as

$$\mathbf{S} = \frac{\mathbf{E} \times \mathbf{B}}{\mu_0}. \quad (\text{B.51})$$

In cartesian coordinates the three components of the Poynting flux are

$$\mu_0 S_x = E_y B_z - E_z B_y \quad (\text{B.52a})$$

$$\mu_0 S_y = E_z B_x - E_x B_z \quad (\text{B.52b})$$

$$\mu_0 S_z = E_x B_y - E_y B_x \quad (\text{B.52c})$$

1. We first use the ideal MHD which uses

$$\mathbf{E} = -\mathbf{v} \times \mathbf{B} \quad (\text{B.53})$$

Therefore, we can write the components as:

$$\mu_0 S_x = (v_x B_z - v_z B_x) B_z - (v_y B_x - v_x B_y) B_y \quad (\text{B.54a})$$

$$\mu_0 S_y = (v_y B_x - v_x B_y) B_x - (v_z B_y - v_y B_z) B_z \quad (\text{B.54b})$$

$$\mu_0 S_z = (v_z B_y - v_y B_z) B_y - (v_x B_z - v_z B_x) B_x \quad (\text{B.54c})$$

or

$$\mu_0 S_x = v_x (B_z^2 + B_y^2) - B_x (v_z B_z + v_y B_y) \quad (\text{B.55a})$$

$$\mu_0 S_y = v_y (B_x^2 + B_z^2) - B_y (v_x B_x + v_z B_z) \quad (\text{B.55b})$$

$$\mu_0 S_z = v_z (B_x^2 + B_y^2) - B_z (v_y B_y + v_x B_x) \quad (\text{B.55c})$$

Now we assume that our background magnetic field only goes in  $z$ -direction ( $\mathbf{B}_0 = B_0 \mathbf{e}_z$ ). If we use the alfvénic correlation

$$\delta \mathbf{B}_\perp = \mp \delta \mathbf{v}_\perp \sqrt{\rho \mu_0} \quad (\text{B.56})$$

which is well fulfilled in the Alfvén wing, change to the rest frame of the plasma ( $\mathbf{v}_0 = \mathbf{0}$ ) and neglect the perturbations in  $z$ -direction, we can simplify the  $S_z$  equation to

$$\mu_0 S_z = \pm B_z \sqrt{\rho \mu_0} (\delta v_x^2 + \delta v_y^2) \quad (\text{B.57})$$

2. If we use equation (B.56) also for the first term in equation (B.55c) and exchange  $\delta B_\perp^2$  with  $\rho \mu_0 \delta v_\perp^2$  in equations (B.55c), this leads to

$$\mu_0 S_z = (v_z \rho \mu_0 \pm B_z \sqrt{\rho \mu_0}) \delta v_\perp^2 \quad (\text{B.58a})$$

$$= \rho \mu_0 z_z^\pm \delta v_\perp^2 \quad (\text{B.58b})$$

Since  $\mathbf{z}^\pm$  is constant and  $\sqrt{\rho\mu_0}z_z^\pm = B_{z,0}$ , we can also write

$$S_z = \pm B_{z,0} \sqrt{\frac{\rho}{\mu_0}} \delta v_\perp^2 = \pm v_A \frac{\delta B_\perp^2}{\mu_0} \quad (\text{B.59})$$

with  $v_A = \frac{|B|}{\sqrt{\mu_0\rho}}$ .

3. Now we look at what happens if we include the Hall effect of the form

$$\mathbf{E} = -\mathbf{v} \times \mathbf{B} + \frac{1}{ne} \mathbf{j} \times \mathbf{B}. \quad (\text{B.60})$$

However, we can rewrite this equation using

$$\mathbf{v}_H = \frac{\mathbf{j}}{ne} \quad (\text{B.61})$$

and we get

$$\mathbf{E} = -(\mathbf{v} - \mathbf{v}_H) \times \mathbf{B}. \quad (\text{B.62})$$

Equations (B.54) to (B.59) still apply if we exchange  $v_i$  with  $v_i - v_{H,i}$ .

4. Another thing we can look into are the values of  $\delta B_z$  and  $\delta v_z$ . For that we need the assumption  $|\mathbf{B}| = \text{const.}$  introduced for Alfvén wings by Neubauer (1980). With this assumption we have

$$B_z = \pm \sqrt{B_{z,0}^2 - B_\perp^2} \quad (\text{B.63a})$$

$$= \pm \sqrt{B_{z,0}^2 - \rho\mu_0\delta v_\perp^2} \quad (\text{B.63b})$$

or

$$\delta B_z = \pm \sqrt{B_{z,0}^2 - \rho\mu_0\delta v_\perp^2} \mp B_{z,0} \quad (\text{B.64})$$

However, with the assumption, that  $\delta\mathbf{z}^\pm = \mathbf{0}$ , it follows that

$$v_z = \delta v_z = \mp \frac{\sqrt{B_{z,0}^2 - \rho\mu_0\delta v_\perp^2} - B_{z,0}}{\sqrt{\rho\mu_0}} \quad (\text{B.65})$$

It is important to note, that in the equations for  $S_z$ , i.e. equations (B.54c), (B.55c) and (B.57) the value for  $B_z$  is the total field, not only the perturbation.

If we say, that the magnetic field perturbations are small against the background magnetic field, which is always true in case of  $M_A \cdot \alpha \ll 1$ , where  $M_A$  is the alfvénic Mach number and  $\alpha$  is the interaction strength, then we can perform a Taylor expansion of equation (B.65) and get

$$\delta v_z = \pm \frac{\sqrt{\rho\mu_0}\delta v_\perp^2}{2B_{z,0}} \quad (\text{B.66})$$



# Research Data Management

The data, Codes and scripts that were produced and written for this thesis are archived on the server `neptun@geo.uni-koeln.de` via the path `/raid0/archivierung/absolventen_archivierung/2022_PhD_SSchlegel_IoFootprint`. All data can be accessed via the Institute for Geophysics and Meteorology at the University of Cologne. Necessary information about the structure of the archive are summarised in a *README*. The overall structure consists of three folders. The folder `Codes_and_Scripts` archives the necessary codes and scripts that we used to simulate physical processes, analyse data and generate images. The folder `MHD_data` stores the results of the MHD simulations. The use of the data and codes underlies a license that is further specified in the file *LICENSE*.



# Erklärung zur Dissertation

Hiermit versichere ich an Eides statt, dass ich die vorliegende Dissertation selbstständig und ohne die Benutzung anderer als der angegebenen Hilfsmittel und Literatur angefertigt habe. Alle Stellen, die wörtlich oder sinngemäß aus veröffentlichten und nicht veröffentlichten Werken dem Wortlaut oder dem Sinn nach entnommen wurden, sind als solche kenntlich gemacht. Ich versichere an Eides statt, dass diese Dissertation noch keiner anderen Fakultät oder Universität zur Prüfung vorgelegen hat; dass sie - abgesehen von unten angegebenen Teilpublikationen und eingebundenen Artikeln und Manuskripten - noch nicht veröffentlicht worden ist sowie, dass ich eine Veröffentlichung der Dissertation vor Abschluss der Promotion nicht ohne Genehmigung des Promotionsausschusses vornehmen werde. Die Bestimmungen dieser Ordnung sind mir bekannt. Darüber hinaus erkläre ich hiermit, dass ich die Ordnung zur Sicherung guter wissenschaftlicher Praxis und zum Umgang mit wissenschaftlichem Fehlverhalten der Universität zu Köln gelesen und sie bei der Durchführung der Dissertation zugrundeliegenden Arbeiten und der schriftlich verfassten Dissertation beachtet habe und verpflichte mich hiermit, die dort genannten Vorgaben bei allen wissenschaftlichen Tätigkeiten zu beachten und umzusetzen. Ich versichere, dass die eingereichte elektronische Fassung der eingereichten Druckfassung vollständig entspricht.

Stephan Schlegel, Joachim Saur. Alternating emission features in Io's footprint tail: Magnetohydrodynamical simulations of possible causes. *Journal of Geophysical Research - Space Physics*.

Published: 15.3.2022

Köln, März 2022

---